NONDESTRUCTIVE ANALYSIS AND DEVELOPMENT

FINAL REPORT

Prepared for the
National Aeronautics and Space Administration
John F. Kennedy Space Center
Under Grant # NAG 10-0058

Principal Investigator
Dr. Faissal A. Moslehy, P.E.
Professor

Department of Mechanical and Aerospace Engineering
University of Central Florida
Orlando Florida, 32816

August 1993

NONDESTRUCTIVE ANALYSIS AND DEVELOPMENT

FINAL REPORT

August 1993

Principal Investigator
Dr. Faissal A. Moslehy, P.E.

Professor
Department of Mechanical and Aerospace Engineering
University of Central Florida
(407)823-5755

ABSTRACT

This final report summarizes the achievements of project #4 of the NASA/UCF Cooperative Agreement from January 1990 to December 1992. The objectives of this project are to review NASA's NDE program at Kennedy Space Center (KSC) and recommend means for enhancing the present testing capabilities through the use of improved or new technologies. During the period of the project, extensive development of a reliable nondestructive, non-contact vibration technique to determine and quantify the bond condition of the thermal protection system (TPS) tiles of the Space Shuttle Orbiter was undertaken.

Experimental modal analysis (EMA) is used as a non-destructive technique for the evaluation of Space Shuttle thermal protection system (TPS) tile bond integrity. Finite element (FE) models for tile systems were developed and were used to generate their vibration characteristics (i.e. natural frequencies and mode shapes). Various TPS tile assembly configurations as well as different bond conditions were analyzed. Results of finite element analyses demonstrated a drop in natural frequencies and a change in mode shapes which correlate with both size and location of disbond. Results of experimental testing of tile panels correlated with FE results and demonstrated the feasibility of EMA as a viable technique for tile bond verification. Finally, testing performed on the Space Shuttle Columbia using a laser doppler velocimeter demonstrated the application of EMA, when combined with FE modeling, as a non-contact, non-destructive bond evaluation technique.

NOMENCLATURE

In order to reference the finite element results contained within this report efficiently, the following nomenclature is adopted:

{Tile Assembly Label} {Tile Label} {Bond Condition Label} {Model Label}

. {Analysis Label} {File Type Label}

Tile Assembly Label:	ST = Single-Tile Assembly MT = 10-Tile Assembly
Tile Label:	3 = 2.4" Tile A = 191025-299 (OV-102)
Bond Condition Label:	00 = 100% Bond 80 = 80% Bond 60 = 60% Bond
Model Label:	N = Clamped Structure Without Filler Bar F = Clamped Structure With Filler Bar P = Extended Structure Panel With Filler Bar Q = Extended Structure Panel Without Filler Bar
Analysis Label:	EI = Eigenvalue Analysis FR = Frequency Response Analysis
Type Label: D = Output Data	I = Input

Examples:

STA80F.EID	Single-Tile Assembly, #191015-299, 80% Bond, With Filler Bar, Eigenvalue Output Data
MT300N.EID	10-Tile Assembly, 2" Tile, 100% Bond, Eigenvalue Output Data

TABLE OF CONTENTS

1 INTRODUCTION

A current need of the National Aeronautics & Space Administration (NASA) is the development of a non-destructive evaluation (NDE) technique to survey the bond condition of the thermal protection system (TPS) tiles on Orbital Vehicles (OV), or Space Shuttles. Each Orbital Vehicle possesses over 24,000 tiles, some of which may lose bond integrity during repeated flights. Thus, it is required to test many suspect tiles after each flight.

Currently, NASA performs this task via a pull test; a suction device is attached to the tile to be tested, and a test load is applied. If the tile withstands the prescribed load, the bond is deemed as nominal. If the tile is torn from the Space Shuttle skin, then, obviously, the bond is not nominal and the tile requires re-installation. Although this method may be simple, it is not efficient as it poses harm to the tile assembly itself. Application of the test load may disturb or damage the bond between the Space Shuttle and the tile. Therefore, this method may be regarded as a destructive method of evaluating bond integrity.

The non-destructive method NASA seeks will accomplish the task of bond integrity evaluation while posing no threat to bond integrity itself. As well, the sheer number of tiles to be tested demands that this method also be time efficient. The objective of this final report is to find and test a practical non-destructive, non-contact technique for the evaluation of Space Shuttle tile bond integrity.

An understanding of the complexity of the bonded tile assembly must first be reached. A Space Shuttle TPS tile assembly is comprised of several components of varying material and geometric properties, all of which must be known so that a feasible NDE technique can be decided upon.

When appraising the merit of a non-destructive evaluation technique, consideration must be given to the practicality of the method as applied to the problem as well as the accuracy of the method. That is, if a certain method is assured to produce 100% reliable results but requires the TPS tile to be submerged in water, it cannot be considered a practical solution to NASA's need. The most feasible NDE technique was decided upon by first considering the possibility of all methods, thus narrowing the field of techniques. Next, the practicality and theoretical promise were considered in order to arrive at a final choice. Eventual consideration has resulted in adopting a variation of the conventional experimental modal analysis (EMA) technique.

Justification of the modal analysis technique as a bond evaluation method is based on the fundamental theory of free vibration which states that the vibration characteristics (i.e. natural frequencies and mode shapes) of an object depend only on the mass and stiffness of the object. It is noted that the mass of a tile assembly with a nominal bond remains unchanged with a change in bond condition.
Conversely, the stiffness of a tile assembly will change with a change in bond condition. Thus, the modal characteristics of the tile assembly will change due to a loss of bond.

In order to verify the modal analysis method, various analytical models were analyzed using the finite element method. Different bond conditions were modeled, and the results were compared. Many other variables were also investigated to determine the most accurate analytical model.

Experimental testing of Space Shuttle Columbia tiles verified some finite element results. However, this testing served mostly to demonstrate the feasibility of experimental modal analysis as a non-destructive measurement tool for this problem.

2 TILE MATERIAL AND ASSEMBLY DESCRIPTION

Most of the surface of an Orbital Vehicle is covered with ceramic reusable surface insulation (RSI) to protect it from re-entry heat. The materials which comprise RSI are reinforced carbon/carbon (RCC), nylon felt (FRSI), and ceramic tile[1]. In areas of higher temperatures (between 1200 and 2300F), high temperature reusable surface insulation (HRSI) is used. HRSI consists of RSI coated with a black borosilicate, reaction-cured-glass coating[2].

There are three different ceramic RSI tiles, each having a different set of material properties. They are LI-900, LI-2200, and FRCI-12. FRCI-12 has a volumetric density of 12 pounds per cubic foot while LI-900 and LI-2200 have densities of 9 and 22 pounds per cubic foot, respectively[3,4,5]. Further material properties may be found in Table 1[6], however, it is important to note here that the material properties of these tiles are orthotropic (transversely isotropic in the X-Y plane). The designation of the tile axes as Roll and Cross-Roll given in Table 1 is established during the material manufacturing process of the strain isolation pad (see Tile-Structure Attachment Materials). In addition to the material properties, tile geometric properties vary as well. Therefore, it is possible for adjacent tiles to have dramatically different vibration characteristics.

2.1 Tile-Structure Attachment Materials

The RSI tiles are attached to the Orbital Vehicle via a strain isolation pad (SIP) and two layers of RTV glue as shown in Figure 1. RTV has an installed thickness of 0.01 inches. There are two different thicknesses of SIP used on the Orbital Vehicle, 0.09 and 0.16 inches, each having different material properties. Also, filler bar, which is made of material identical to that of the SIP, is placed below the gap of adjacent tiles. It is important to note that the filler bar is bonded only to the structure, not to the tile; the contact at this interface is caused only because the filler bar is in slight compression when installed. Material properties of the RTV and SIP are also given in Table 1.

Space Shuttle TPS tiles are installed in arrays or groups of tiles. Installation of a tile array begins with the RSI tiles. A layer of RTV is applied to the RSI tiles and SIP is affixed. Filler bar is affixed to the skin of the Orbital Vehicle using RTV. After both have cured, a layer of RTV is applied to the skin of the Orbital Vehicle, and the RSI/SIP array is affixed to the skin. The filler bar is thick enough to require constant pressure on the RSI/SIP array while the RTV cures. This produces a residual compressive load on the filler bar and a residual tensile load on the SIP and RTV after installation. This assures two significant results: (1) The filler bar will remain in contact with the tile under nominal conditions and (2) any disbond will result in the SIP rising off the structure, thus creating a void which can be detected by NDE techniques.

Table 1: TPS Materials Properties (Average Values)

Property		Tile (LI-900)	Tile (FRCI-12)	Tile (LI-2200)	SIP (0.16)	SIP (0.09)	RTV (560)
Young's Modulus (lb/in^2)	E_x	25,000	50,000	80,000	180	410	450
	E_y	25,000	50,000	80,000	600	600	450
	E_z	7,000	10,000	27,000	180	410	450
Poisson's Ratio	ν_{xy}	0.18	0.18	0.18	0.15*	0.34*	0.48
	ν_{xz}	0.16	0.16	0.16	0.4	0.4	0.48
	ν_{yz}	0.16	0.16	0.16	0.0	0.0	0.48
Shear Modulus (lb/in^2)	G_{xy}	10,500	13,500*	33,000	50	18	152
	G_{xz}	3,000	4,500	11,000	50	18	152
	G_{yz}	3,000	4,500	11,000	50	18	152
Mass Density ($lb*s^2/in^4$)	ρ	$13.5x10^{-6}$	$18.0x10^{-6}$	$33.0x10^{-6}$	$7.8x10^{-6}$	$11.1x10^{-6}$	$126x10^{-6}$

Legend

* Based on $\nu_{yx}=0.5^*$ Estimate; Actual Value Not Available

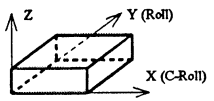

A loss of bond of the tile assembly can be caused by a variety of reasons. Deterioration of the RTV over time is one possible cause. Another is poor installation of the tile assembly, where possibly there is physical interference between the SIP and the filler bar (see Figure 2). Whatever the cause of disbond, NASA has found that the highest occurring and most likely location of disbond is along any of the edges of the SIP between the SIP and the Space Shuttle skin. Thus, for analyses in this report, disbond is assumed to occur at this location.

2.2 Orbital Vehicle Skin Structure

The skin structure of an Orbital Vehicle is made of aluminum and varies at different sections of the vehicle. For instance, at the mid-fuselage, an integrated skin-stringer structure is used, while in the aft-fuselage, a very dense machined grid structure is utilized. Obviously, the choice of structure is independent of the tiles, but rather is based upon loading conditions exerted on the Orbital Vehicle. Thus, the structure below a tile is different at different sections of the Orbital Vehicle. An illustration of the skin structure at the mid-fuselage is given in Figures 3 and 4.

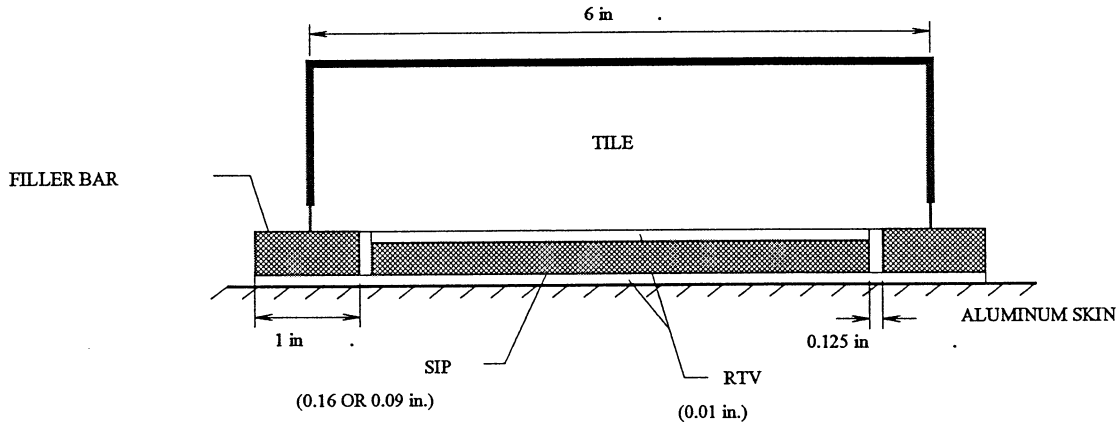

Figure 1: Single-Tile Assembly

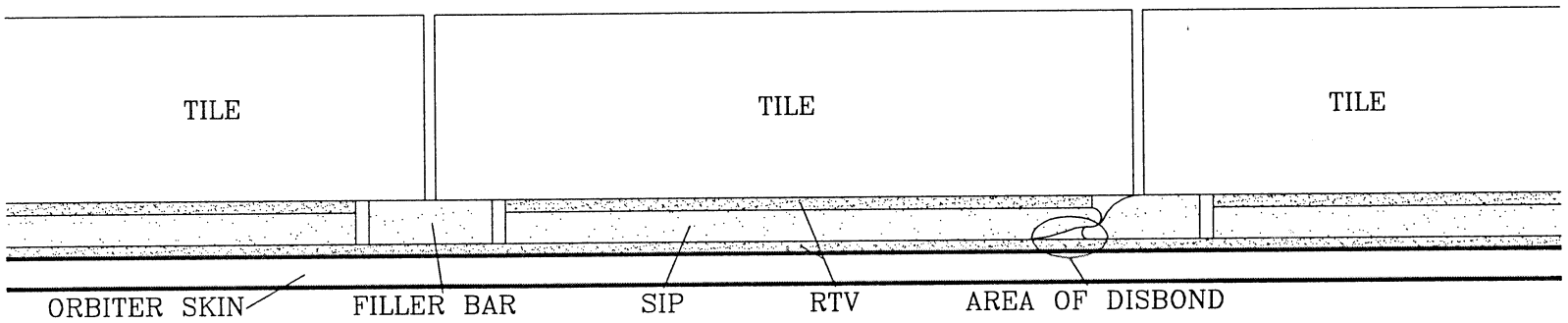

Figure 2: Disbond due to Physical Interference between SIP and Filler Bar

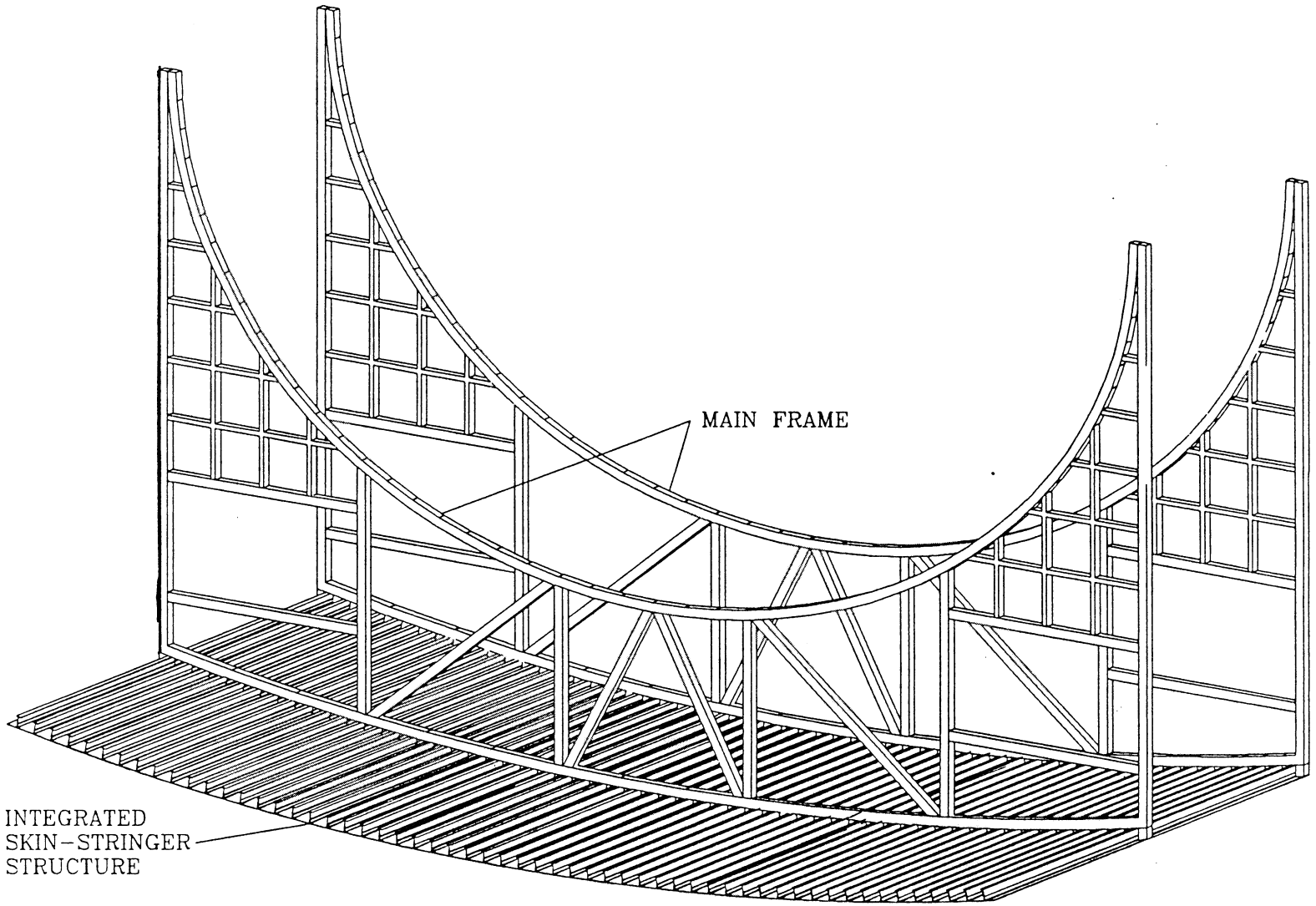

Figure 3: Mid-Fuselage Structure Section

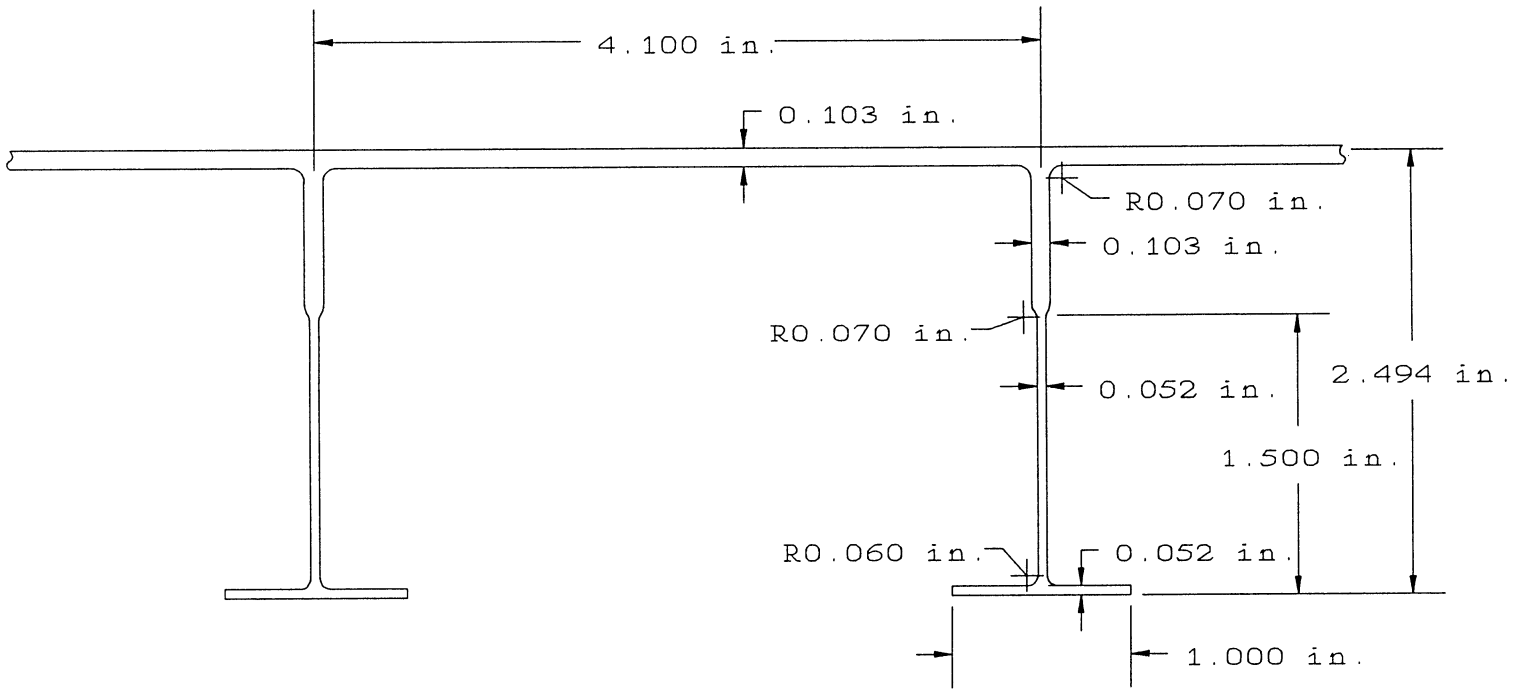

Figure 4: Typical Mid-Fuselage Skin Structure Cross-Section

3 NDE TECHNIQUE SELECTION

This section describes the theory and practicality of each NDE technique considered for tile bond verification such that each may be either qualified or dismissed.

3.1 Ultrasonic Testing

Ultrasonic testing involves exciting an object with either a pulsed or a swept frequency ultrasonic wave. The wave travels through the object, reflecting off boundaries and is recorded using an attached transducer. Transducer signals are processed by different instruments depending on the method of excitation. If there is a void within the material, an ultrasonic echo occurs which can be distinguished from the normal transducer signal. However, the amount of echo cannot be used as an interpretation of the magnitude of the discontinuity, for the amplitude of the ultrasonic echo is influenced by several factors of which discontinuity size is only one[7]. This disadvantage is coupled with the physical dilemma of having to attach a bulky transducer (about 2 inches in diameter) to the tile in order to detect any measurable signal. The outer borosilicate coating of an HRSI tile is very fragile, thus making any contact with it undesirable. These considerations diminish confidence in the feasibility of applying ultrasonic testing to the Space Shuttle.

3.2 Radiography

Radiographic testing, or x-ray testing, involves the passing of x-rays through an object such that they strike a radiographic film plate or a fluoroscopic screen. The use of a fluoroscopic screen allows real-time observation of images, although the image is very dark. In either case, any discontinuity in the object is immediately visible[8]. Thus, the size and location of discontinuity can be immediately inferred. However, x-ray examination requires an x-ray tube to be placed on one side of the object and the film plate on the other, an unacceptably complicated and time-consuming procedure for TPS tile inspection. Also, the use of x-rays around the Space Shuttle while other operations are proceeding concurrently poses an unwarranted hazard to workers.

3.3 Infrared Radiation

All bodies above a temperature of absolute zero generate electromagnetic radiation. However, the emissivity depends on the source of this radiation of the object. A high emissivity (close to 1) results from radiation emanating from the surface of the object, whereas a low emissivity (close to 0) results from radiation issuing forth from within the object. An infrared sensor is utilized to detect this radiation from which isothermal graphs may be inferred. These isothermal graphs clearly depict voids of thermal radiation[9].

A TPS tile, by design, has a very high emissivity (~.9), thus any infrared detection made will be of surface radiation. This, obviously, will not aid in the evaluation of bond condition on the underside of a tile.

3.4 Electronic Shearography

Electronic shearography utilizes a laser which illuminates the object of interest as an image shearing camera records the true image of the object superimposed with a sheared image of the object vibrating under acoustic energy. This produces contours of slope of out-of-plane displacements (see Figure 5). The advantages of this non-contact technique are: real-time inspection, high inspection rate, full field video presentation, and user friendliness. However, fringe resolution and clarity are limited and the interpretation of fringes can be ambiguous (fringes do not represent mode shape). Also, shearography favors testing TPS tiles at lower frequencies (below 500 Hz).

3.5 Experimental Modal Analysis

Experimental Modal Analysis (EMA) involves the excitation and response measurement of a discretized domain. Transfer functions between discrete nodes provide the information from which modal parameters (i.e. natural frequencies and mode shapes) may be inferred. The natural frequencies and mode shapes of an object are governed by its mass and stiffness. Thus, a change in either the mass or stiffness of an object precipitates a change in the modal parameters. The extent of change in modal parameters depends on both the severity and location of mass/stiffness fluctuation. Also, specific mass/stiffness changes will affect each vibration mode differently. For instance, in the RSI tile case, loss of bond may affect an out-of-plane vibration mode vastly more than an in-plane vibration mode. The dependence of modal parameter changes on the character of mass/stiffness variation is the basis for identification of damage.

The idea of using vibration characteristics to detect and locate damage in structures has been widely explored (e.g. Stubbs and Osegueda[10], Springer *et al.*[11], Hearn and Testa[12], Chen and Garba[13], Rizos *et al.*[14], Moslehy *et al.*[15]). However, the research reported herein is based on Moslehy *et al.*[15] who introduced the first successful modal testing and analytical modeling to the specific task of TPS tile bond evaluation.

The analytical model describing the eigenvalue problem for undamped systems can be stated in terms of the system stiffness and mass matrices $[K]$ and $[M]$, the ith eigenvalue ω_i^2, and the corresponding eigenvector $\{\phi\}_i$ as follows:

$$\left[[K]-\omega_i^2[M]\right]\{\phi\}_i=\{0\} \tag{1}$$

Small changes in stiffness $[K]$ or mass $[M]$ produce small changes in ω_i^2 and $\{\phi\}_i$. For the perturbed system, equation (1) becomes

$$[[K]+[\Delta K]]-\left(\omega^2+\Delta\omega_i^2\right)[[M]+[\Delta M]]\left\{\{\phi\}_i+\{\Delta\phi\}_i\right\}=\{0\} \tag{2}$$

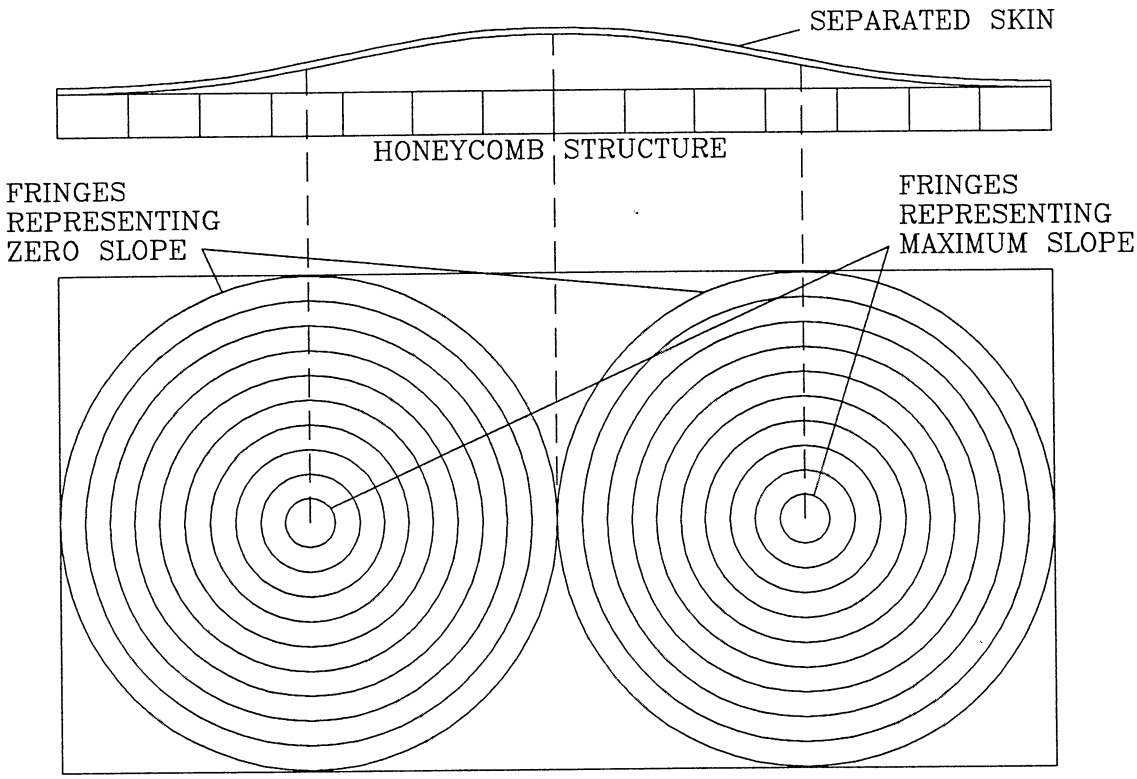

SCHEMATIC OF FRINGE CONTOURS REPRESENTING
CONSTANT SLOPE OF OUT-OF-PLANE DISPLACEMENTS

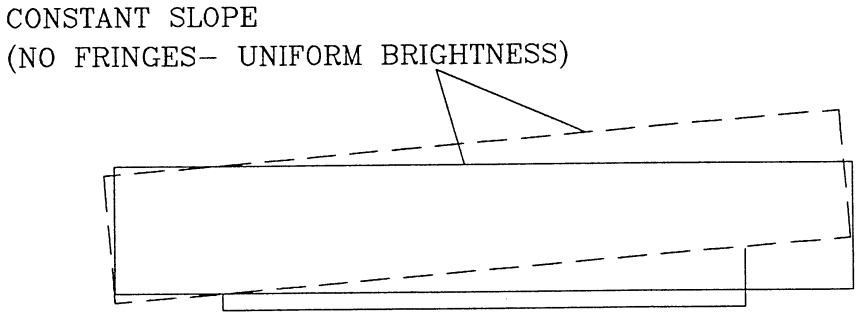

SCHEMATIC SHOWING ROCKING MOTION OF TILE

Figure 5: Shearography

If it is assumed that the damage of the structure in question will affect only the stiffness, not the mass, then $[M]$ can be neglected. Also neglecting second-order terms, equation (2) gives[12]

$$\Delta\omega_i^2 = \frac{\{\phi\}_i^T[\Delta K]\{\phi\}_i}{\{\phi\}_i^T[M]\{\phi\}_i} \tag{3}$$

which is the change of the ith natural frequency due to a change in the global structural stiffness $[K]$. This theoretical relationship between stiffness change and natural frequency change has been demonstrated experimentally in many instances. Hearn and Testa[12] performed two experiments to this end. In the first, a four-member welded steel frame was subjected to cyclic loading, and modal parameters were observed as progressive damage resulted from fatigue cracking. At every 10,000 load cycles, the frame was inspected for cracks by modal analysis and verified using dye-penetrant testing. A total of 20 response measurements were made at each interval; a history of the first six natural frequencies was developed. Results reveal a drop in each frequency whenever a new crack was discovered, which correlated to the change in frequency predicted by the analytical model. In their second experiment, they measured the effects on modal parameters of wire ropes in tension which were damaged by transverse sawcuts. Again, results agreed with predictions of the analytical model.

Similar work on beams was performed by Springer *et al.*[11] & Stubbs and Osegueda[16]. Natural frequencies were used not only to predict the amount of damage suffered, but also the location of the damage. The analytical models they employed yielded errors of less than 10% for a variety of beams.

3.6 Application to TPS Tiles

The well known technique of EMA utilizes an impact hammer or mechanical shaker to excite the structure. This is not practical, since such methods can damage the TPS tile, even under laboratory conditions. Hence, an alternate method of excitation must be used. The simplest choice is the use of acoustical energy[15]. Although simple, there are considerations to be made, most notably the type of signal to be used. Modal analysis in this research was performed with random noise, but a better signal type may be a chirp function.

The second variation to the conventional EMA technique involves a substitute for an accelerometer to make vibration measurements. Although in the laboratory an accelerometer poses no threat to a TPS tile, continuous attachment of an accelerometer to the fragile emissivity coating of TPS tiles in the field can cause damage to the tiles. There exists a non-contact technique which may fulfill this particular dilemma. The method investigated in this research is laser doppler velocimetry (LDV), which is explained in Section 5.

It is concluded that the modal analysis technique holds the most promise for the task of non-destructively evaluating Space Shuttle TPS tile bond integrity. Thus, modal analysis is pursued in finite element simulation as well as experimental testing.

4 FINITE ELEMENT MODELING

The NISA finite element computer code[17] was used on a 50 Mhz 486 PC to analyze the FE models developed for different TPS tile assemblies. In the analysis, the actual material properties of TPS components were used. All tile assembly components were modeled using 8-node brick elements. When employed, the skin structure was comprised of 4-node plate elements.

A typical FE mesh of a single-tile assembly on clamped structure is illustrated in Figure 6. The mesh is mostly defined by physical properties of the tile assembly. For example, the edge between the 6 x 6 inch tile and the 5 x 5 inch upper RTV layer requires that a line of nodes be modeled on the tile. Also, in the case where multiple tiles are modeled in a staggered formation, the edge of one tile must meet a line of nodes on adjacent staggered tiles. The edge of the tile on which a finer mesh is used is the edge on which disbond is modeled; a line of nodes is required at each possible edge of disbond (see Figure 7). The high aspect ratio of some elements of the mesh has been tested separately and was found to produce acceptable results with the finite element code used.

Some model variables have already been mentioned. Not only are there several physical variables which must be simulated, but also the application of finite element analysis itself sometimes demands approximations to be made and prompts the consideration of different modeling avenues.

Unless otherwise noted, the tile modeled in finite element analyses is tile# 191025-299 on OV-102 (Columbia) as this is the tile which was analyzed most in hands-on tests performed on the shuttle at Rockwell International in Palmdale, California (see Section 5).

4.1 Constraints

Constraints are one of the first considerations which need to be addressed when using the finite element method. Any model analyzed using the finite element method must be properly "anchored" such that infinite accelerations or singularities are not produced.

In modeling a tile assembly, there are no direct constraints, thus it must be determined how to "anchor" the tile assembly. In the most conservative scenario, one would model an entire Orbital Vehicle and constrain the landing gear (this is even an approximation). On the other side of the spectrum, the best assumption to make in order to reduce model size and computation time is that the skin to which the tile assembly is mounted can be assumed rigid. If this is so, all the nodes on the bottom surface of the tile assembly may be constrained (for 100% bond), and no modeling of additional structure is required. It is obvious that there is a direct trade-off between modeling accurate constraints and model size and computation time.

The most efficient method to determine if clamped structure is a realistic assumption is to create two models, one in which the tile is attached to clamped structure and the other in which the tile is mounted on a reasonable section of the OV. Orbital Vehicle.

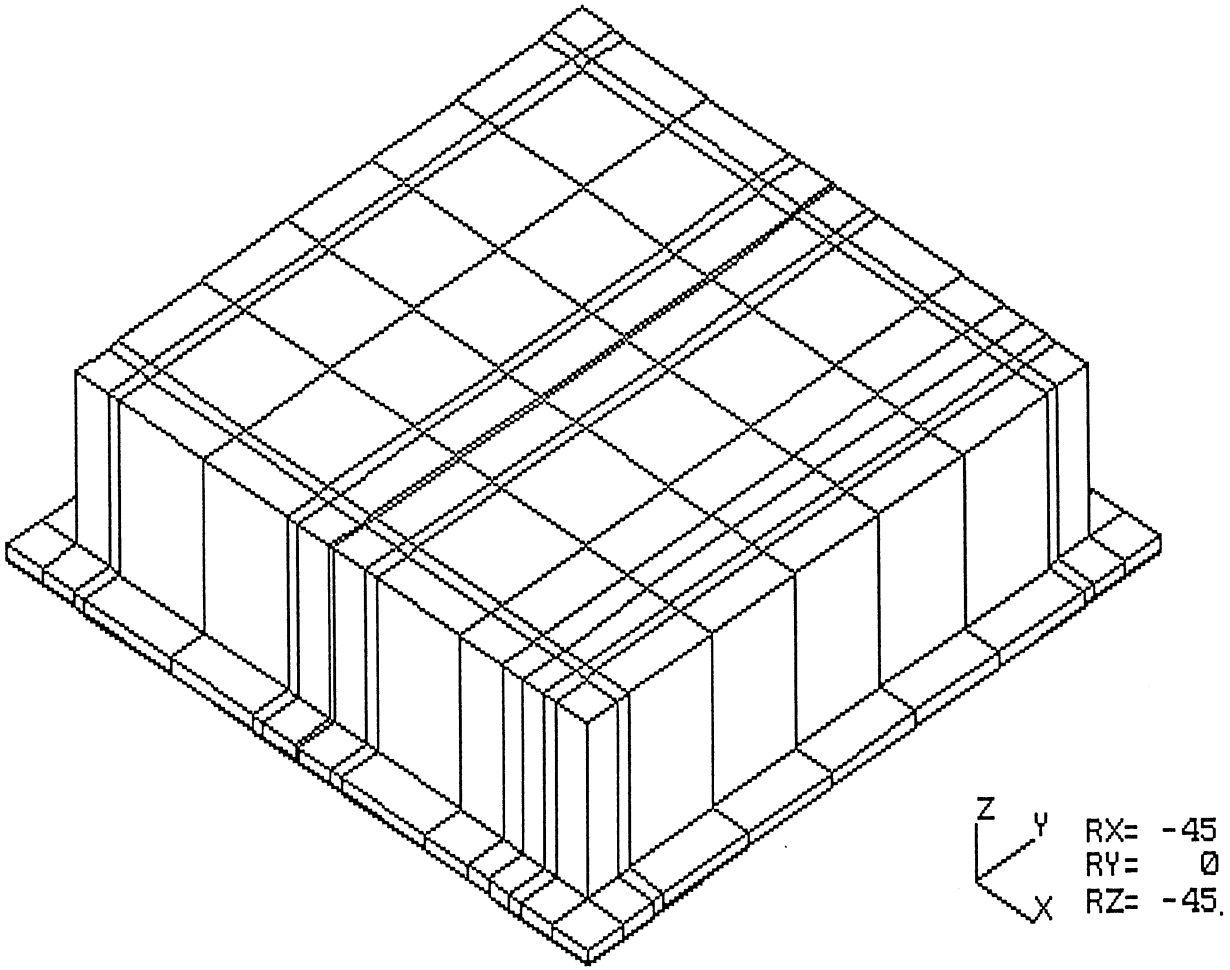

Figure 6: Typical Single-Tile Mesh

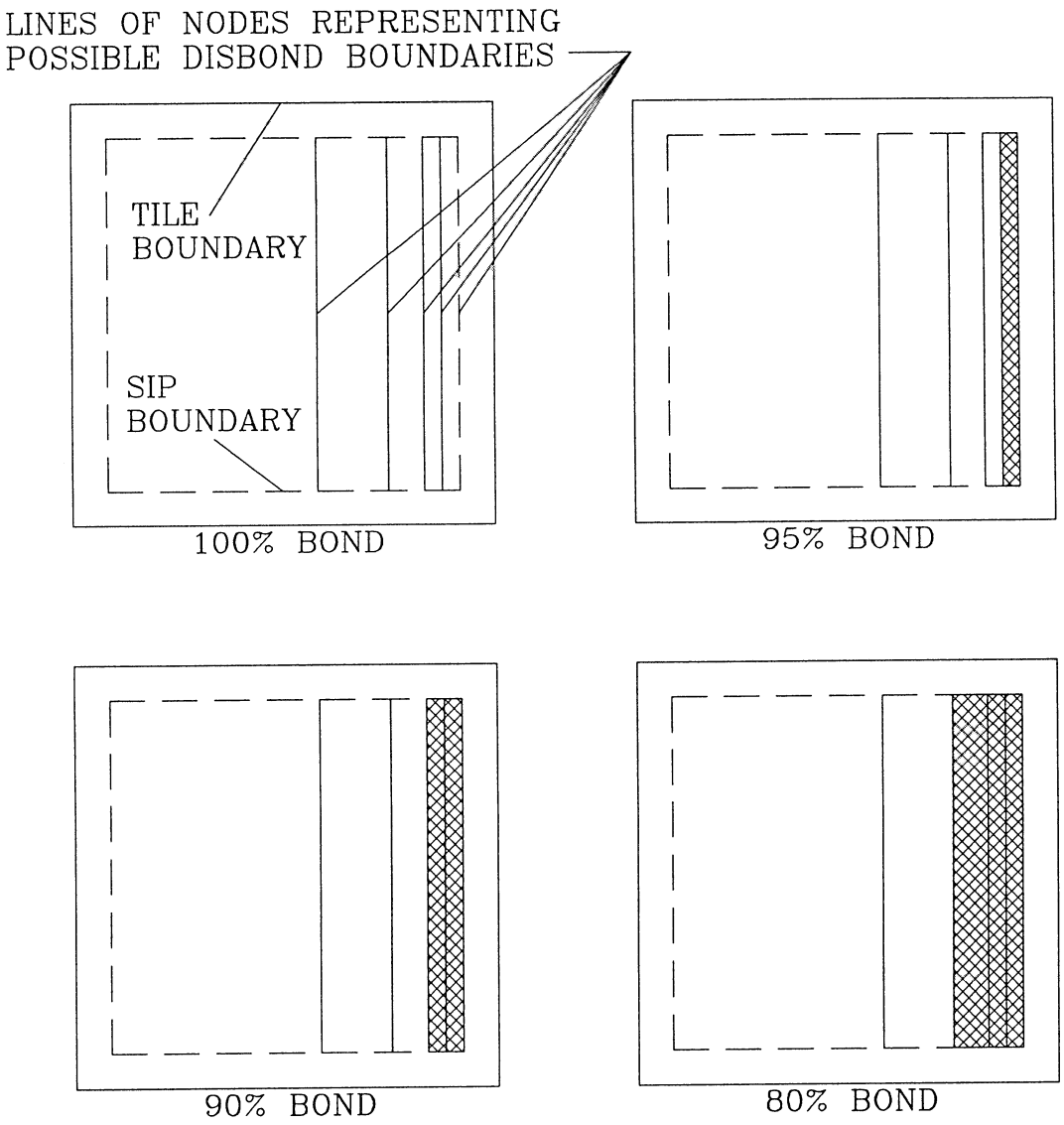

Figure 7: Disbond Areas and Required Lines of Nodes

The manner in which a "reasonable section" is chosen is to consider all structure radiating from the tile assembly until a significant rise in stiffness is encountered. Structure to this point is modeled and constraints are imposed at the "cut" where the stiffening structure normally exists.

4.2 Structure Modeling

The skin structure type chosen for modeling was that of the mid-fuselage as this is one of the least stiff sections of skin structure on the Orbital Vehicle. Examining a tile assembly mounted on this structure, it was found that the closest large rise in stiffness occurs at the fuselage main frames (see Figure 3). Thus, the model of the tile assembly plus structure, also referred to as extended structure model, includes the tile assembly mounted on the 57 inch length of structure between main frames. At either end of this structure, the nodes were constrained.

Examination of the mid-fuselage structure provides constraint information which resolves the structure in the longitudinal direction, however there are no criteria which prescribe the width of the structure which should be modeled. Thus, another variable was introduced and had to be modeled. Noting that the stringers run longitudinally, a sensitivity analysis was required to determine the
number of stringers which should be modeled to provide an accurate stiffness at the tile assembly location. Consequently, analyses of structure alone consisting of 2, 4, 8, 12, 16, and 20 stringers were performed (results in Section 5).

4.3 Bond Condition Modeling

The most important variable to be modeled is the amount of disbond associated with a tile. For the finite element analyses performed, bond conditions of 100%, 80%, and 60% were modeled. Disbond was modeled along an edge parallel to the Roll axis of the tile assembly in all models unless noted otherwise.

Disbond is considered to occur along any edge of a tile at the SIP-structure interface. The edge used to model any disbond can be discovered by noting which edge has a finer mesh (refer to Figures 6 and 7). Along this edge, each line of nodes extending from each edge of the RTV represents the edge where bond might end and disbond begins. The method in which disbond was modeled depended on whether or not structure was included in the model.

In the case where no structure was included in the model, the bottom layer of nodes were constrained. Thus, to simulate disbond, these rigid constraints were removed at the proper nodes for the amount of disbond prescribed. The "proper nodes" can be visualized by referring to the disbond edge of Figure 6. Removing the constraints from the 6 nodes along the bottom edge of the lower RTV would produce a simulated disbond of 5%. Removal of additional lines of constraints results in simulated disbonds of 10%, 20%, and 40%, respectively.

When the structure is included in the model of the tile assembly, there are no constraints to lift at the nodes in the area of disbond. Rather, these nodes belong to elements of both the lower layer of RTV and the skin structure immediately below. Thus, to simulate disbond, double nodes were created at the proper nodes. That is, two nodes were created to coexist at the exact same location, each belonging to a different element (see Figure 8). This produced a situation where the nodes of interest of neighboring elements perfectly overlapped when undisplaced, however, since there was no longer any stiffness between the nodes, they could vibrate freely with respect to each other. This could result in a physically impossible situation - one element can vibrate into another element without resistance (i.e. penetration). However, in the actual physical system, the slight residual tension the SIP experiences after installation causes a slight separation between the SIP and structure in an area of disbond. Thus, these neighboring elements should be able to vibrate free of one another. In the finite element analysis, this translates into the tile being allowed to penetrate the structure. It is worth noting that eigenvalue results do not provide amplitudes of vibration, only mode shape vectors. Thus, in any case, the FEA results do not depict the actual tile displacement.

The location of the disbond edge with respect to the tile axis system is another variable, affected by the orthotropic properties of the tile assembly components. Vibration characteristics of the tile assembly might be expected to be axis independent until the realization is made that the material properties are different in each axis direction. Thus, it is anticipated that not only will the vibration characteristics vary between axes, but also that the changes in vibration characteristics due to disbond will vary. Consequently, a disbond along each axis was modeled. The axes are described mathematically as X and Y, corresponding to the Cross-Roll and Roll axes, respectively.

4.4 Filler Bar Modeling

The filler bar poses an interesting dilemma, partially due to a limitation of the NISA finite element code. Recalling the description of filler bar installation from Section 2, the filler bar is in contact with the RSI tile only by virtue of the compression precipitated by the installation process. This delineates a possibly non-linear condition - the filler bar resists downward motion of the RSI tile, but may not influence any upward motion if contact is lost. Unfortunately, the NISA finite element code utilizes linear mathematical models in vibration analysis calculations. Thus, we are left with two options: (1) model the filler bar fixed to the RSI tile by virtue of common nodes, in which case RSI tile motion in all directions is resisted and (2) do not model filler bar at all, in which case it is assumed that the filler bar provides negligible stiffness to the RSI tile in all directions. As this is a quandary due to the analytical model, an experimental analysis was required to determine the true affect of the filler bar and to interpret finite element results (see Section 5).

A further consideration of the filler bar is its role in tile interaction. That is, if it is found that filler bar must be modeled to produce the proper stiffness of a tile assembly, it must be determined if there is interaction in the physical case between tiles through the filler bar as would be the case in the finite element analysis of a 10-tile model. This again required finite element models of both cases as well as experimental testing to serve as an interpreter. It is

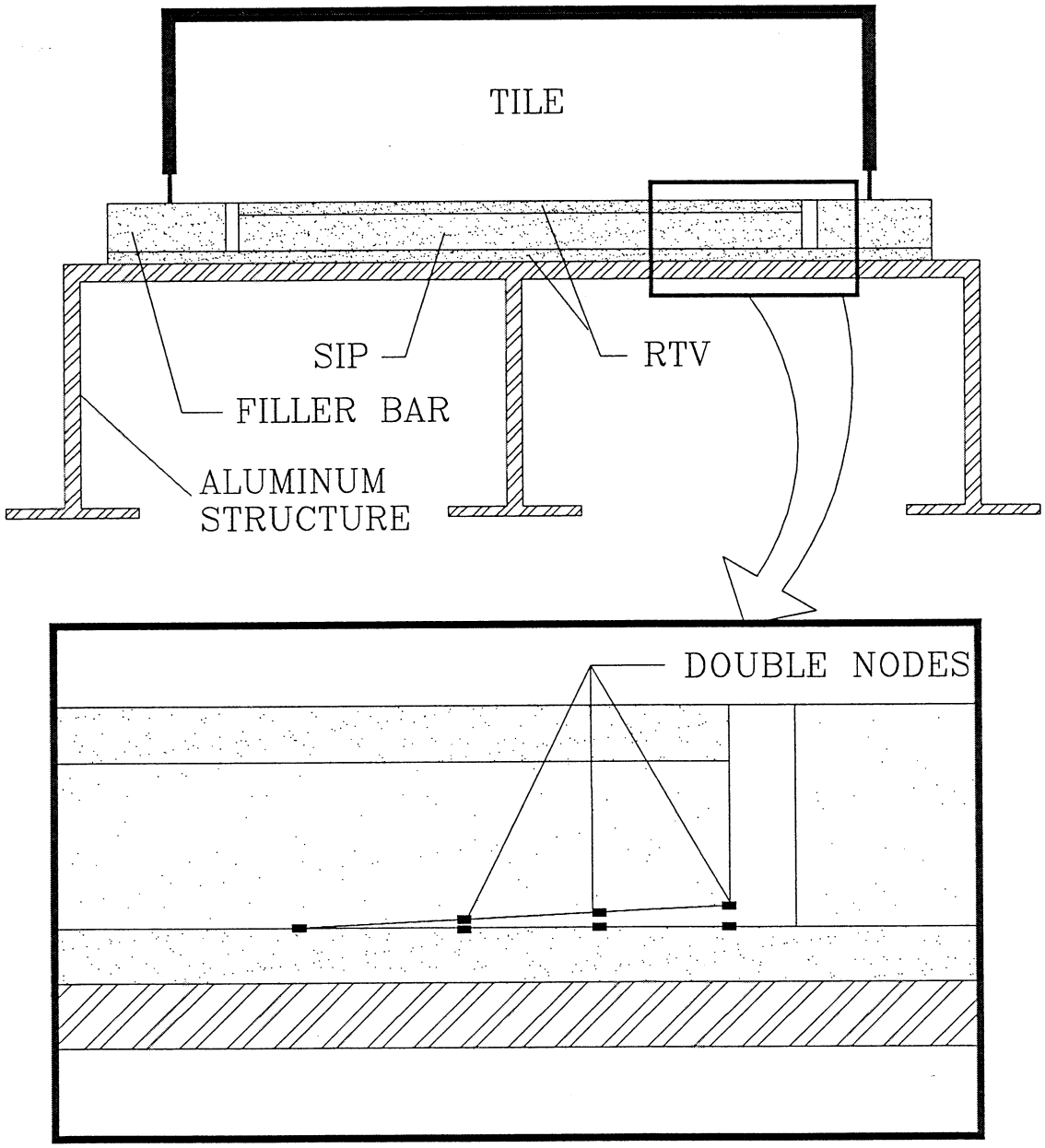

Figure 8: Disbond Modeling

noted that a finite element model of a 10-tile assembly with no filler bar is equivalent to a single-tile assembly if a clamped structure is assumed.

4.5 10-Tile Modeling

As stated in the above section, the requirement of multiple tiles to be modeled is largely dependent on the properties of the filler bar. In a model including multiple tiles, the additional "dummy" tiles were modeled similarly to the tile of interest with the mesh depending on geometric demands (see Figure 9 for 10-tile/clamped structure model mesh).

There are instances where multiple tiles do not need to be modeled completely, however any model including extended structure might require the mass of all the tiles on the structure to be modeled. All tiles which are not required to be specifically modeled geometrically may need to be modeled as point masses such that the vibration of the structure is affected accurately. Thus, a model with point masses was analyzed, and results were compared to models without added point masses.

4.6 Types of Analyses

Initial analyses of all models were linear eigenvalue analyses which provided free vibration modal information. Comparison of natural frequencies and mode shapes were used to determine the affects of variables, most notably, bond condition. Ensuing analyses of models of interest involved frequency response calculations to simulate the response of models of interest to acoustic energy applied as pressure to the top surface of the tile of interest (see Figure 10). A pressure loading equivalent to 100 dB of sound was used (0.00029 psi) at frequencies swept from 100 to 3500 Hz. Displacement, velocity, and acceleration results were extracted for nodes at the corner and center of the tiles of interest.

5 EXPERIMENTAL ANALYSES

Experimental analyses were used as a verification of finite element results as well as a hands-on trial of different experimental techniques for effectiveness in non-destructively measuring natural frequencies and mode shapes. This section outlines the experimental methods employed. Results are presented in Section 7.

5.1 Experimental Modal Analysis

A slight variation of the conventional EMA was performed on select test panels at the experimental mechanics laboratory at UCF. The tiles at the UCF laboratory were of varying sizes and unknown physical properties and bond conditions. A speaker was used to generate narrow band (1000 Hz) random noise between 200 and 1200 Hz; an accelerometer, a SMS structural dynamics system, a Hewlett Packard spectrum analyzer, and a Hewlett Packard microcomputer were used to perform modal analysis of the tile of interest. The EMA set-up is

OR

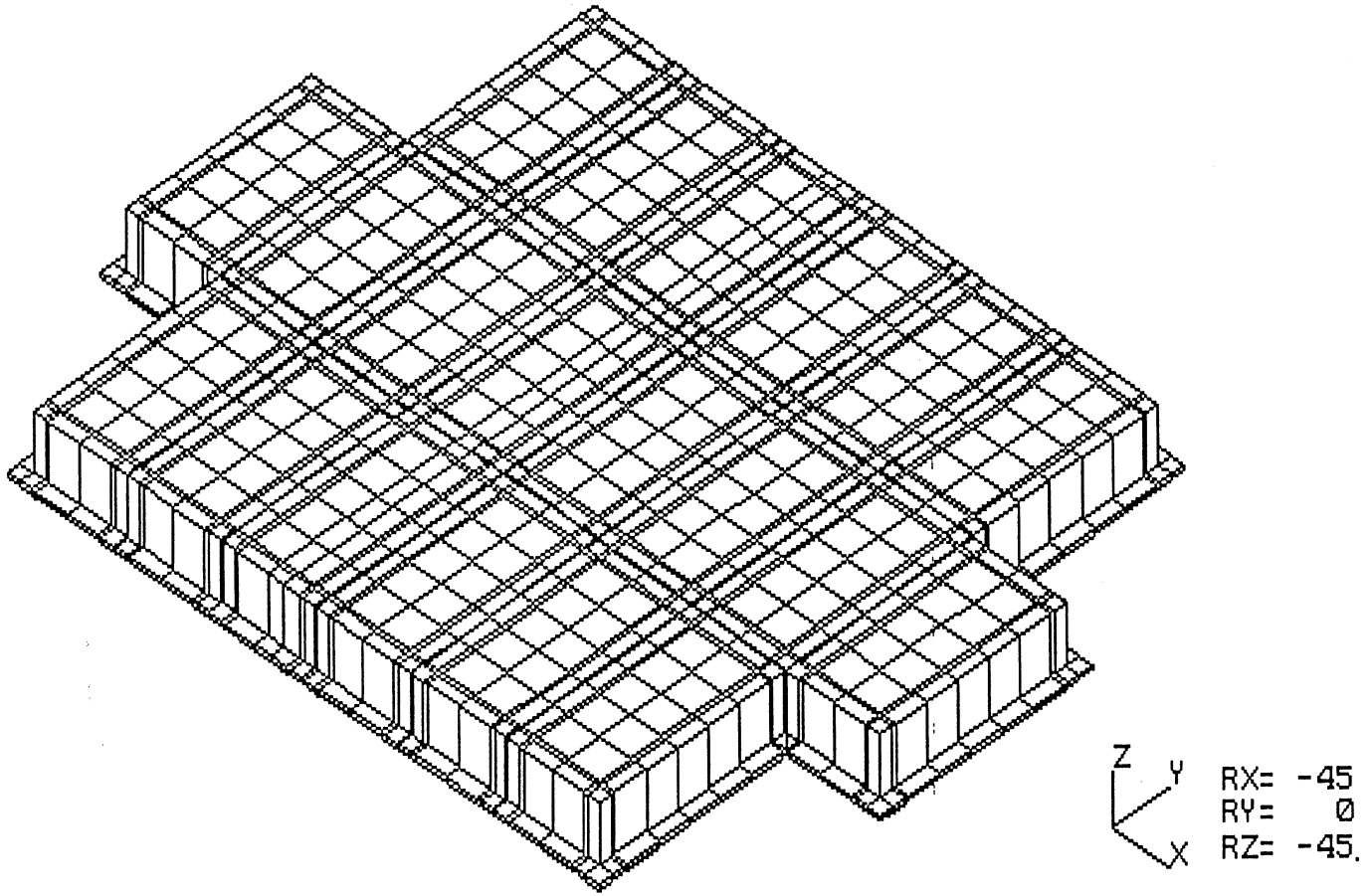

Figure 9: 10-Tile / Clamped StructureModel Mesh

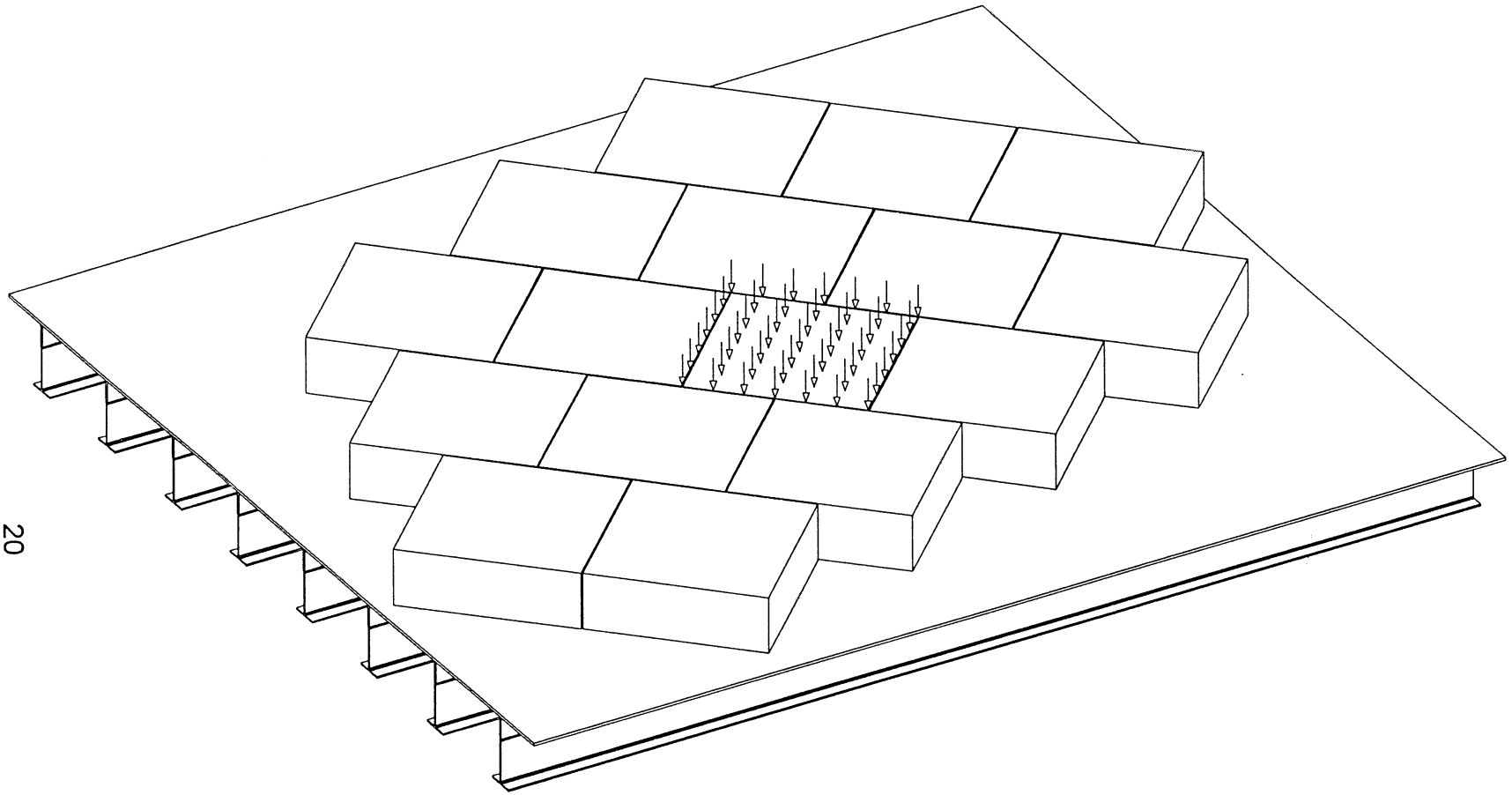

Figure 10: Pressure Application for Forced Response

illustrated in Figure 11. Natural frequency results were recorded. It is noted that EMA testing at UCF only serves to justify modal analysis as a measurement technique using acoustic energy. Also, because the accelerometer was placed on the top surface of the tile, only modes producing vertical acceleration were recorded.

The effect of filler bar was also determined through the same EMA procedure. A 6 x 6 x 2.4 inch tile at the UCF laboratory was tested with and without filler bar, with natural frequency results being recorded.

5.2 Frequency Response

Frequency response testing was performed on tiles at UCF as well using a speaker, accelerometer, digital oscilloscope, and Hewlett Packard spectrum analyzer. The experimental set-up was similar to that of the EMA set-up in Figure 11 with the exception of no modal analysis computers. The accelerometer was placed at both the center and corner points of the tile, and the acoustic frequency was swept over a range of 10 to 2000 Hz. Accelerometer output was monitored, and resonant frequencies were recorded. As with the EMA testing, it is noted that because the accelerometer was placed on the top surface of the tile, only modes producing vertical acceleration were recorded.

5.3 Holographic Interferometry

Holographic testing was performed at UCF to assess its feasibility as a non-contact measurement technique to determine natural frequencies and mode shapes. Holographic interferometry is capable of measuring very small displacements (~.3 m) of an object. Proper application of this technique produces a fringe pattern depicting mode shapes at corresponding natural frequencies. A disadvantage of holography in the application to the TPS tile evaluation task, however, is the long set-up time required and the requirement for vibration isolation. In the test conducted at UCF, a 60 mW Helium-Neon laser, a holographic camera, various optics, and a speaker were used to perform both real-time and time-average holographic interferometry on a TPS tile assembly.

5.4 Rockwell-Palmdale Testing

The purpose of the testing performed at the Rockwell International facility in Palmdale, California was to assess the feasibility and practicality of employing different non-contact techniques to ascertain the bond condition of shuttle TPS tiles[18]. Tested tiles were on the aft underside portion of the left wing of OV-102 (Columbia). An illustration of tiles tested is shown in Figure 12 and physical properties of tiles tested are given in Table 2. Subsequent to experimental testing, the tiles of interest were removed using a hot wire and a nonmetallic scraper for expert inspection to determine actual bond condition.

5.5 Shearography

Shearography testing was performed on the Space Shuttle Columbia at Rockwell International in Palmdale, California with a Laser Technology Incorporated (LTI) system at

frequencies which were swept from 50 to 500 Hz in 5 seconds at 110 dB[18]. A videotape of results was recorded during testing.

5.6 Ometron VPI Testing

The Ometron Vibration Pattern Imager (VPI) system is a laser doppler velocimeter which is capable of making rapid velocity profile measurements over a user-defined area (see Figure 13). Coupling with a speaker and signal analyzer allow modal testing to be performed. The test performed involved a rapid single-point frequency response survey of 13 tiles and a 36 point modal analysis of tile# 191025-299. Frequency response plots and mode shapes were recorded (see Section 7).

Table 2: Physical Properties of Tiles Tested at Rockwell International-Palmdale

Tile Number	Tile Material	IML Area (footprint)	Thickness (in.)		
			Tile	SIP	RTV
191025-299	LI-900	35.66 sq. in.	2.07	0.16	0.01
191025-300	LI-900	35.64 sq. in.	2.02	0.16	0.01
191026-030	LI-900	35.73 sq. in.	2.44	0.16	0.01
191026-059	LI-900	35.66 sq. in.	2.15	0.16	0.01
191026-061	LI-900	35.63 sq. in.	2.04	0.16	0.01
191026-064	LI-900	35.66 sq. in.	2.22	0.16	0.01
191026-067	LI-900	35.70 sq. in.	2.36	0.16	0.01
191026-071	LI-900	35.71 sq. in.	2.4	0.16	0.01
191026-075	LI-900	35.66 sq. in.	2.3	0.16	0.01
191026-076	LI-900	35.70 sq. in.	2.39	0.16	0.01
191026-077	LI-900	35.66 sq. in.	2.33	0.16	0.01
191026-135	LI-900	23.73 sq. in.	2.46	0.16	0.01
191026-161	LI-2200	35.66 sq. in.	2.27	0.16	0.01
191026-237	FRCI-12	35.69 sq. in.	2.36	0.16	0.01
191026-239	FRCI-12	35.68 sq. in.	2.34	0.16	0.01
191026-243	FRCI-12	35.65 sq. in.	2.15	0.16	0.01
191026-256	FRCI-12	35.64 sq. in.	2.08	0.16	0.01
191026-257	FRCI-12	29.65 sq. in.	2.1	0.16	0.01
192131-057*	LI-2200	35.65 sq. in.	2.22	0.16	0.01
192158-079*	LI-900	35.67 sq. in.	2.29	0.16	0.01

Legend

* Instrumented Tiles

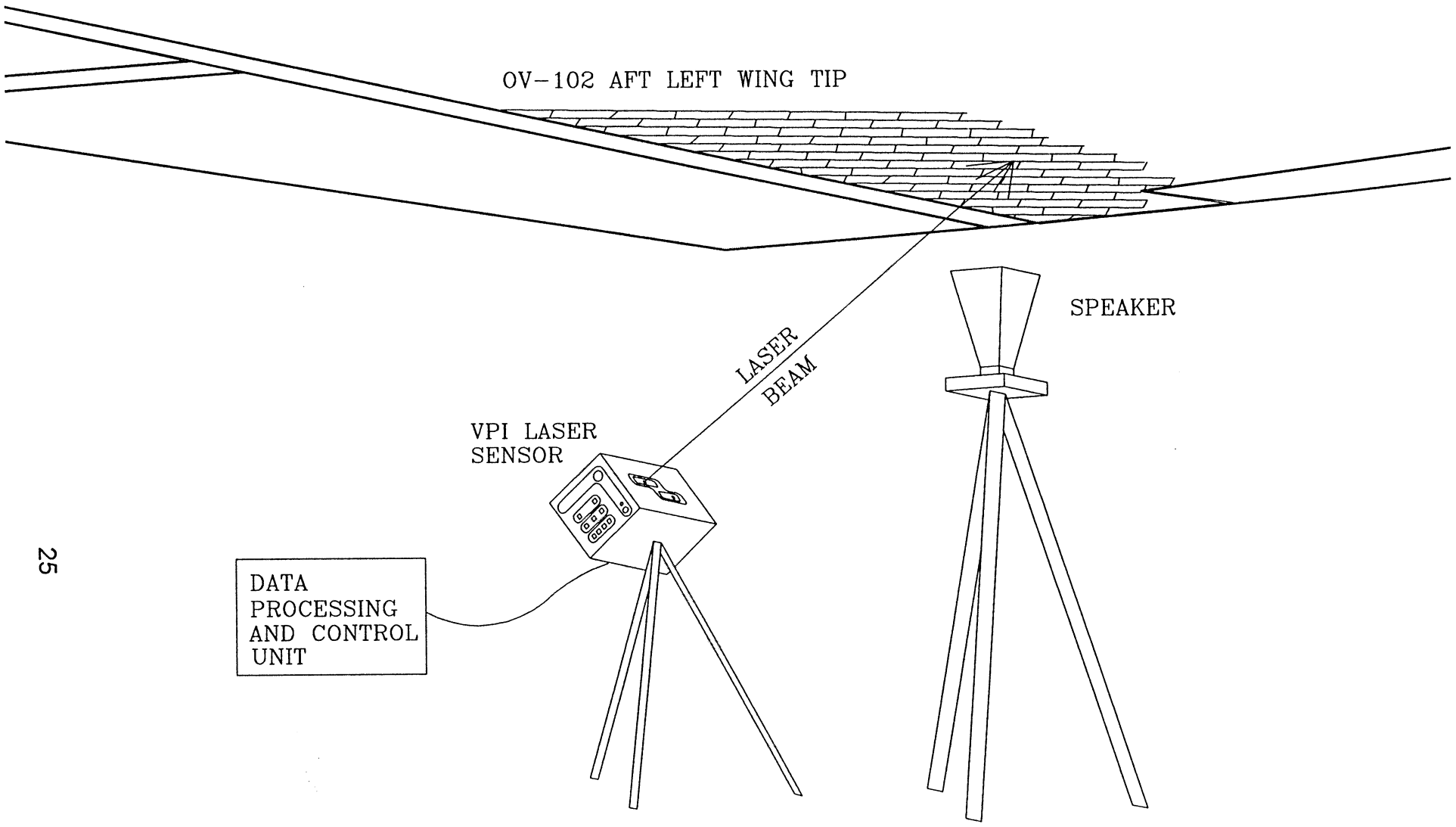

Figure 13: Ometron VPI Test Set-Up at Rockwell-Palmdale Facility

6 FINITE ELEMENT RESULTS

The first finite element analyses were performed to demonstrate the affect of disbond on natural frequencies. The FE model used was of tile# 191025-299 from OV-102 with filler bar mounted on a clamped structure. Figure 14 illustrates the mesh of this model. The 100% bond case model has 2640 degrees of freedom (DOF) and 528 elements and used 7 minutes of CPU time. Referring to Table 3 and Figure 15, it is noted that natural frequencies for all modes drop with an increase of disbond. Knowledge beforehand of these numbers would enable a test engineer to accurately quantify the amount of bond for this particular tile from modal test data. In addition, the location of disbond could be determined upon observation of the tile mode shapes as illustrated in Figures 16, 17, and 18. The tile mode shape which is most affected by the change in stiffness is the rocking mode about the axis parallel to that of the disbond. In this case, mode# 5 for the 80% and 60% bond cases demonstrates the most dramatic change. Note that the rocking motion in the 100% case is symmetric about the center of the tile. In the 80% and 60% bond cases, the axis of rotation is shifted away from the area of disbond such that the tile above the area of disbond undergoes increased motion. The line of zero motion (the rotation axis) is a clear indicator of the location of disbond. This particular model is of a single-tile assembly with filler bar and a clamped structure assumption, however the decrease in natural frequencies and shifts in mode shapes exist for all tile assembly FE models.

The next variable examined was the axis along which the disbond occurs. Tile# 191025-299 was modeled with filler bar for this case as well, and new results are listed with results from Table 3 for comparison. Model size and run time remained unchanged between models of dissimilar disbond location. As anticipated, a slightly different change in natural frequency is encountered due to the orthotropic properties of the tile assembly (see Table 4). The mode shape distortion due to disbond along either edge was the same, with the exception of axis of rotation. Mode shapes remained consistent with Figures 16, 17, and 18. Questions concerning model constraints were next addressed. To this end, a comparison of FEA of a single-tile assumed to be rigidly supported and a single-tile mounted on the extended structure described earlier was performed. First, however, a sensitivity analysis was performed to determine the size of structure required in order to have accurate dynamic qualities.

FEA of the structure only was performed with the structure varying in width from 2 to 20 stringers. Model size varied, obviously, with the number of stringers modeled (5256 DOF & 360 elements for 8-stringer model). However, CPU time required was no more than 10 minutes. Results of the first natural frequency (out-of-plane flexing) are presented in Figure 19. A typical mode shape (for an 8-stringer model) is shown in Figure 20. These results determined thenumber of stringers to be used for tile/extended structure models. Upon analysis of the results, it was noted that the first natural frequency did not significantly vary with more than 8 stringers, hence 8 stringers were used in extended structure modeling.

Next, tile# 191025-299 with filler bar on extended structure was modeled (see Figure 21 for mesh). The 100% bond case model possesses 18330 DOF and 3135 elements, and

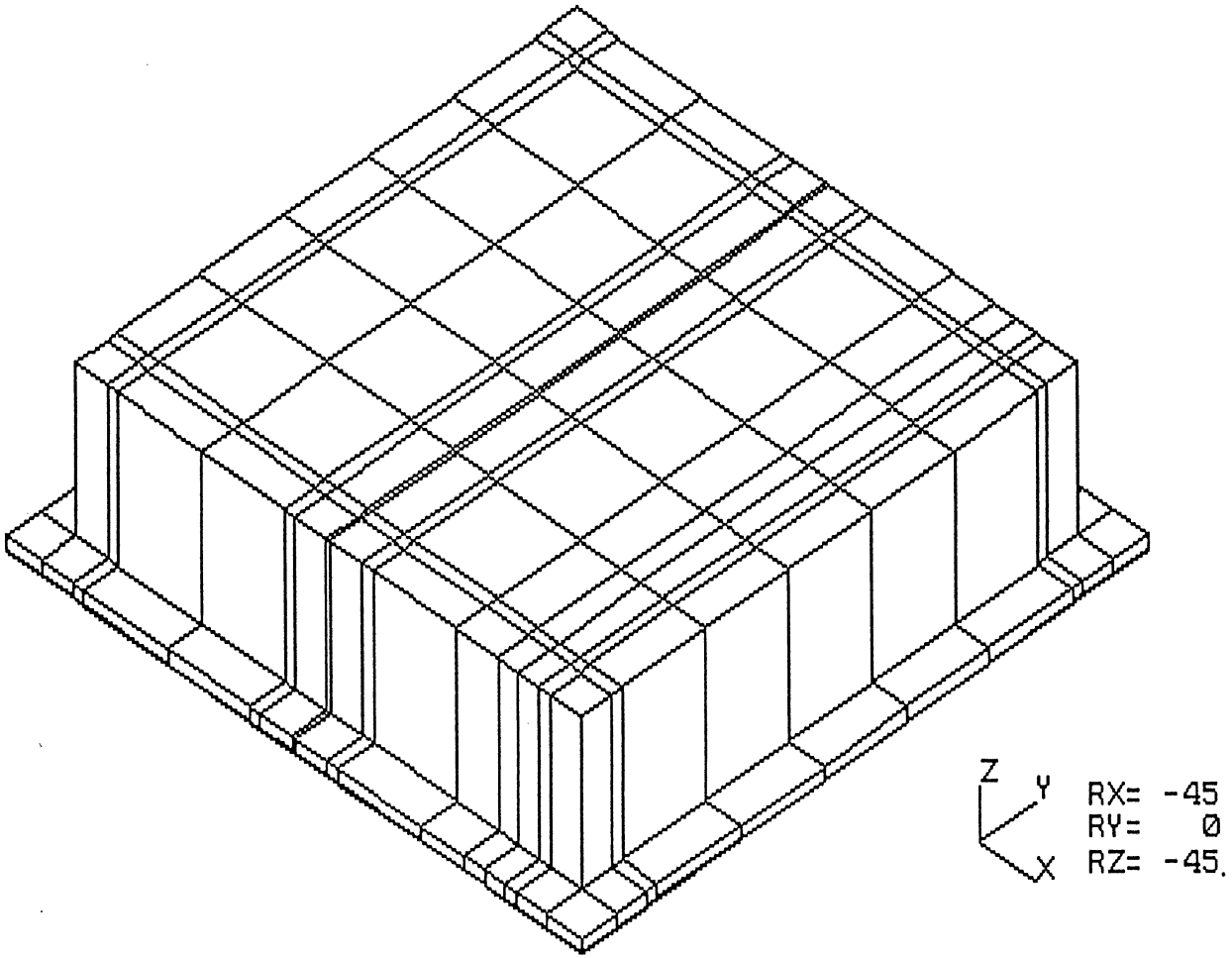

Figure 14: STA00F.EII

Table 3: FEA Results of Tile# 191025-299 at Percentage Bond

Mode #	Natural Frequencies (Hz)			Mode Shape Description
	100% Bond	80% Bond	60% Bond	
1	480	449	409	TX
2	487	450	416	TY
3	525	505	495	ROT
4	1016	850	728	RY
5	1020 (P)	969	905	RX
6	1025 (RX)	1013	1001	P
7	1489	1439	1423	F
8	1898	1865	1847	F
9	2031	2009	1981	F
10	2371	2350	2341	F

Legend

TX: Rigid Body Translation of Tile in X-Axis Direction
TY: Rigid Body Translation of Tile in Y-Axis Direction
ROT: Rigid Body Rotation of Tile about Z-Axis
RX: Rigid Body Rocking of Tile about X-Axis
RY: Rigid Body Rocking of Tile about Y-Axis
P: Rigid Body Translation of Tile in Z-Axis Direction (Piston Mode)
F: Flexing of Tile

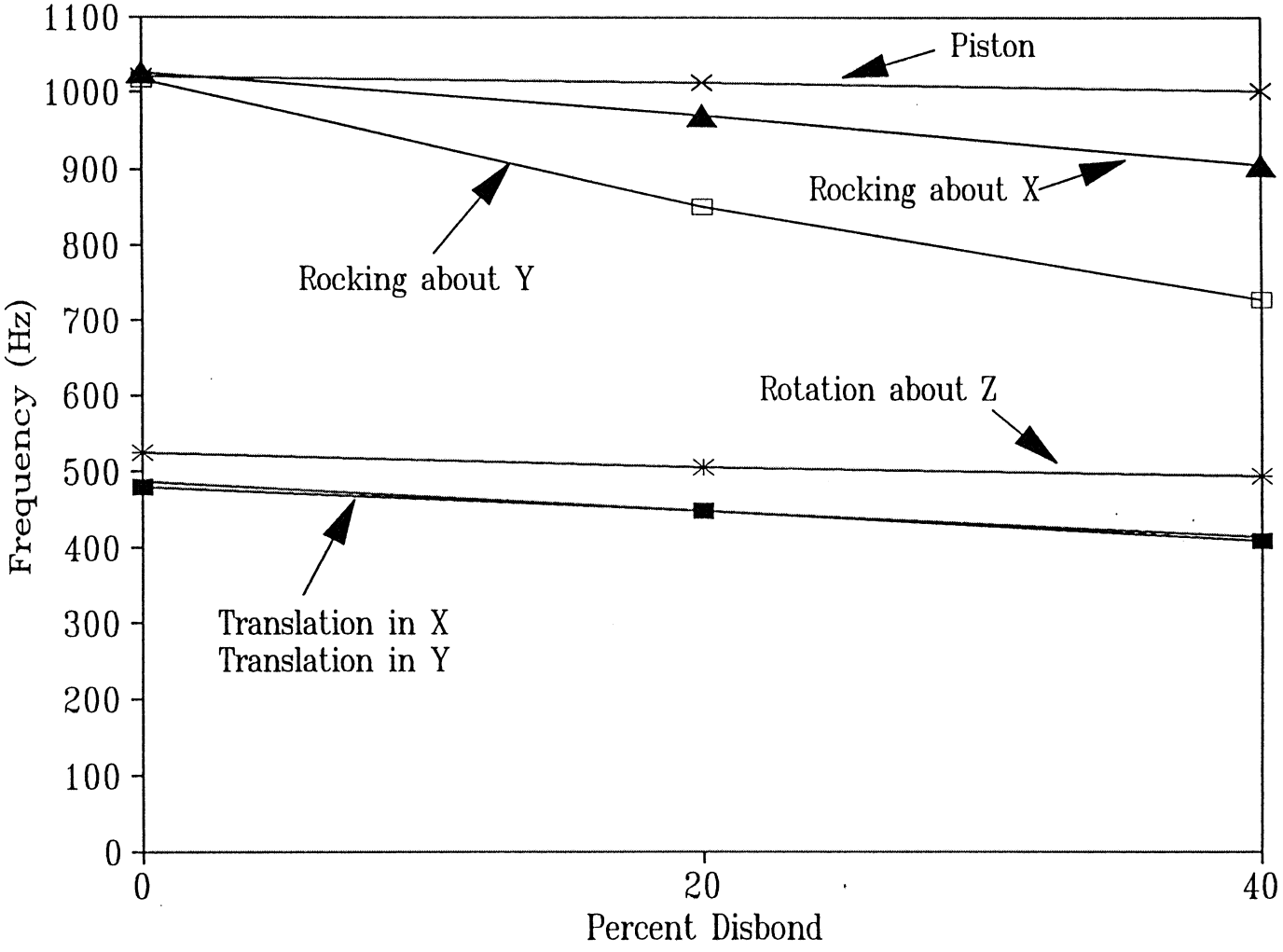

Figure 15: Frequency vs. % Disbond

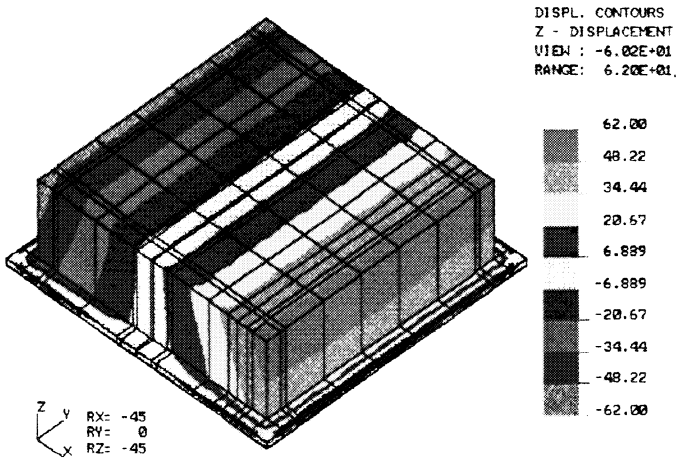

Figure 16: STA00F.EID

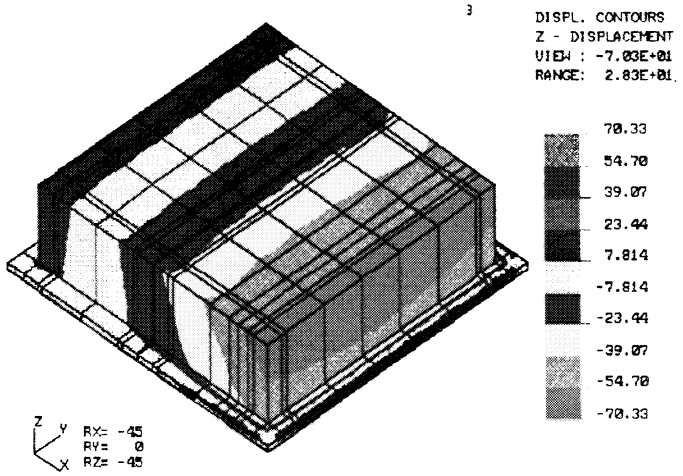

Figure 17: STA80F.EID

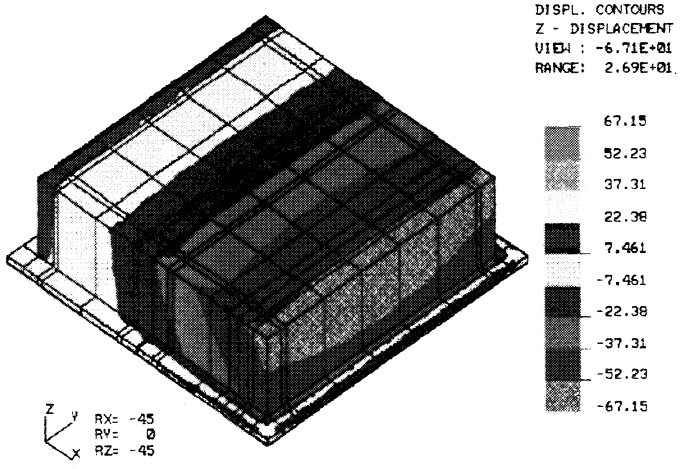

Figure 18: STA60F.EID

Table 4: FEA Results of Tile# 191025-299 with Disbond Along X and Y Axes

Mode Number	Natural Frequencies (Hz)		
	100% Bond	80% Bond (Y-Axis)	80% Bond (X-Axis)
1	480	449	455
2	487	450	469
3	525	505	510
4	$1016^{(RY)}$	$850^{(RY)}$	$873^{(RX)}$
5	$1020^{(P)}$	$969^{(RX)}$	$966^{(RY)}$
6	$1025^{(RX)}$	$1013^{(P)}$	$1020^{(P)}$
7*	1489	1439	1439
8	1898	1865	1860
9	2031	2009	2007
10	2371	2350	2185

Legend

$^{(RY)}$ Rigid Body Rocking of Tile about Y-Axis

$^{(RX)}$ Rigid Body Rocking of Tile about X-Axis

* Modes 7 and Higher are Flexing Modes

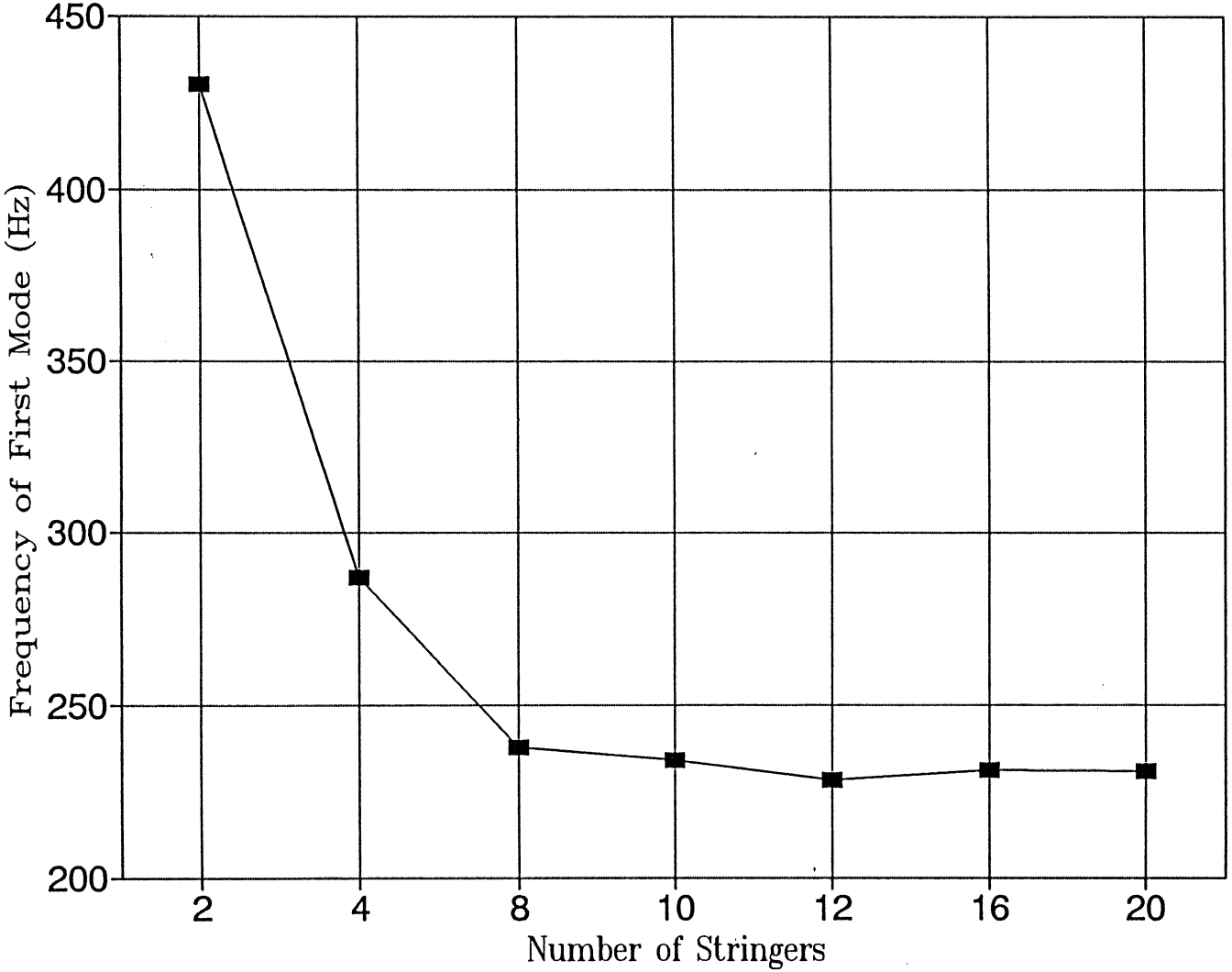

Figure 19: Mid-Fuselage Stringer Sensitivity

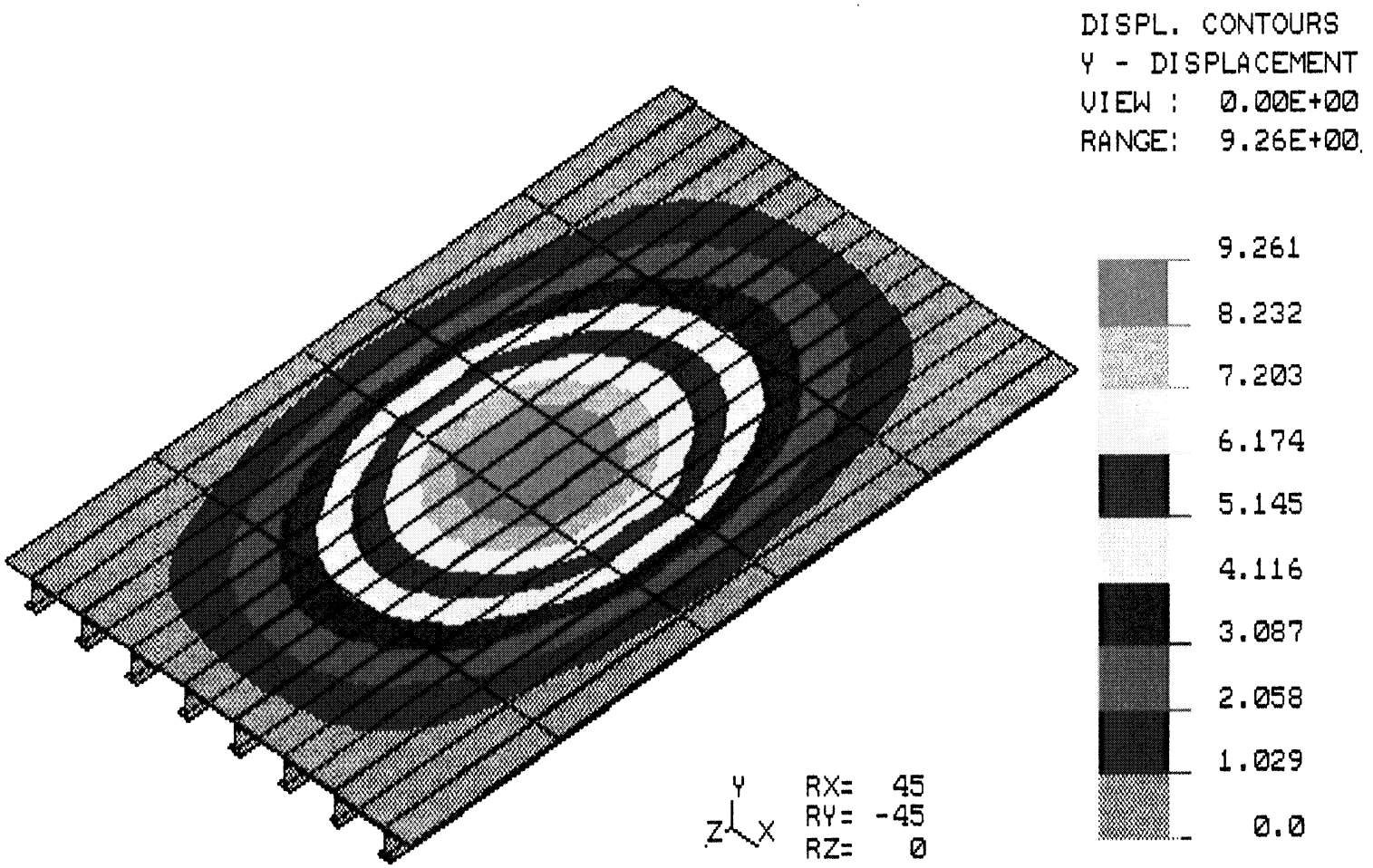

Figure 20: Typical Extended Structure Mode Shape for Sensitivity Analysis (8 Stringers)

took 12.9 hours of CPU time to complete. FEA results are given in Table 5. Figures 22 and 23 illustrate the rocking mode shape of the tile for the extended structure model for the 100% and 80% bond cases, respectively. It was expected that natural frequencies of this model would be lower than those of the single-tile/clamped structure model as a decrease in stiffness of the tile assembly would result due to the introduction of an elastic structure. However, for each out of plane mode of the rigid strucure case, two exist for the flexible strucure, one lower and one higher than the frequency of the rigid case. Due to the structural motion, the lower frequency coresponding to where the structure is in phase with the tile and the higher frequency coresonds to where the structure is 180° out of phase with the tile. Another unexpected result is encountered in the mode shapes of this model. Whereas it has been demonstrated in a clamped structure model that the axis of rotation for the mode of tile rocking about an axis parallel to that of the disbond shifts away from the disbonded area, the axis of rotation shifts towards the disbonded area in this model. This perplexity demonstrates the need for further development of finite element models involving an extended structure, if it is deemed that structure is necessary for the correct dynamic response of a tile.

The next model consideration is the filler bar. As described before, there is a modeling dilemma regarding filler bar because of the non-linear contact between the filler bar and RSI tile. Thus, models of different configurations were analyzed with and without filler bar. Adding or subtracting filler bar to a model changed the overall model size and CPU run time minimally. The single-tile/clamped structure model of Table 3 was modeled without filler bar (see Figure 24 for mesh) with results appearing in Table 6. Mode shape plots for 100%, 80%, and 60% bond cases are shown in Figures 25, 26, and 27, respectively.

The single-tile/extended structure model of Table 5 was modeled without filler bar (see Figure 28 for mesh) with results appearing in Table 7. Mode shape plots for 100% and 80% bond cases are shown in Figures 29 and 30, respectively.

One last physical variable to be addressed was whether or not a multiple-tile model is required to properly simulate the vibration characteristics of a single tile. The determination for the need of multiple tiles to be modeled rests heavily on whether or not the filler bar is determined to transmit vibration, given the complexity of the filler bar-to-tile contact. If, indeed, the filler bar is concluded to play a significant role in the vibration of the tile assembly, then a multiple-tile model is required. If, however, the filler bar is deemed as an insignificant vibration transmitter, then it must be determined whether or not the mass of theadditional tiles is critical for correct vibration characteristics. Consequently, a model was developed which consisted of the typical single-tile on extended structure model with point masses added to represent additional tiles. The mesh of this model is identical to that of Figure 21. Model size and run time varied minimally from the typical single-tile on extended structure model. Results of FEA of this model are given in Table 8.

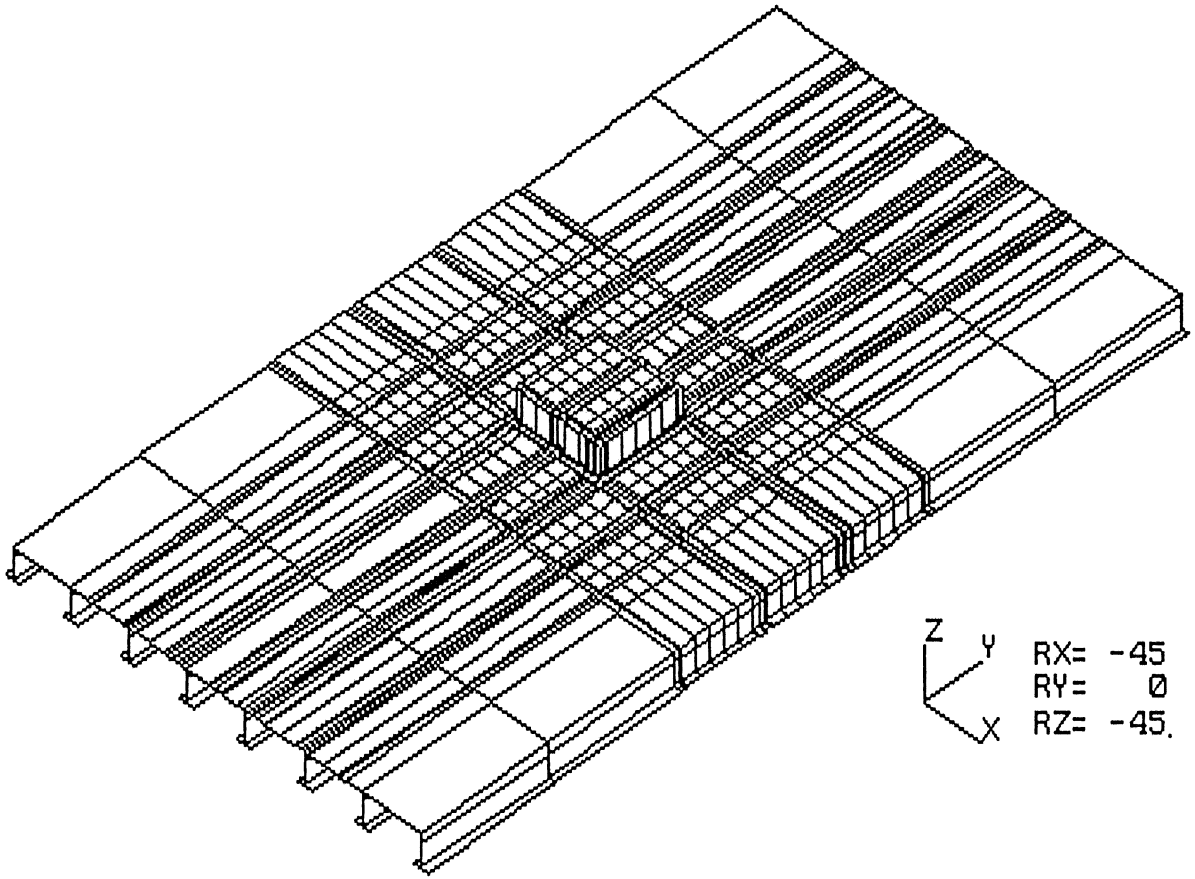

Figure 21: STA00P.EII

Table 5: FEA Results of Tile# 191025-299 With Extended Structure

Mode Shape	100% Bond		80% Bond		60% Bond	
	Mode#	Frequency (Hz)	Mode#	Frequency (Hz)	Mode#	Frequency (Hz)
TX	22	391	22	384	23	371
TY	23	444	23	406	20	360
ROT	24	480	25	458	25	448
P	45	802	42	735	41	670
RX	56	894	52	853	47	806
RY	65	1029	61	940	48	813
ST	1-21	189-366	1-21	189-366	1-19	189-355
	25-44	480-774	24	457	21-22	366-366
	46-55	803-893	26-41	487-717	24	435
	57-64	896-1021	43-51	738-850	26-40	487-652
			53-60	858-920	42-46	717-802

Legend

TX: Rigid Body Translation of Tile in X-Axis Direction
TY: Rigid Body Translation of Tile in Y-Axis Direction
ROT: Rigid Body Rotation of Tile about Z-Axis
P: Rigid Body Translation of Tile in Z-Axis Direction (Piston Mode)
RX: Rigid Body Rocking of Tile about X-Axis
RY: Rigid Body Rocking of Tile about Y-Axis
ST: Mid-Fuselage Structural Modes

Table 6: FEA Results of Tile# 191025-299 Without Filler Bar at Percentage Bond

Mode #	Natural Frequencies (Hz)			Mode Shape Description
	100% Bond	80% Bond	60% Bond	
1	352	284	214	ROT
2	379	319	235	TX
3	380	359	338	TY
4	737	552	407	RY
5	740	660	572	RX
6	847	808	783	P
7	1264	1208	1191	F
8	1760	1726	1706	F
9	1924	1901	870	F
10	2248	2228	2218	F

Legend

TX: Rigid Body Translation of Tile in X-Axis Direction
TY: Rigid Body Translation of Tile in Y-Axis Direction
ROT: Rigid Body Rotation of Tile about Z-Axis
RX: Rigid Body Rocking of Tile about X-Axis
RY: Rigid Body Rocking of Tile about Y-Axis
P: Rigid Body Translation of Tile in Z-Axis Direction (Piston Mode)
F: Flexing of Tile

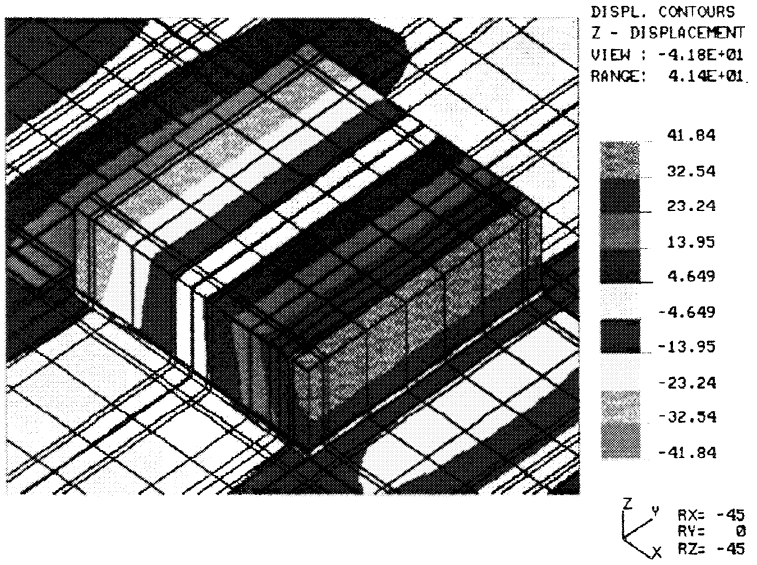

Figure 22: STA00P.EID

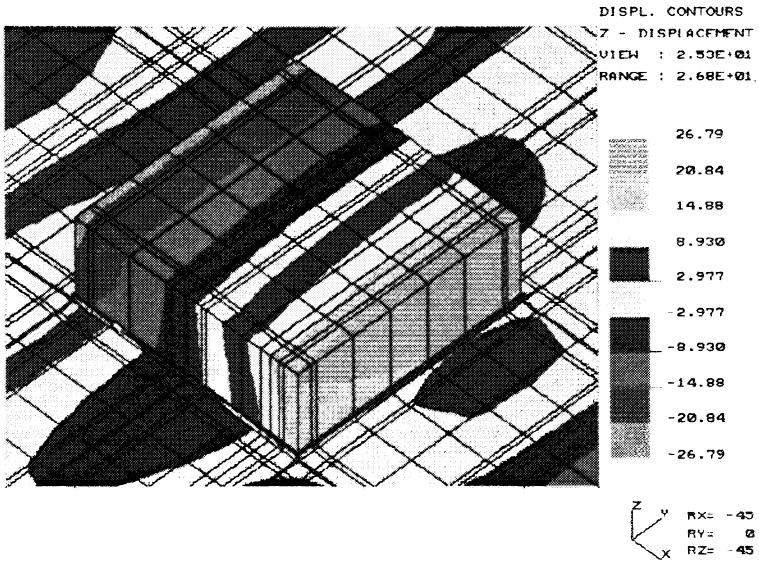

Figure 23: STA80P.EID

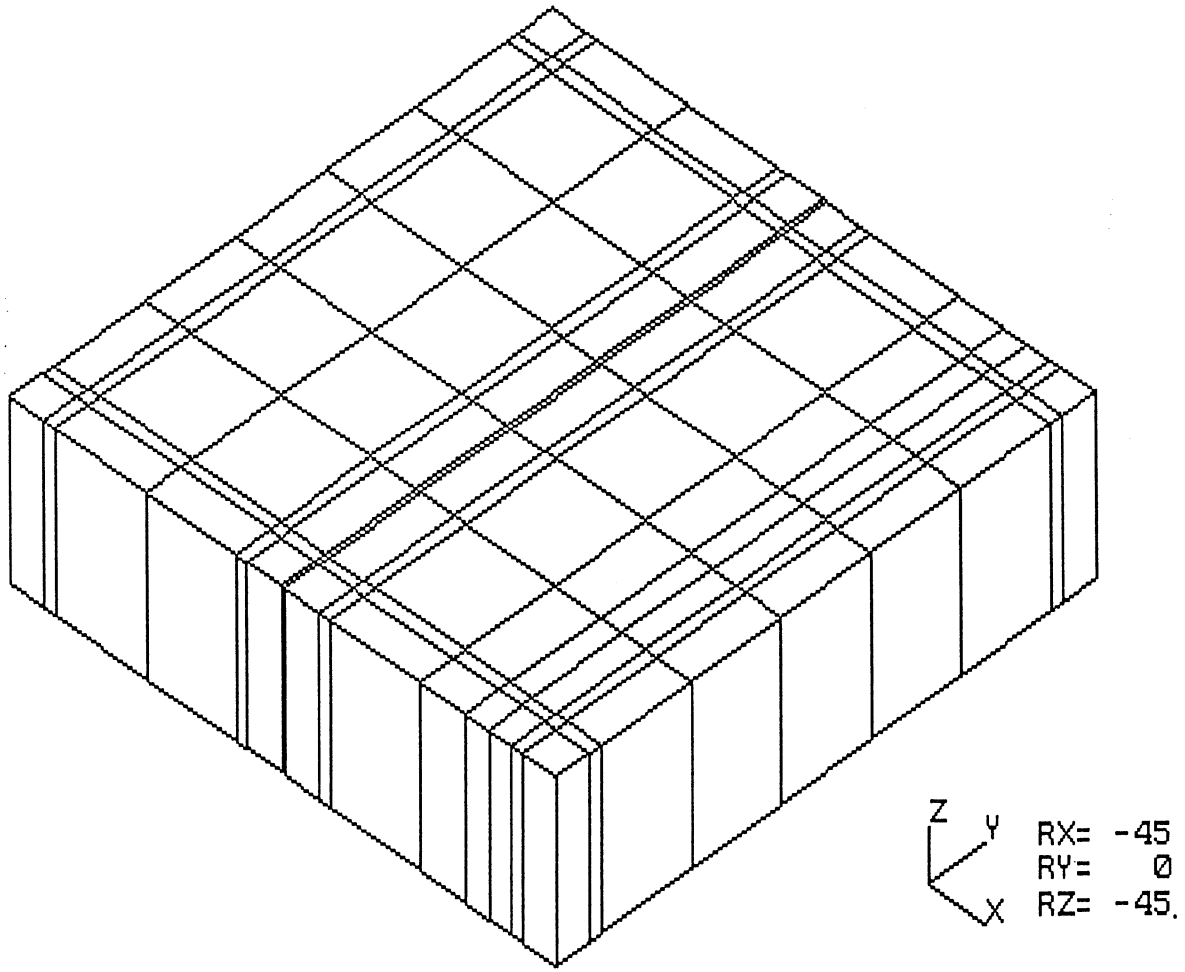

Figure 24: STA00N.EII

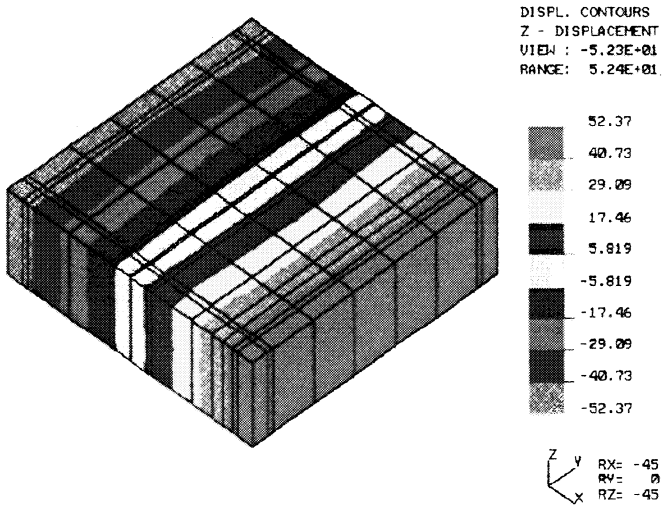

Figure 25: STA00N.EID

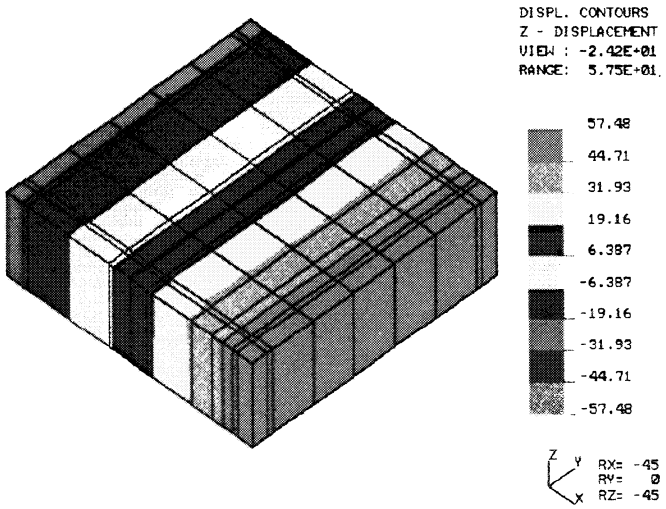

Figure 26: STA80N.EID

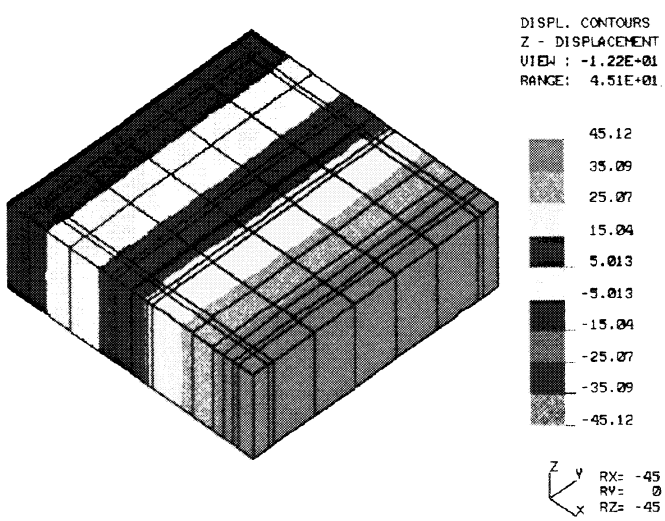

Figure 27: STA60N.EID

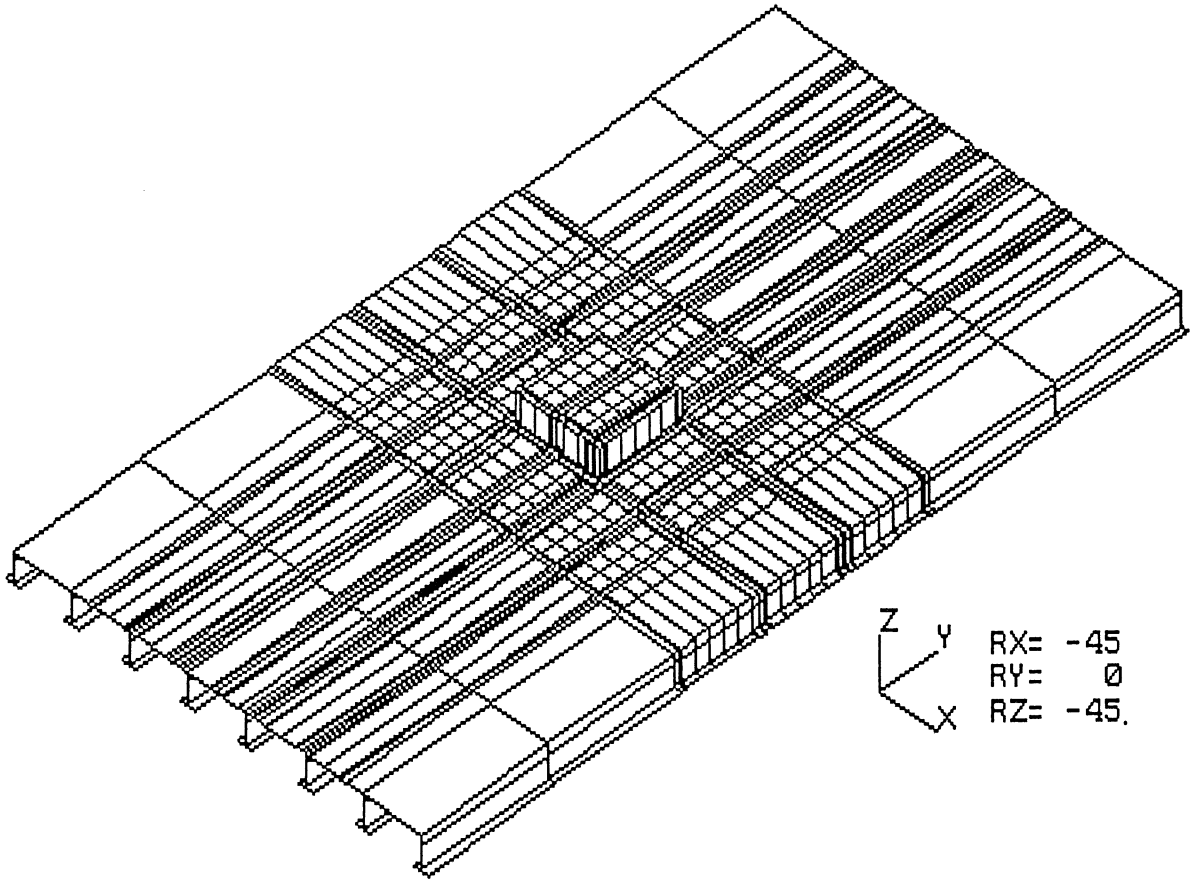

Figure 28: STA00Q.EII

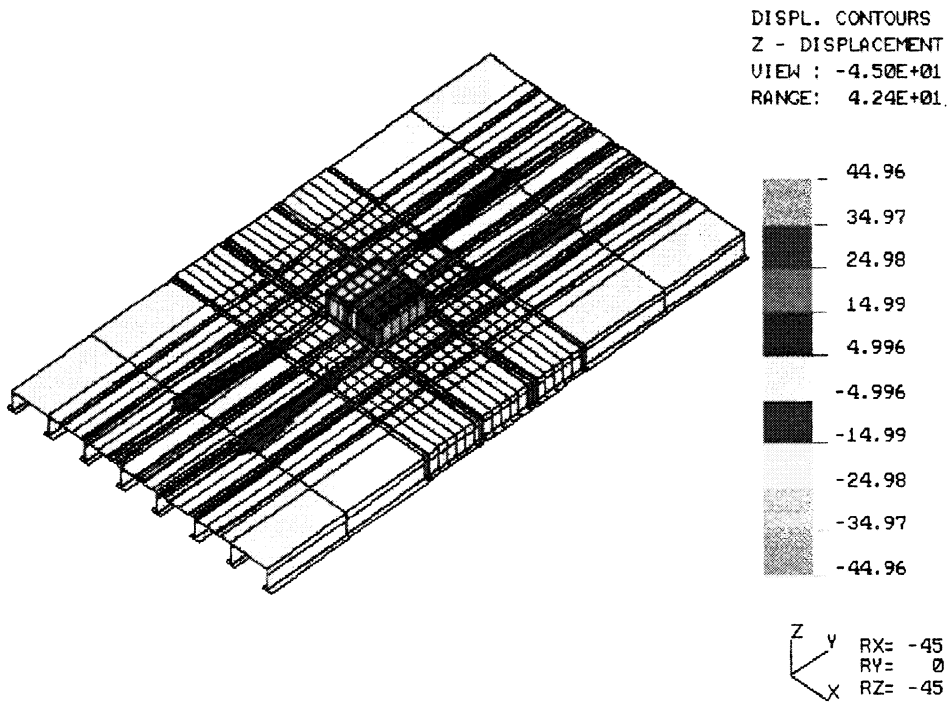

Figure 29: STA00Q.EID

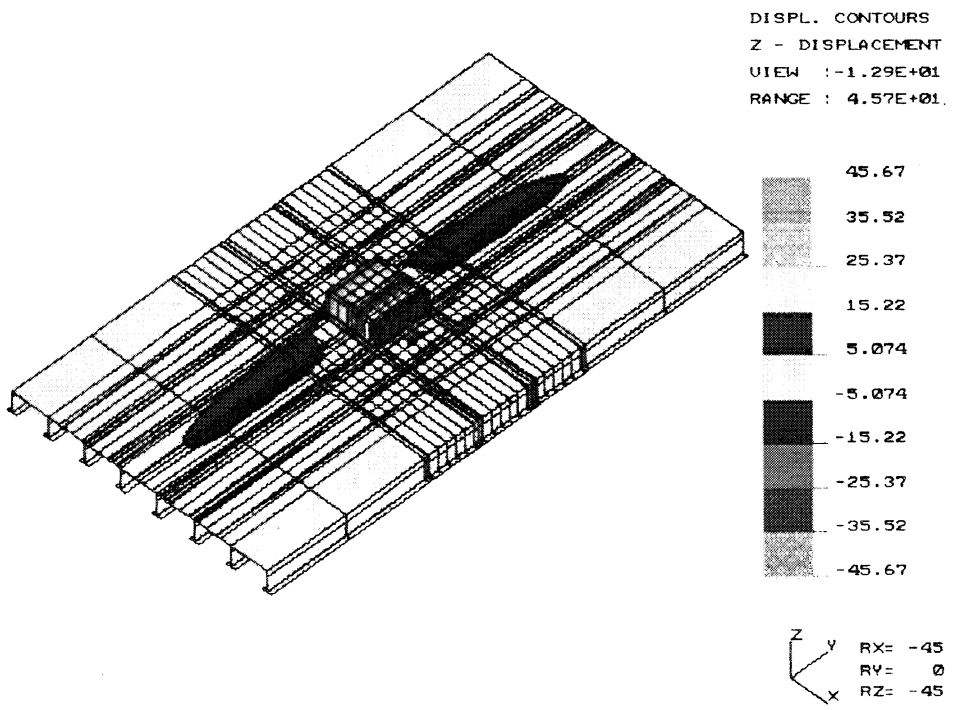

Figure 30: STA80Q.EID

Table 7: FEA Results of Tile# 191025-299/Extended Structure Without Filler Bar

Mode Shape	100% Bond		80% Bond	
	Mode#	Frequency (Hz)	Mode#	Frequency (Hz)
ROT	19	351	8	283
TY	24	368	19	348
TX	25	441	25	427
RX	41	688	40	611
P	42	713	41	611
RY	45	756	44	728
ST	1-18 20-23 26-40 43-44 46-68	189-350 354-366 485-649 717-740 760-1090	1-7 9-18 20-24 26-39 42-43 45-68	187-256 295-342 350-366 479-597 656-716 739-1014

Legend

TX: Rigid Body Translation of Tile in X-Axis Direction
TY: Rigid Body Translation of Tile in Y-Axis Direction
ROT: Rigid Body Rotation of Tile about Z-Axis
P: Rigid Body Translation of Tile in Z-Axis Direction (Piston Mode)
RX: Rigid Body Rocking of Tile about X-Axis
RY: Rigid Body Rocking of Tile about Y-Axis
ST: Mid-Fuselage Structural Modes

Table 8: FEA Results of Tile# 191025-299/Extended Structure with Point Masses

Mode Shape	100% Bond	
	Mode#	Frequency (Hz)
TX	22	391
TY	23	444
ROT	24	480
P	45	801
RX	60	896
RY	68	1029
ST	1-21 25-44 46-59 61-67	189-366 480-773 803-894 905-1021

Legend

TX: Rigid Body Translation of Tile in X-Axis Direction
TY: Rigid Body Translation of Tile in Y-Axis Direction

ROT: Rigid Body Rotation of Tile about Z-Axis
P: Rigid Body Translation of Tile in Z-Axis Direction (Piston Mode)
RX: Rigid Body Rocking of Tile about X-Axis
RY: Rigid Body Rocking of Tile about Y-Axis
ST: Mid-Fuselage Structural Modes

A 10-tile model with filler bar was analyzed with a clamped structure assumption to validate its feasibility as an analytically correct model. The 100% bond case model has 20580 DOF and 4368 elements (see Figure 9 for mesh), requiring 13.9 hrs. of CPU time. FEA results for the 100% bond case are given in Table 9. Tables 10 and 11 give the results for the 80% and 60% bond cases, respectively. It is noted that closely spaced modes in these tables demonstrate the fact that the 10 tiles of the model are alike. A clearer understanding of vibration behavior is achieved through investigation of mode shapes. Figures 31 and 32 are representative examples. The rocking mode about the axis of disbond is illustrated for 80% and 60% bond cases, respectively, in these figures.

The final finite element consideration was the simulation of the acoustical energy to be applied during experimental testing. Thus, a forced response analysis of a single-tile was performed with a dynamic pressure corresponding to 100 dB applied to the top surface of the tile of interest. The equivalent pressure was calculated to be 290×10^{-6} psi. Resonant frequencies calculated through a forcedresponse analysis are listed in Table 12 for a single tile on clamped structure and a single tile on extended structure. A typical response spectrum graph for various nodes on the top surface (see Figure 33) of a multi-tile/clamped structure model is illustrated in Figure 34. In this particular figure, it is noted that the center point of each tile except the tile of interest has a single out-of-plane mode corresponding to the piston mode of the tile.

However, the tile of interest has a disbond of 40% in this case. Consequently, the axis of rotation for the corresponding rocking mode is shifted, and the center point is no longer on this axis of zero motion. This is demonstrated in the second, earlier mode of the center point of the tile of interest corresponding to the rocking mode of the tile about an axis parallel to the disbond. The presence of two peaks on a frequency response plot (out-of-plane motion) is a clear indicator of a tile which has disbond. Also, from these frequency response spectrum graphs, the amplitude of displacement of any particular point on the tile can be found. For the 100 dB signal, the computed maximum displacement of the center point on a tile on clamped structure is 23×10^{-6} in. for 100% bond. This is important to realize, as the displacement the tile experiences must be at least as great as the sensitivity of any instrument intended to measure its displacement. This particular displacement is acceptable for all measurement techniques discussed. However, the tile of interest has a disbond of 40% in this case. Consequently, the axis of rotation for the corresponding rocking mode is shifted, and the center point is no longer on this axis of zero motion.

Table 9: FEA Results of 10-Tile Model/Clamped Structure, 100% Bond

Mode Number	Frequency (Hz)	Mode Number	Frequency (Hz)	Mode Number	Frequency (Hz)
1	474	21	568	41	1025
2	477	22	581	42	1028
3	481	23	585	43	1028
4	487	24	599	44	1029
5	490	25	612	45	1029
6	496	26	616	46	1030
7	501	27	626	47	1034
8	510	28	632	48	1034
9	512	29	647	49	1034
10	527	30	648	50	1037
11	529	31	1014	51	1038
12	535	32	1015	52	1040
13	539	33	1019	53	1040
14	541	34	1020	54	1046
15	549	35(RY)	1021	55	1047
16	550	36	1023	56	1047
17	551	37	1023	57	1047
18	552	38(P)	1024	58	1052
19	558	39	1024	59	1052
20	559	40	1025	60	1056

Legend

(RY) Rigid Body Rocking of Tile of Interest about Y-Axis

(P) Rigid Body Translation of Tile of Interest in Z-Axis Direction (Piston Mode)

Table 10: FEA Results of 10-Tile Model/Clamped Structure, 80% Bond

Mode Number	Frequency (Hz)	Mode Number	Frequency (Hz)	Mode Number	Frequency (Hz)
1	467	21	562	41	1025
2	471	22	581	42	1025
3	481	23	585	43	1027
4	486	24	599	44	1029
5	486	25	604	45	1030
6	495	26	615	46	1031
7	499	27	625	47	1034
8	510	28	631	48	1034
9	512	29	636	49	1036
10	523	30	647	50	1038
11	525	31(RY)	847	51	1039
12	535	32(P)	993	52	1040
13	539	33	1013	53	1043
14	540	34	1016	54	1046
15	547	35	1019	55	1051
16	550	36	1020	56	1052
17	550	37	1021	57	1057
18	551	38	1023	58	1066
19	552	39	1024	59	1068
20	557	40	1024	60	1077

Legend

(RY) Rigid Body Rocking of Tile of Interest about Y-Axis

(P) Rigid Body Translation of Tile of Interest in Z-Axis Direction (Piston Mode)

Table 11: FEA Results of 10-Tile Model/Clamped Structure, 60% Bond

Mode Number	Frequency (Hz)	Mode Number	Frequency (Hz)	Mode Number	Frequency (Hz)
1	446	21	560	41	1020
2	460	22	581	42	1020
3	481	23	581	43	1021
4	483	24	582	44	1023
5	486	25	583	45	1023
6	494	26	585	46	1024
7	496	27	596	47	1024
8	510	28	598	48	1025
9	511	29	614	49	1025
10	517	30	622	50	1026
11	523	31	628	51	1029
12	535	32	633	52	1030
13	538	33	647	53	1030
14	540	34(RY)	719	54	1033
15	545	35(P)	928	55	1034
16	549	36	1002	56	1036
17	549	37	1015	57	1037
18	551	38	1016	58	1038
19	551	39	1017	59	1040
20	552	40	1019	60	1041

Legend

(RY) Rigid Body Rocking of Tile of Interest about Y-Axis

(P) Rigid Body Translation of Tile of Interest in Z-Axis Direction (Piston Mode)

Table 12: FE Forced Response Fundamental Frequencies for Tile# 191025-299

		100% Bond	80% Bond	60% Bond
Clamped Structure	With Filler Bar	1019 Hz	850 Hz	728 Hz
	Without Filler Bar	847 Hz	552 Hz	235 Hz
Extended Structure	With Filler Bar	802 Hz	753 Hz	670 Hz

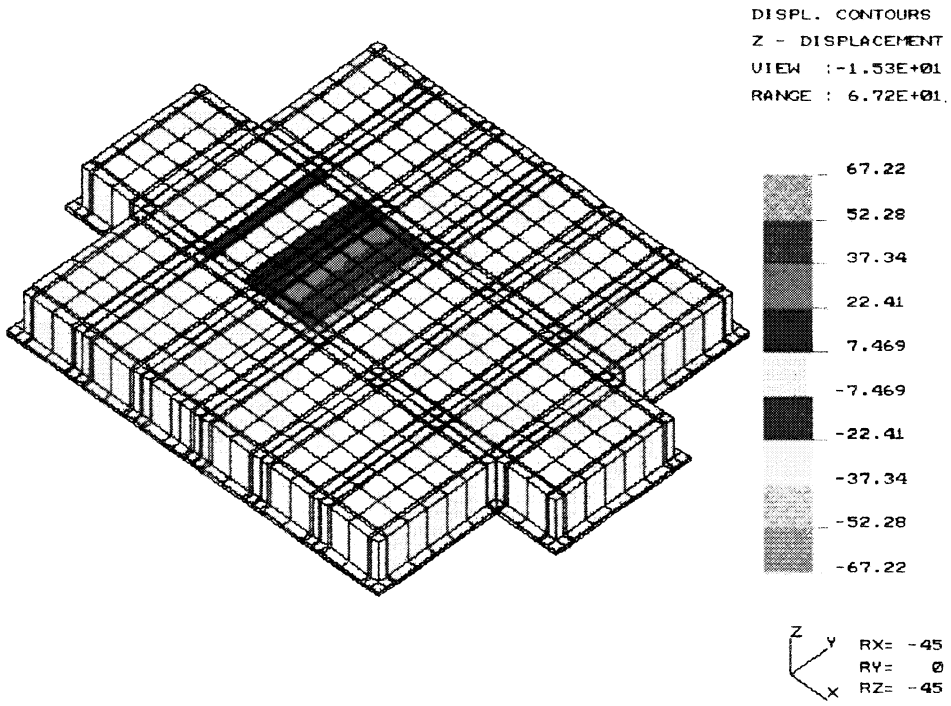

Figure 31: MT380F.EID

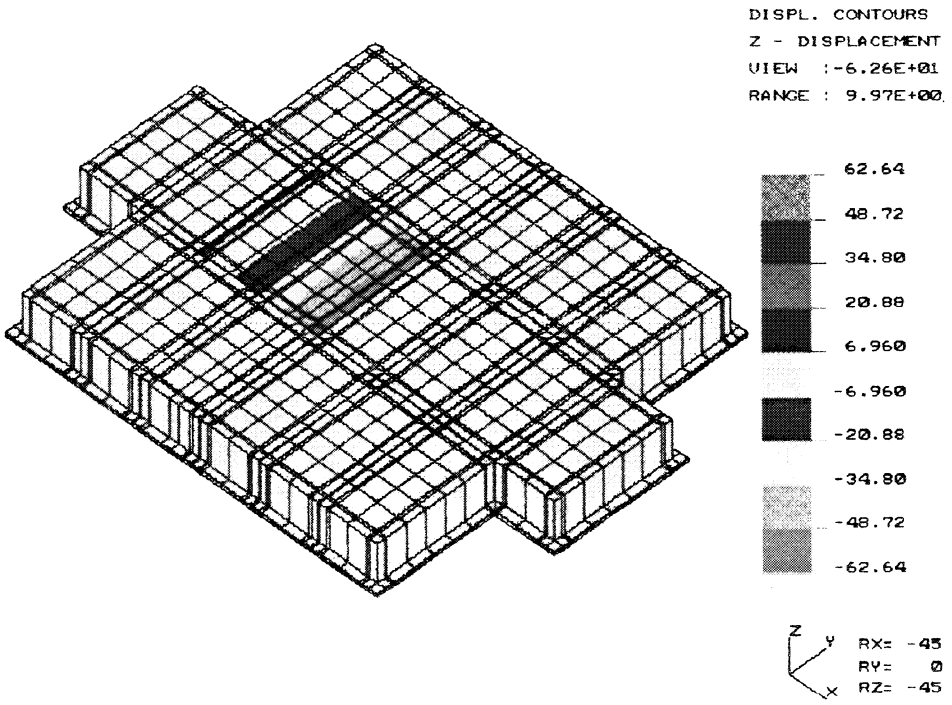

Figure 32: MT360F.EID

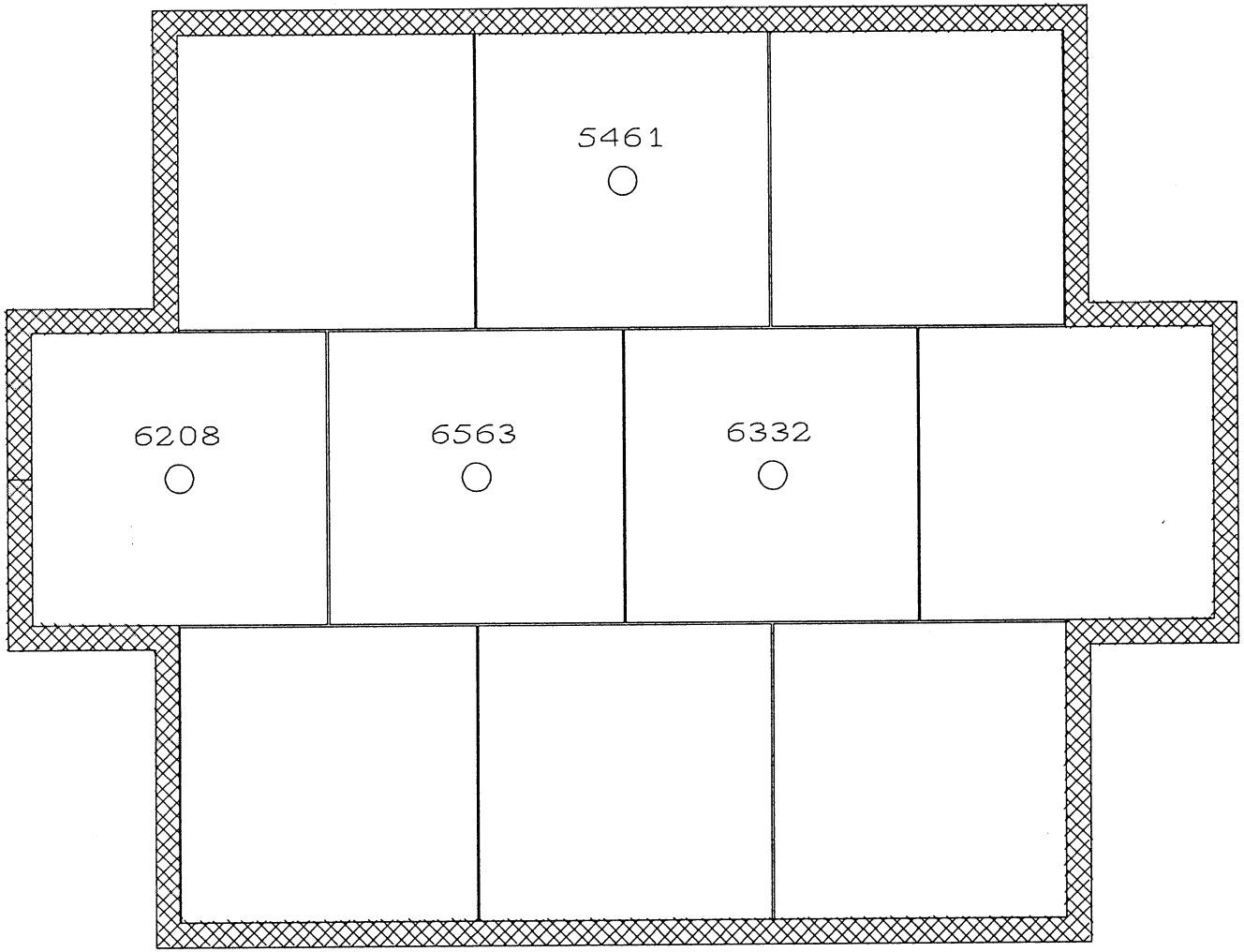

Figure 33: Nodes of Multi-Tile/Clamped Structure Model Analyzed in Frequency Response Calculations

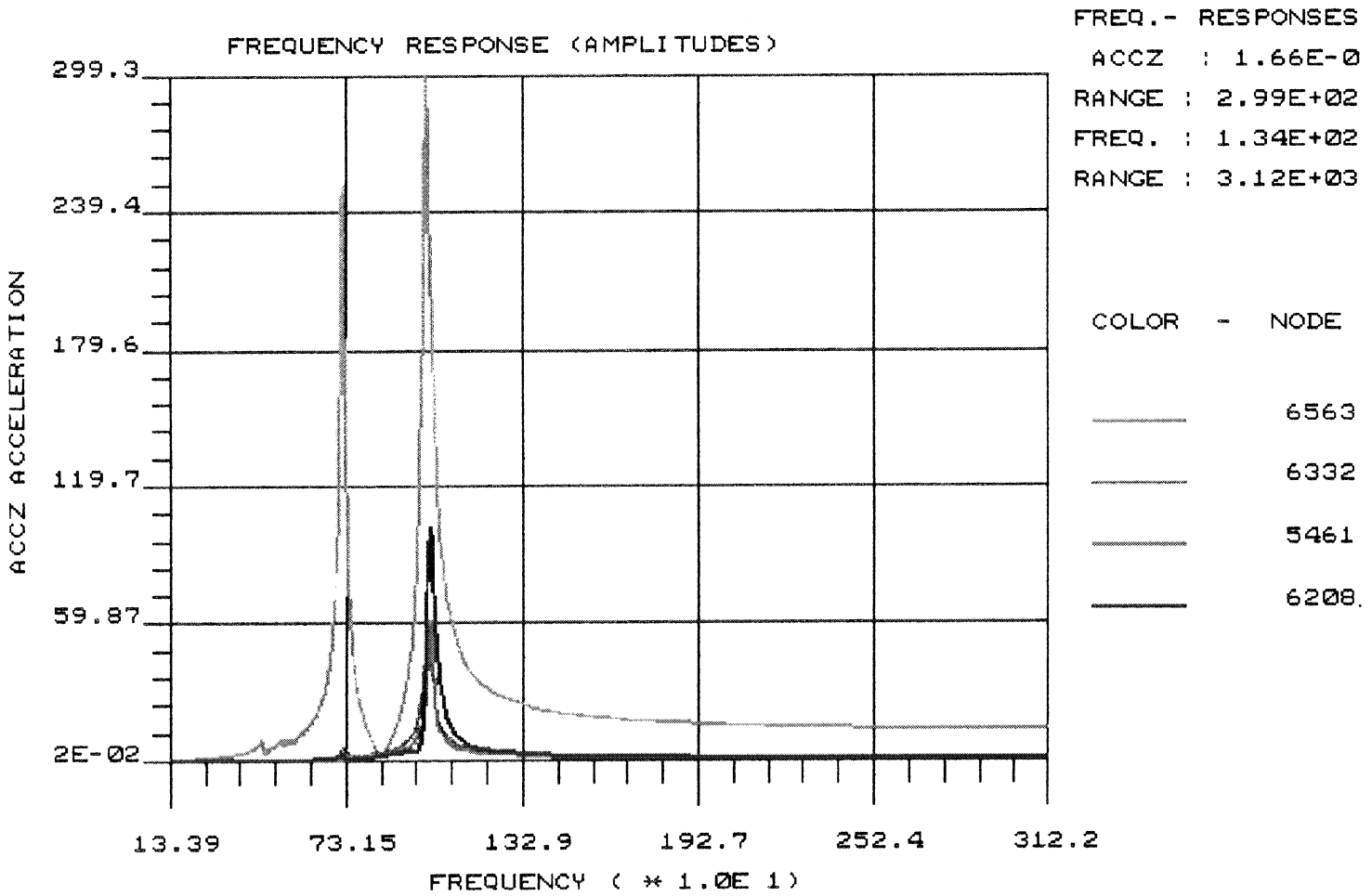

Figure 34: Typical Frequency Response Spectrum Graph of 10-Tile/Clamped Structure Model

7 EXPERIMENTAL RESULTS

EMA and frequency sweep analysis of a 2.4 inch tile was performed at UCF for comparison to finite element results of a FE model of this tile. Results of all testing is listed in Table 13. The first three frequencies measured using EMA which are of modes which produce out-of-plane acceleration, compare well with FEA results of the first three modes which produce out-of-plane acceleration. Frequency response results correlate well with FEA results also, noting the first three out-of-plane modes. Considering the FEA results to be exact, the experimental results would indicate the tested tile to be approximately 90% bonded.

EMA of the UCF 2.4 inch TPS tile was performed once more with and without filler bar to determine its affect on vibration characteristics. Natural frequencies for both cases are listed in Table 14. The trend of natural frequencies rising with the introduction of filler bar indicates that filler bar is an essential part of the TPS tile assembly vibration system and must be included in all analytical analyses. EMA was performed at UCF on five sample tiles of varying properties which were provided by NASA. The testing of these tiles served only as a demonstration of EMA as a viable vibration measurement technique for Space Shuttle TPS tiles. Results of testing are listed in Table 15.

Holography testing successfully identified several TPS tile natural frequencies and mode shapes, demonstrating its capability as a non-contact technique to measure modal parameters. Figures 35 and 36 show, respectively, the experimental set-up and representative holograms of a 2.4 inch tile mode shape at resonance.

Shearography results were ambiguous. The videotape recording of the test revealed no patterns at all, indicating no surface strain and, hence, no indication of bond problems. Unfortunately, the result of no pattern does not indicate conclusively that the results are meaningful. However, post-testing removal of the tiles did indicate all tiles tested were nominally bonded. Also, the test suggested that shearography is capable of wide-scale high-speed modal pattern imaging of OV tiles[18].

The Ometron VPI measurements, however, did return good results, as seen in Table 16. These results correlated well with FEA results. Not only were natural frequencies measured, but for tile# 191025-299, mode shapes were constructed allowing the direct comparison with FE results. Figure 37 is an example of an Ometron VPI measured mode shape. This particular mode shape is the rocking mode about the y-axis. Comparison of the frequency of this mode to that attained with FEA suggests that this tile has a bond between 90% and 100%, assuming the FEA results are exact. Even considering error in the FEA results, it is encouraging that the LDV determined results of a tile on an actual Space Shuttle correlate well with FEA results.

Table 13: EMA, Frequency Sweep, and FEA Results of 2.4 inch UCF TPS Tile

Mode Number	FEA Natural Frequencies (Hz)			Experimental Frequencies (Hz)	
	100% Bond	90% Bond	80% Bond	EMA	Freq. Sweep
1	279	257	226	-	-
2	292	271	243	-	-
3	293	285	278	-	-
4(RY)	597	536	461	398	526
5(RX)	599	572	540	570	574
6(P)	683	663	652	674	667
7(F)	1325	1303	1285	-	1774
8	2115	2094	2049	-	1826
9	2255	2234	2138	-	1927
10	2547	2269	2152	-	-
11	2577	2291	2159	-	-
12	2899	2317	2172	-	-
13	2974	2373	2189	-	-
14	3081	2453	2219	-	-
15	3103	2494	2261	-	-
16	3226	2516	2272	-	-
17	3433	2560	2282	-	-
18	3440	2569	2351	-	-
19	3473	2573	2392	-	-
20	3478	2633	2556	-	-

Legend

(P) Piston Mode

(RX) Rocking of Tile about X-Axis

(RY) Rocking of Tile about Y-Axis

(F) Modes 7 and Higher are Flexing

- Not Measured

Table 14: EMA Results of 2.4 inch Tile With and Without Filler Bar

Mode Number	Frequency (Hz)	
	With Filler Bar	Without Filler Bar
1	446	398
2	482	478
3	554	514
4	590	566
5(P)	642	586

Legend

(P) Piston Mode

Table 15: EMA Results of Five Sample TPS Tiles at UCF

Sample		Natural Frequencies (Hz)					
		Mode 1	Mode 2	Mode 3	Mode 4	Mode 5	Mode 6
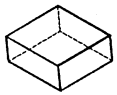	1	474	522	570	642°	-	-
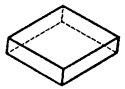	2	428	476	566°	624	-	-
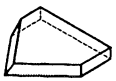	3	316	340	368	396°	524	-
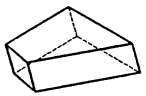	4	296	380	448	528°	-	-
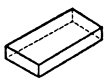	5	260	336	428	476	548°	624

Legend
- Not measured
° Piston Mode

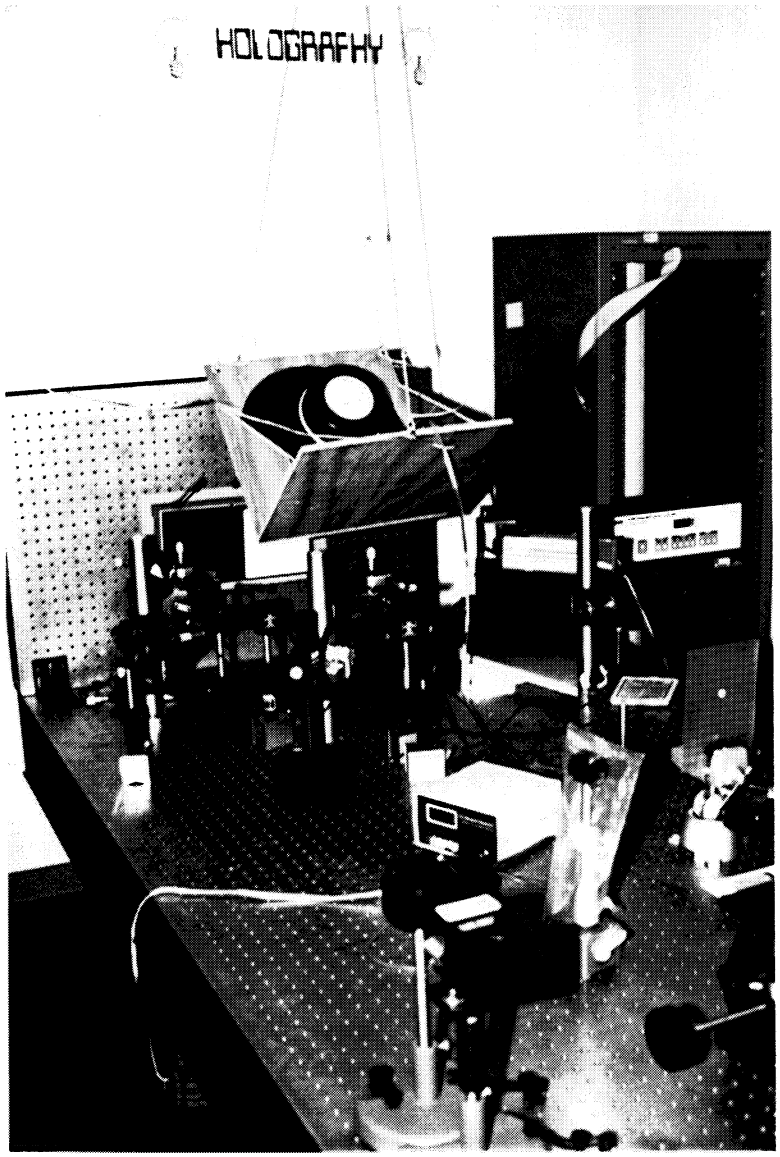

Figure 35: Holography Set-up

Figure 36: Mode Shape Holograms of UCF 2.4 inch Tile at Resonance

Table 16: Ometron VPI Results from Rockwell International-Palmdale

Mode Number	FEA Natural Frequencies (Hz)			Ometron VPI Test Natural Frequencies (Hz)
	100% Bond	90% Bond	80% Bond	
1	480	467	449	
2	487	472	450	
3	525	513	505	
4(R)	1015	934	850	978
5	1020	1000	969	
6	1025	1017	1013	
7(F)	1489	1461	1439	
8	1898	1878	1865	1887
9	2031	2021	2009	
10	2371	2358	2351	2334
11	2396	2376	-	
12	2929	2921	-	
13	3016	3010	-	
14	3037	3029	-	
15	3078	3064	-	
16	3115	3095	-	
17	3157	3142	-	3166
18	3263	3251	-	
19	3295	3288	-	
20	3596	3586	-	3572

Legend
- Not Calculated
(R) Rocking of Tile about Disbond Axis
(F) Modes 7 and Higher are Flexing Modes

MODE #1, 978.41 Hz, 1.65% Cr
(DEFORMED-SOLID LINE, UNDEFORMED-DASHED LINE)

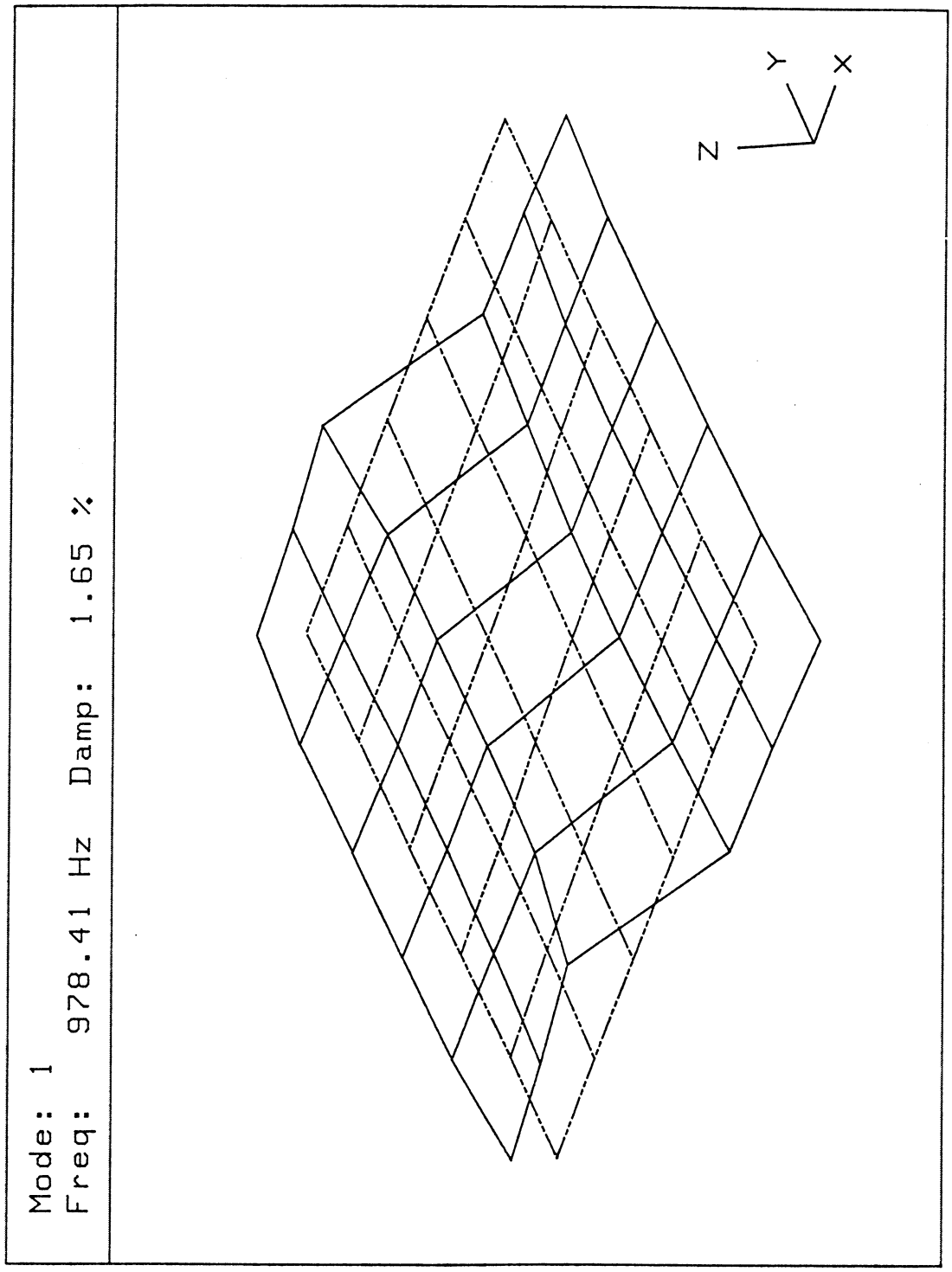

Figure 37: Ometron VPI Measured Mode Shape of Tile #191025-299

8 CONCLUSIONS AND RECOMMENDATIONS

A non-contact, non-destructive technique has been devised for which Space Shuttle TPS tiles may be evaluated for bond condition. The most practical course to take in implementing a successful TPS tile evaluation program begins with establishing a database of nominal natural frequencies for the most suspect tiles. This can be accomplished through the use of finite element calculations coupled with continuous verification of natural frequencies during the installation process. Once a database is successfully established, comparison of experimental evaluation would quickly identify the bond condition of a particular TPS tile.

Various considerations as described in this final report need to be addressed before implementation of a reliable system is to be born, especially perplexities in finite element modeling. Forced response FEA and EMA results arrived at in this research attest that filler bar is a significant component of the vibration system and must be considered in any analytical modeling. However, forced response results indicate that tile interaction appears to be minimal, thus eliminating the requirement for a 10-tile finite element model. Also, FEA results indicate that the mass of surrounding tiles does not affect vibration characteristics of an extended structure model, hence, this mass need not be modeled in FE analyses. Forced response analyses indicate that some natural frequencies of a tile on extended structure vary with those of a tile on a clamped structure. Thus, structure below a TPS tile must be modeled in order to obtain the correct dynamic response to acoustic energy, which is presumed to be the exciting force.

REFERENCES

1. Korb, L.J., and Clancy, H.M., "Shuttle Orbiter Thermal Protection System: A Material and Structural Overview," paper No. STS 81-0219 presented at the 26th National Symposium Society for the Advancement of Materials and Process Engineering, April 1981.

2. Goldstein, H.E., Leiser, D.B., and Katvala, V.W., "Reaction Cured Glass and Glass Coatings," U.S. Pat. 4,093,771, June 1978.

3. FRCI-12: Fibrous Refractory Composite Insulation Material, Another Product of Space-Age Technology, Lockheed Missiles & Space Company, Inc., January 1987.

4. LI-900: Lockheed's All-Silica Insulation Material, A Product of Space-Age Technology, Lockheed Missiles & Space Company, Inc., January 1987.

5. LI-2200: A 22-PCF, All-Silica Insulation Material, Another Product of Space-Age Technology, Lockheed Missiles & Space Company, Inc., January 1987.

6. Materials Properties Manual Volume 3: Thermal Protection System Materials Data, Rockwell International, August 1988.

7. Gericke, O.R., "Ultrasonic Spectroscopy," in Research Techniques in Nondestructive Testing, Sharpe, R.S., Ed., Academic Press, New York, pp. 31-62, 1970.

8. Halmshaw, R., "Direct-View Radiological Systems," in Research Techniques in Nondestructive Testing, Sharpe, R.S., Ed., Academic Press, New York, pp. 241-268, 1970.

9. Lawson, W.D., and Sabey J.H., "Infrared Techniques," in Research Techniques in Nondestructive Testing, Sharpe, R.S., Ed., Academic Press, New York, pp. 443-477, 1970.

10. Stubbs, N.S., and Osegueda, R.A., "Global Damage Detection in Solids -Experimental Verification," International Journal of Analytical and Experimental Modal Analysis, Volume 5, Number 2, pp. 81-97, April 1990.

11. Springer, W.T., Lawrence, K.L., and Lawley, T.J., "Damage Assessment Based on the Structural Frequency-Response Function," Experimental Mechanics, Volume 28, pp. 34-37, March 1988.

12. Hearn, G., and Testa, R.B., "Modal Analysis for Damage Detection in Structures," Journal of Structural Engineering, Volume 117, pp. 3042-3063, October 1991.

13. Chen, J. and Garba, J.A., "On-Orbit Damage Assessment for Large Space Structures," AIAA Journal, Volume 26, Number 9, pp. 1119-1126, September 1988.

14. Rizos, P.F., Aspragathos, N., and Dimarogonas, A.D., "Identification of Crack Location and Magnitude in a Cantilever Beam from the Vibration Modes," Journal of Sound and Vibration, Volume 138, Number 3, pp. 381-388, 1990

15. Moslehy, F.A., Davies, T.W., and Davis, R.M., "Finite Element Modeling and Vibration Measurement Applied to the Space Shuttle TPS Tiles Bond Verification," Proceedings of the 1991 Joint Army-Navy-NASA-Air Force (JANNAF) Nondestructive Evaluation Meeting, KSC, FL, pp. 51-60, May 14-16 1991.

16. Stubbs, N.S., and Osegueda, R.A., "Damage Detection in Periodic Structures," Damage Mechanics and Continuum Modeling, ASCE, New York, pp. 113-128, 1985.

17. ____, "NISA II User's Manual, Version 91.0," Engineering Mechanics Research Corporation, Troy, MI, April 1990.

18. Davis, R.M., Moslehy, F.A., and Clarke, M.M., "Nondestructive Evaluation of Shuttle Columbia Tiles," Proceedings of the 29th Space Congress, pp. 2.1-2.9, April 1992.

MATERIALS PERFORMANCE AND EVALUATION

RESEARCH PROGRAM

END OF YEAR REPORT
1993

Dr. Vimal H. Desai

Materials Science and Engineering Program
Mechanical and Aerospace Engineering Department
College of Engineering
University of Central Florida

REBAR CORROSION PROTECTION BY ELECTRICAL INJECTION OF INHIBITORS

EXECUTIVE SUMMARY

Corrosion of steel reinforcements in concrete structures is a commonly encountered problem. This is especially true for structures which are exposed to the marine environments containing large amounts of chloride ions. Since the relative humidity is high in the coastal environments, chloride ions diffuse through the concrete relatively faster and cause localized corrosion of rebar by enhancing the passive film breakdown. Also, the rebar/concrete interface degradation occurs due to the stresses generated by accumulation of corrosion products. There are several methods used to protect the rebar against corrosion. Among them are, using galvanized rebars (zinc coated), epoxy coated rebars, premixing of corrosion inhibitors in the concrete at the time of mixing, and cathodic protection. All these methods, except for the last one, are applicable only before the structure is fabricated. Corrosion of existing off-shore structures, bridges in the coastal marine environments poses a serious problem. Cathodic protection is often used for this purpose. Expensive instrumentation, continuous monitoring, high installation costs and hydrogen embrittlement (especially in prestressed rabars) are some of the disadvantages of using this technique.

Electrical injection is a novel technique for applying corrosion inhibitors to the existing structures. In this technique complex cationic inhibitors are forced to move to the rebar/concrete interface under the high electric field gradient between the rebar (cathode) and a temporary anode on the top of concrete specimen. The applied electric field ranges from 5-10 V/cm. In our studies a series of quaternary cationic inhibitors, with molybdate and nitrite anionic part, were injected and the inhibitor efficiency was determined by polarization resistance (R_p), corrosion potential (E_{corr}), and polarization studies. The results from the above studies indicate that E_{corr} became more positive with inhibitor injection. Even after removal of electric field the diffusion of the inhibitor continues towards the rebar/concrete interface. Three weeks after the injection time, E_{corr} of the specimen containing 15 lb/yd^3 of NaCl attained a value close to the specimen containing no NaCl. Similarly, the polarization resistance increased continuously. The results from these studies indicate that corrosion protection of the existing structures using electrical injection is practical and efficient. Detailed studies are in progress to optimize the injection parameters like the electric field strength, inhibitor concentration and injection time. A series of inhibitors are being studied to determine the most efficient inhibitor system. The effect of prolonged inhibitor injection (through applied electric field) on the mechanical integrity of concrete (especially, the compressive strength of concrete and interfacial bonding between concrete and rebar) is being investigated. Also, determination of the diffusivity of various inhibitor molecules under varying applied potentials is being investigated.

INTRODUCTION

Corrosion of steel rebars in concrete structures is a commonly encountered problem especially for structures exposed to the marine environments containing large amounts of chloride ions. Since the relative humidity is high in the coastal environments, chloride ions diffuse through the concrete relatively faster and cause localized corrosion of rebar by promoting the breakdown of passivity. Degradation of rebar/concrete interface occurs due to the stresses generated by the accumulation of corrosion products. Some of the protection methods are use of galvanized rebars , epoxy coatings , corrosion inhibitors, and the cathodic protection. All these methods, except for the last, are applicable only before the structure is fabricated. Corrosion protection of existing structures like bridges, off-shore structures in the coastal marine environments poses a severe problem. Cathodic protection is often used for this purpose but expensive instrumentation, continuous monitoring, high installation costs and hydrogen embrittlement are some of the disadvantages of using cathodic protection.

Electrical injection is a novel technique for applying corrosion inhibitors to the existing structures[1]. In this technique complex cationic inhibitors are forced to move to the rebar/concrete interface under the high electric field gradient between the rebar (cathode) and a temporary anode on the top of concrete specimen.

OBJECTIVES

1. Study the feasibility of applying corrosion inhibitors to existing reinforced concrete structures using electrical fields.

2. Determine the efficiency of electrically injected inhibitors. This is being done using electrochemical methods such as EIS and polarization studies.

3. Determine the optimum parameters for inhibitor application like inhibitor type, concentration, electric field strength, frequency of inhibitor application and current density during inhibitor application.

4. Study the effect of applied electric fields on the integrity of the reinforced concrete and concrete/rebar interfacial strength.

Specimens consisted of cylindrical concrete slabs 4" x 6" and rectangular slabs with steel rebar embedded in them. The specimens also contained dimensionally stable titanium rods used as internal reference electrodes. The potential of these Ti reference electrodes was periodically monitored against an external true reference electrode to compensate for any deviation in their potential from the original established value. A sponge soaked with inhibitor solution (concentration 10mM-100mM) and $Ca(OH)_2$ was placed at the top of the specimen. A mesh of dimensionally stable titanium served as the temporary anode and the rebar was made the cathode. An electric field of strength 5-10 V/cm was applied between them. This high field potential caused the cationic part of the inhibitor to move rapidly towards the rebar forming a film which passivated the surface and protected the surface of the rebar against localized corrosion.

Figures 1(a) and 1(b) shows a schematic experimental setup for inhibitor injection in rectangular and cylindrical concrete slabs. Since the reference electrode is embedded in the concrete specimens, the value of E_{corr} and other parameters is close to the true value because the error due to the IR drop is minimized. Apart from E_{corr} measurement, polarization resistance(R_p), impedance and polarization studies was performed to determine the effectiveness of the inhibitor. An external counter-electrode wrapped around the concrete specimen was used for impedance and polarization studies. Table I lists the specification of specimens used for inhibitor injection.

Table 1 Specimens for specifications used in inhibitor injection

Four Batches With Different NaCl Concentration

10.0 lb/yd^3 or 0.28 wt% NaCl 6.5 g NaCl per Sample
15.0 lb/yd^3 or 0.42 wt% NaCl 9.8 g NaCl per Sample
20.0 lb/yd^3 or 0.56 wt% NaCl 13 g NaCl per Sample

Amount of NaCl	No. of Specimens	E_{corr} (mV) vs Ti *
00.00	6	-16.0 to -31.0
10.0 lb/yd^3	6	-305 to -367
15.0 lb/yd^3	6	-380 to -420
20.0 lb/yd^3	6	-450 to -510

* E_{Ti} vs. SCE = -45 to -60 mV

METHODOLOGY

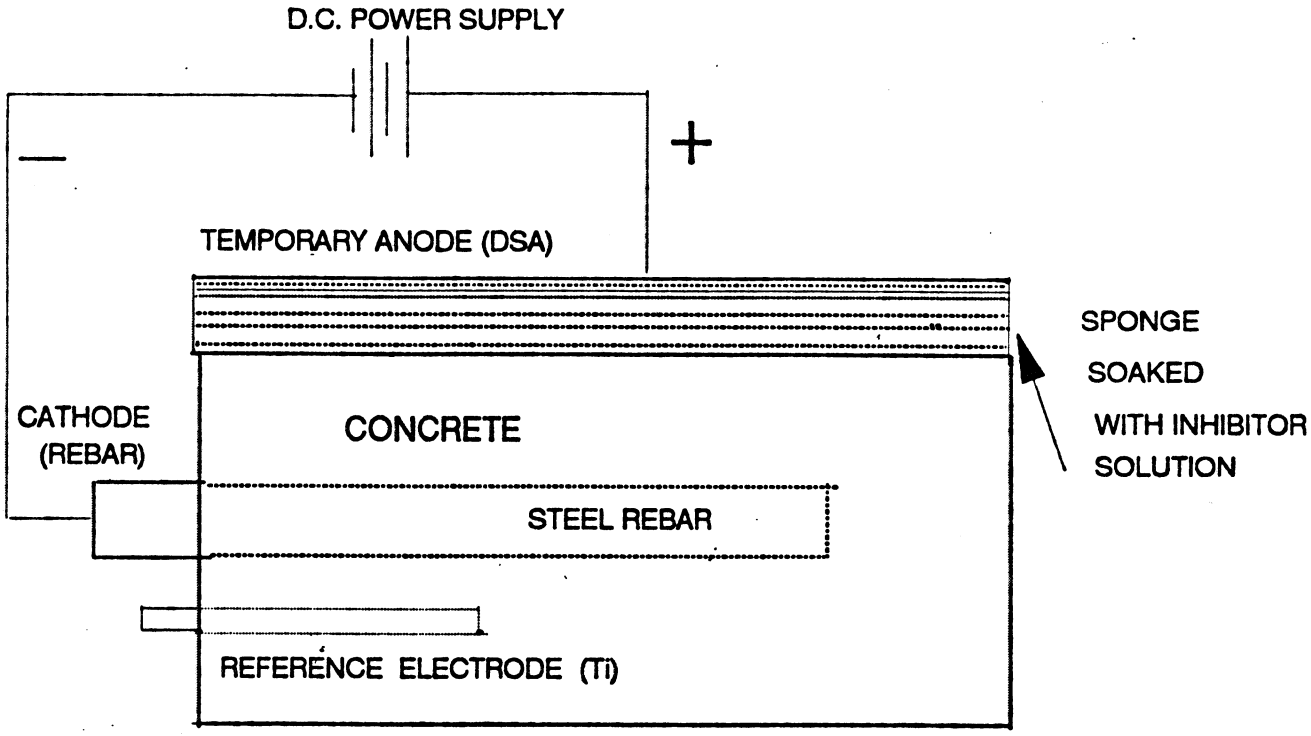

(a)

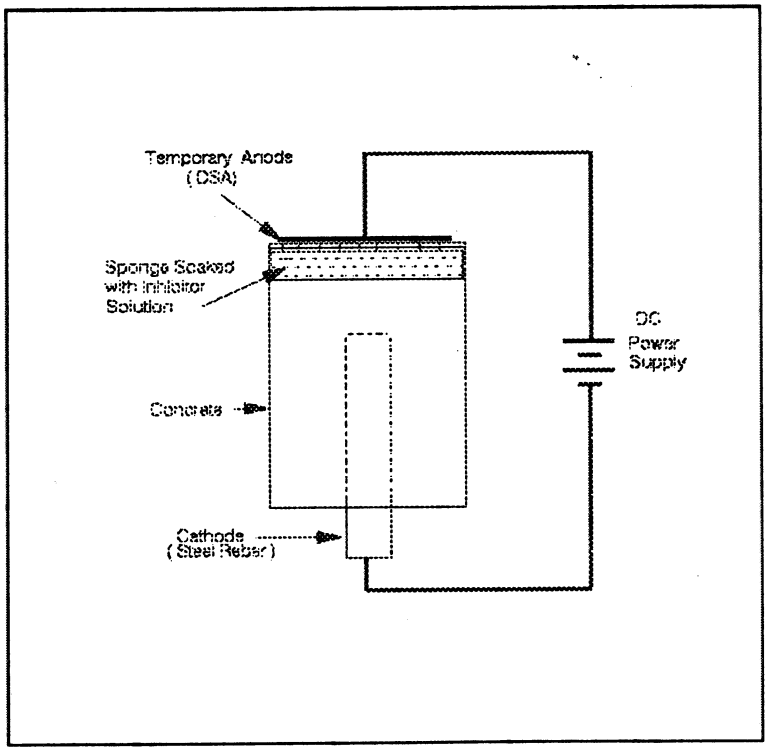

(b)

Figure 1 showing experimental set-up for electrical inhibitor injection.

RESULTS

Inhibitor Screening

studies were performed on polished steel rebars and rebars embedded in concrete. The Polished rebar were immersed in 3.5% NaCl solution (non-derated). The studies were performed in the presence and absence of 10 mM solution of tetrabutylammonium nitrite. Variation of corrosion potential with time (Figure 2) shows that the initial and steady state value of E_{corr} is about 250 mV more noble in the case of electrolyte containing inhibitor solution. Potential dynamic polarization curve (Figure 3) and impedance (bode) plots further confirm the substantial improvement in electrochemical behavior using the above inhibitor. Inhibitors showing substantial improvement were selected for further studies.

Studies on Reinforced Concrete Specimens

The inhibitor was applied to rebar containing concrete specimens using applied electrical field of 5.0 V/cm. Surface treated Ti mesh was used as an Dimensionally Stable Anode (DSA). Inhibitor solution was soaked in a sponge and placed on the top of concrete block and the electric field applied between DSA and rebar as the cathode. The inhibitor cation was driven towards the rebar/concrete interface. Electric field was applied continuously for a period of one week. Periodic monitoring of corrosion potential of specimens containing 10, 15 and 20 lb/yd^3 NaCl with and without inhibitor injection showed that while the specimen without inhibitor injection reached a steady state value of E_{corr} at -305 to -510 mV vs. Ti (E_{Ti} vs. SCE= - 45 mV) the specimen with inhibitor injection show initial rapid drop in Ecorr which became very noble and continue to shift in the noble direction for several weeks after the removal of applied electric field (Table II). The steady state values of Ecorr in these specimens is attained in about 3 weeks after stopping the electrical injection. This value of steady state potential is very close to that for concrete specimens containing no NaCl (-16 to -31 mV). These preliminary results indicate the electrical inhibitor injection substantially improved corrosion behavior. This value of steady state potential persists even 16 weeks after single electrical injection (Figure 4). Potentiodynamic polarization and a.c. impedance studies further indicate improvement in corrosion behavior of electrically injected with inhibitor as shown in figures 5-7.

Experimental Results

Table II indicates the values of Corrosion Potential of steel rebar in three batches of concrete specimens containing different NaCl concentrations. The inhibitor (tetrabutylammonium nitrite at concentration of 10 mM) was applied for one week using electric field of about 5.0 V/cm.

Table II E_{corr} vs Time for Different NaCl Concentration

Specimen batch No.	NaCl (lb/yd^3)	E_{corr} initial (mV)vs. Ti	E_{corr} after one week	E_{corr} after 3 weeks	E_{corr} after 5 weeks	E_{corr} after 15 weeks
1	10	-307	N/A	-50	-44	-43
2	15	-381	-180	-97	-82	-97
3	20	-438	-350	-190	-167	-143

Double Layer Effects

Cathodic polarization studies performed on some of the specimens show no significant effect on scan rate indicating that polarization studies are not representative of any significant double layer effect but are representative of charge transfer at rebar/electrolyte interface. All the above results indicate a remarkable improvement in corrosion rate of embedded rebars after electrical inhibitor application.

Chloride Migration Effects

Initial studies on the effect of electrical fields of 5.0 V/cm on specimens with no inhibitor applied, show that there is no measurable effect of chloride ion migration from near the rebar/concrete interface. This indicates that the improvement in the corrosion resistance of the embedded rebar is predominantly due to inhibition effect of electrically applied inhibitor. Furthermore, AASHTO T277-89 standard also does not predict any significant chloride ion migrations at such low applied voltages.

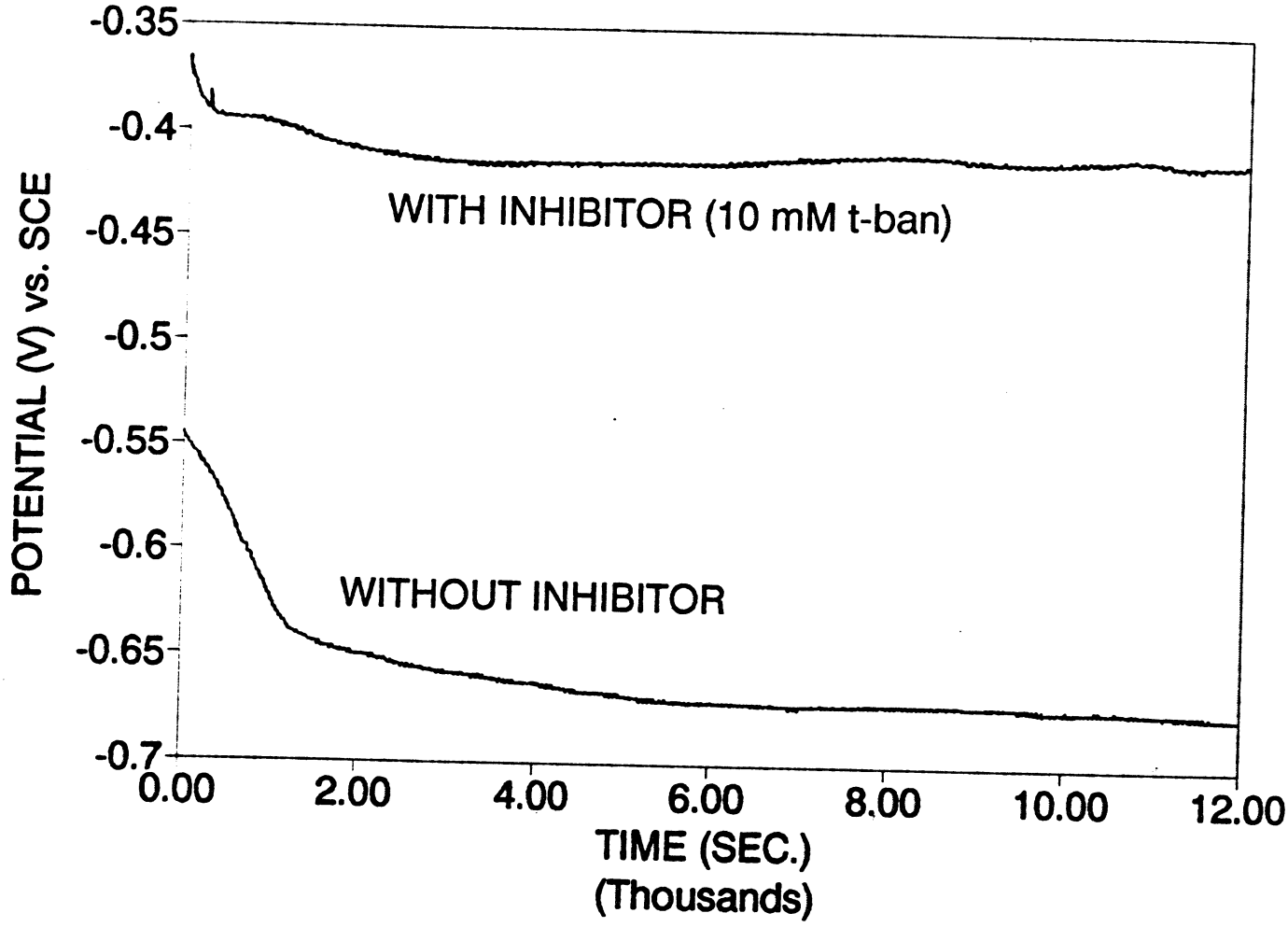

Figure 2 Showing that corrosion potential of polished rebar is about 250 mv more positive when 10mM tetrabutylammonium nitrite is added to 3.5%NaCl solution

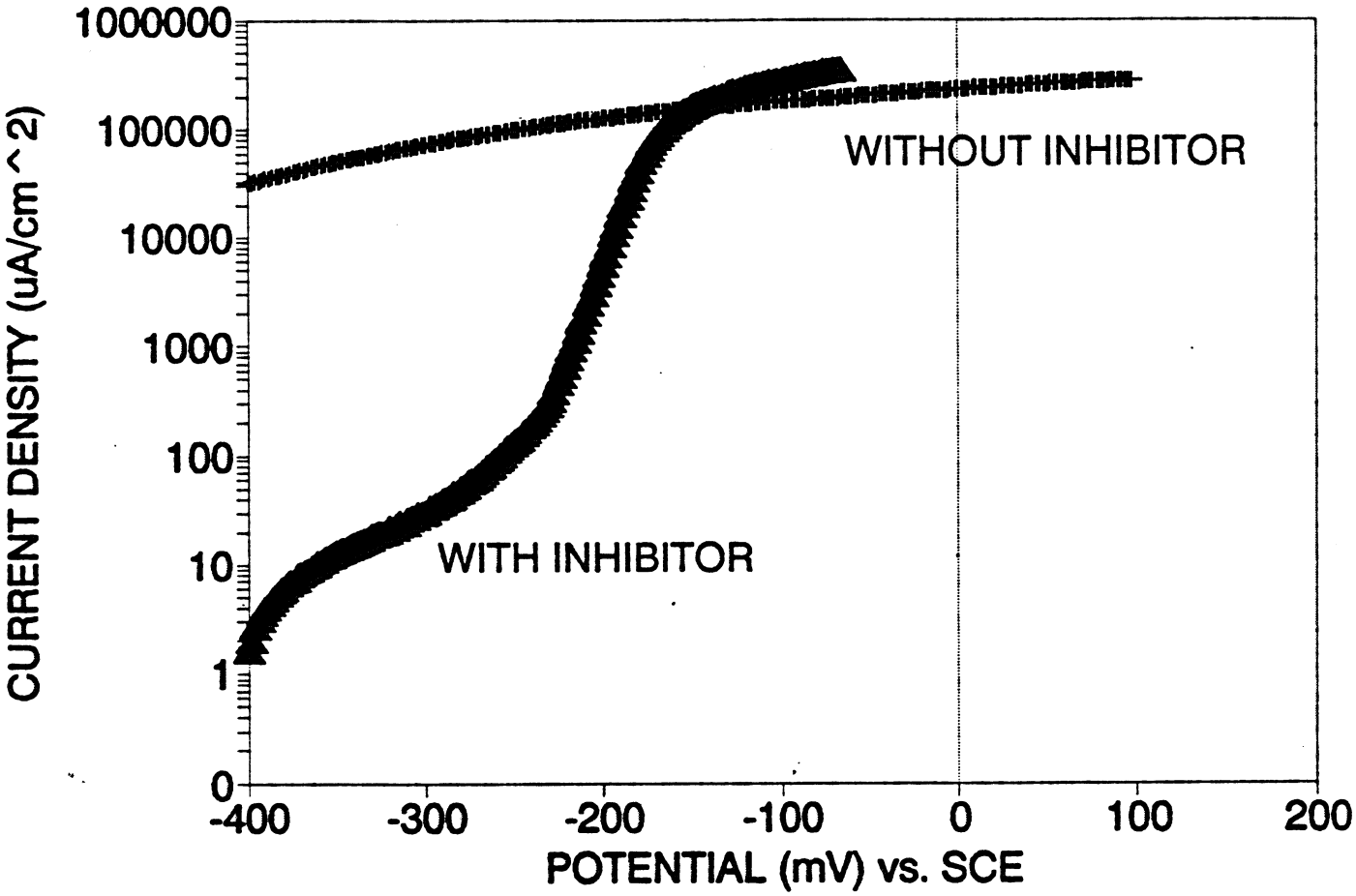

Figure 3 Shows that at all the applied potential the current density of polished rebar specimens is much lesser in the presence of 10mM tetrabutylammonium nitrite in 3.5%NaCl solution as compared to that without inhibitor

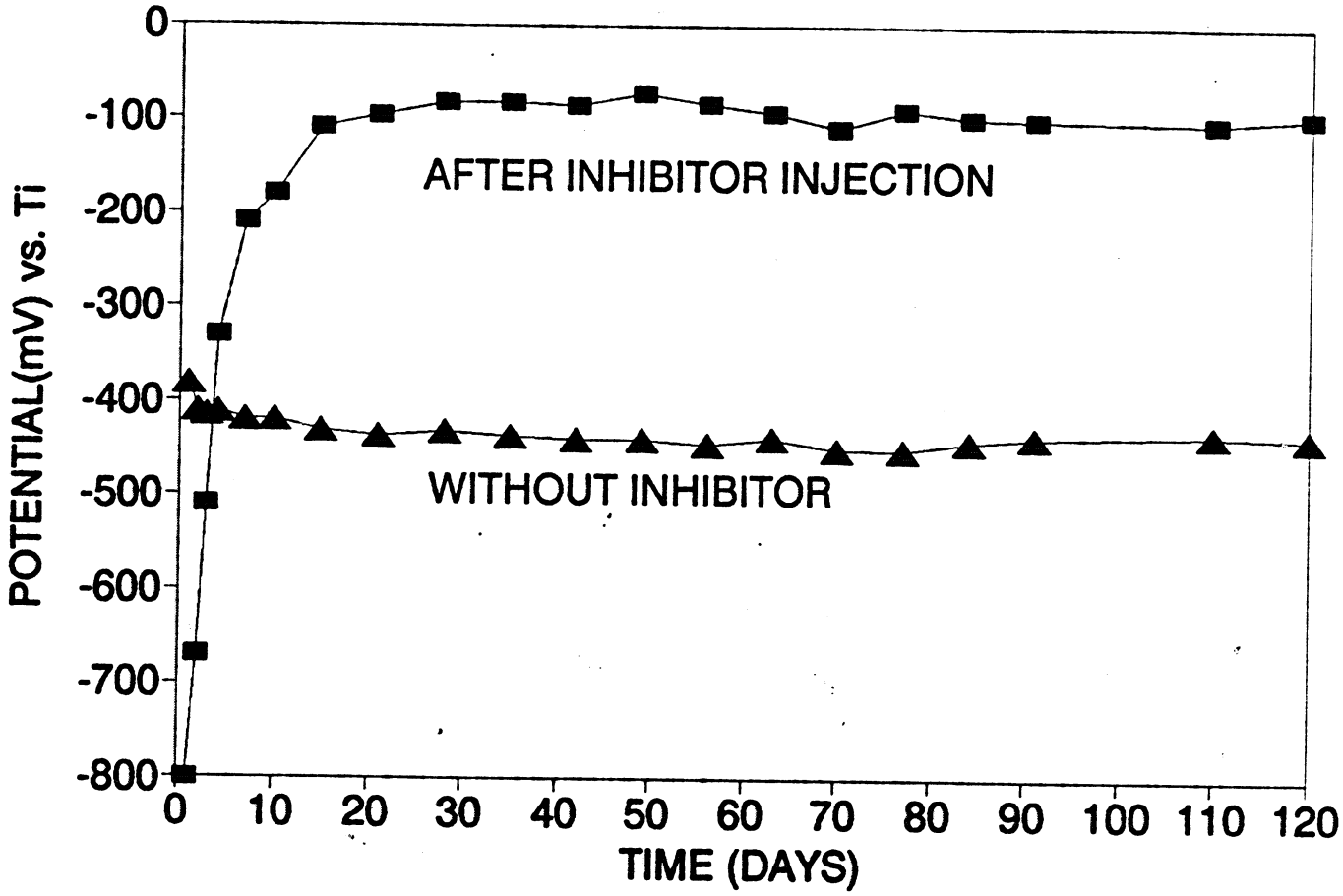

Figure 4 showing that corrosion potential of concrete specimens containing 15 lb/yd^3 became about 300mV more positive after electrical injection of inhibitor (tetrabutylammonium nitrite) for one week

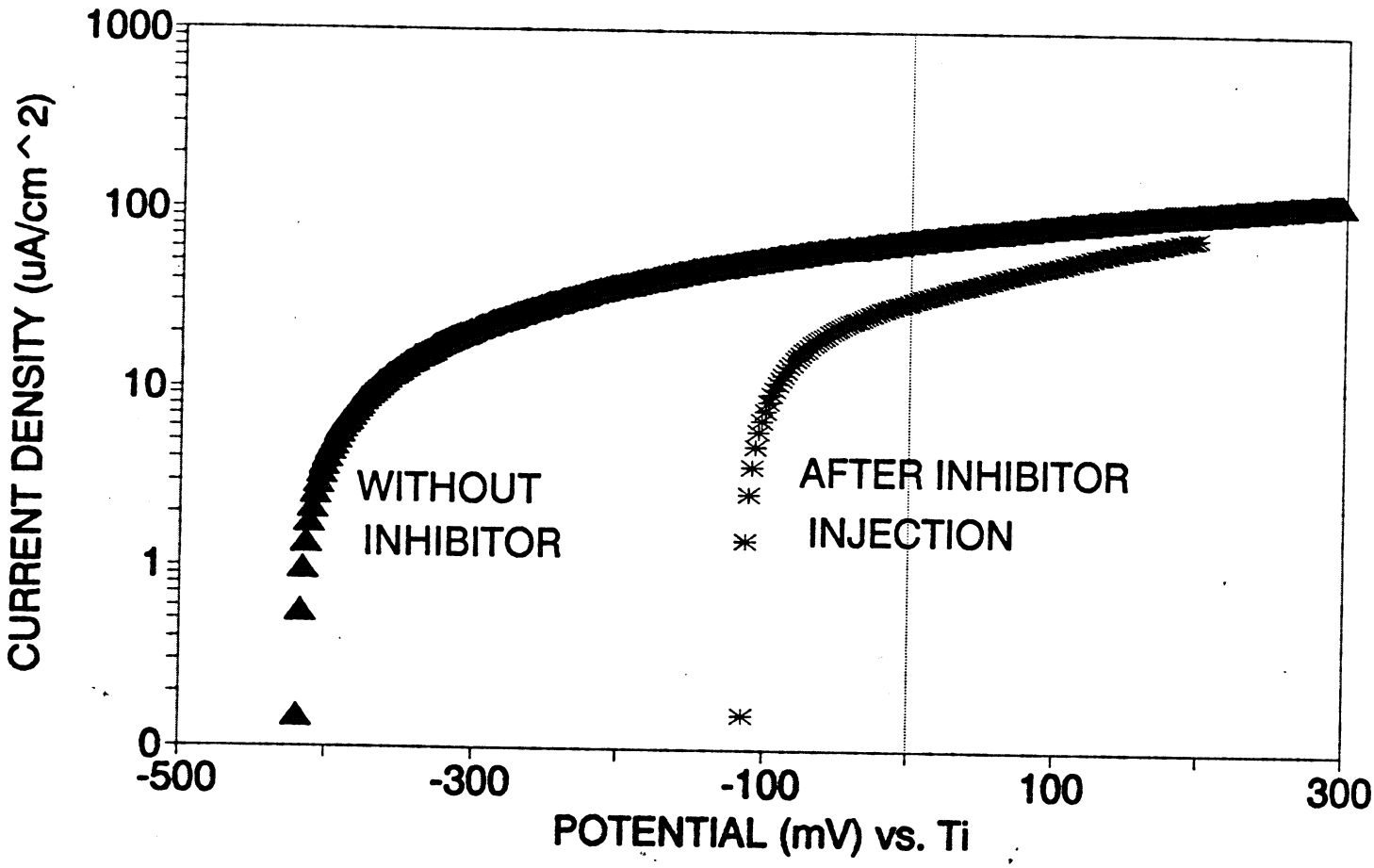

Figure 5 Potentiodynamic polarization curves showing that current density for concrete specimens containing 15 lb/yd^{3}NaCl after electrical injection of tetrabutylammonium nitrite for one week is much lower than that without any inhibitor addition

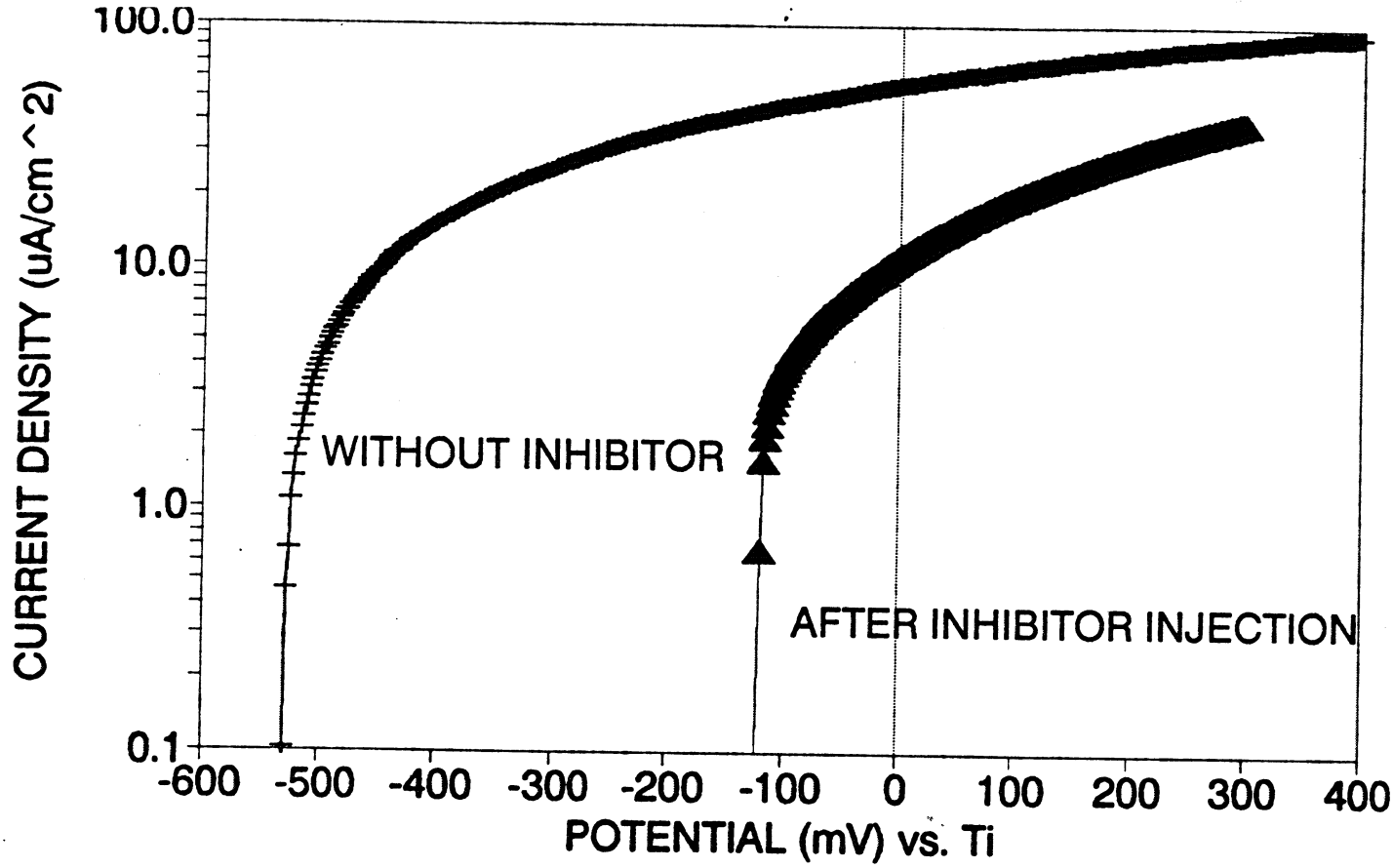

Figure 6 Potentiodynamic polarization curves show that the lower current density for concrete specimens containing 20 lb/yd^{3}NaCl after electrical injection of tetrabutylammonium nitrite for one week

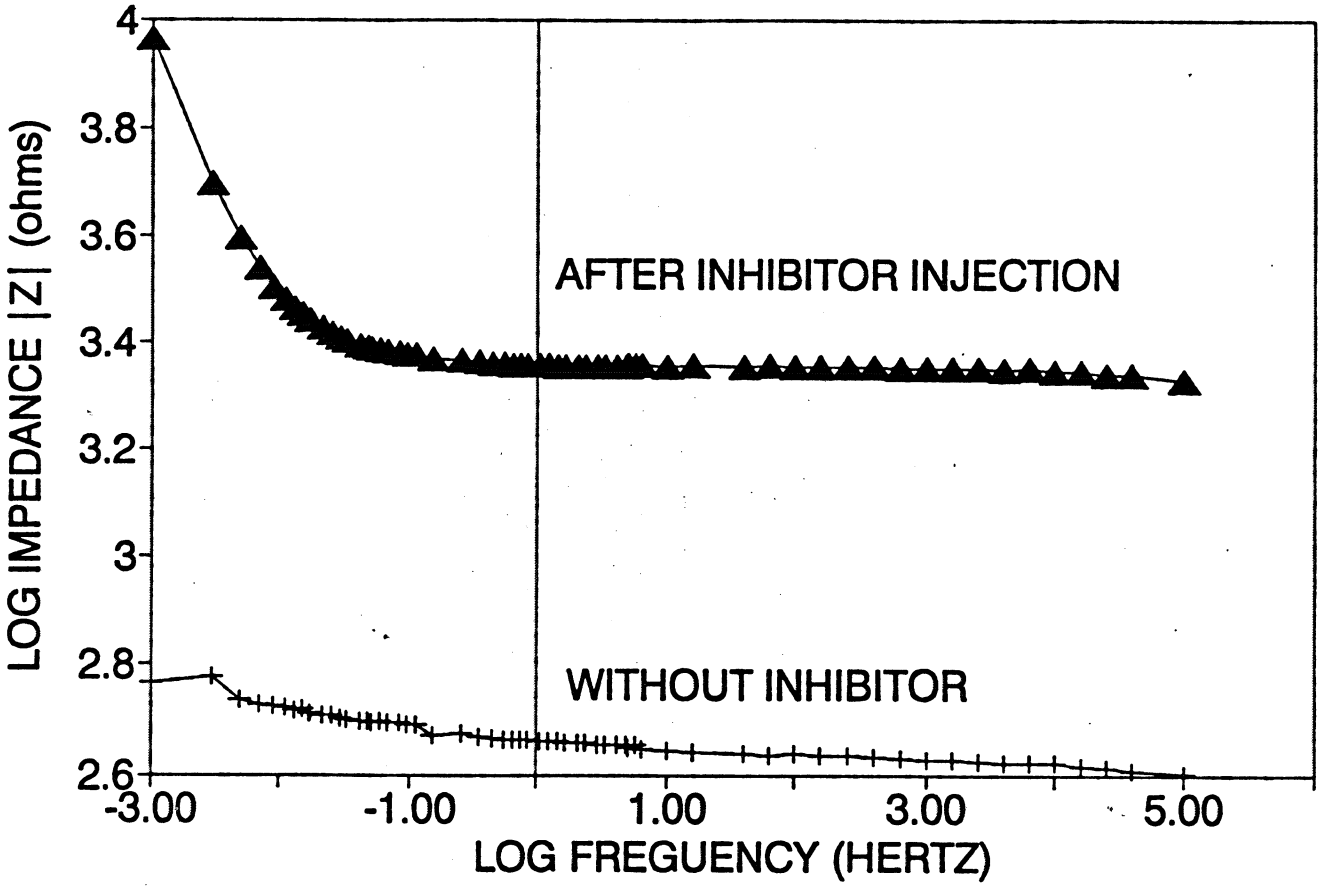

Figure 7 Bode plots showing that the higher value of R_p for concrete specimens containing 20 lb/yd^{3}NaCl with electrical injected inhibitor (tetrabutylammonium nitrite)

FUTURE STUDIES

Long term studies are being done to determine the efficiency of different inhibitors and to obtain optimum injection parameters like inhibitor concentration, electric field strength and frequency of application. Work is being done to synthesize higher efficiency inhibitors. The studies on the effect of electric field strength on the integrity of concrete structures are in progress.

In this project, studies will be performed to monitor the value of polarization resistance (R_p) and then calculate the efficiency of various inhibitors using the following relationships:

$$I_{corr} = \frac{b_a b_c}{2.303 (b_a + b_c) R_p} \quad \ldots\ldots\ldots\ldots\ldots (i)$$

where b_a = anodic tafel slope
b_c = cathodic tafel slope

Inhibitor efficiency (IE) is defined as:

$$IE = \frac{(I^o_{corr} - I^I_{corr})}{I^o_{corr}} x100 \quad \ldots\ldots\ldots\ldots\ldots (ii)$$

where I^0_{corr} = corrosion current in absence of inhibitor
I^I_{corr} = corrosion currents in presence of inhibitor

Since b_a and b_c are assumed to be constant for a particular metal in a given environment, we obtain from (i) and (ii):

$$IE = \frac{R^I_p - R^o_p}{R^I_p} x100 \quad \ldots\ldots\ldots\ldots\ldots (iii)$$

where R_p^I = polarization resistance with inhibitor
R_p^0 = polarization resistance without inhibitor

One of the most important advantages of the inhibitor method is the simultaneous removal of chloride ions while injecting inhibitors. Since Cl^- ions are negatively charged, they will tend

to move towards temporary anode and away from the rebar/concrete interface. So the applied electric field has two fold benefit, enhanced diffusion of the corrosion inhibitor towards the rebar/concrete interface and the migration of chloride ions away from the interface.

Studies will lead to the development of high efficiency inhibitors (90%-100%). It is also necessary to perform a long term study to determine the degree of retention of the inhibitor so that the information on the required frequency of inhibitor application can be obtained. Also studies involving the comparison of rebar corrosion following inhibitor injection against situations involving cathodic protection would be performed. It must be emphasized that cathodic protection requires permanent installation, whereas inhibitor injection requires only a few days temporary installation. Finally from a practical viewpoint, a study involving a pre-corroded steel rebar embedded in chloride-contaminated concrete would be used to gain information on the degree of protection afforded by inhibitor injection in a situation where corrosion is in an advanced state.

HYDROGEN EMBRITTLEMENT SUSCEPTIBILITY

INTRODUCTION

Many of the corrosion resistant alloys currently being used or being considered for use in hydrogen environment, including at KSC, have not been tested for their susceptibility to hydrogen embrittlement. These alloys are not currently being used in applications where hydrogen is a major constituent of the environment. However, with the need for more corrosion resistant facilities and equipment, these alloys are being considered as candidates for such applications. It is therefor necessary that these alloys be studied in some detail as to their hydrogen embrittlement susceptibility. The alloys included in the study are Nickel based alloys such as C-22, C-276, G-30 and Inconel 625 as well as 904L. Although it is generally known that Al and Ni as well as high strength steels are susceptible to hydrogen embrittlement, the degree of susceptibility and its dependance on micristructure and heat treatment has not been addressed yet in the literature. Our previous work on Ni based superalloys has underscored the point that in addition to chemical constituents of the alloy, microstructure affects the material's behavior significantly in terms of embrittlement and H diffusivity.

OBJECTIVES

1. To find the susceptibility to hydrogen embrittlement of various corrosion resistant alloys and establish a correlation between their microstructure and susceptibility.
2. To find the diffusivity of hydrogen in various alloys, relate it to their embrittlement susceptibility. Determine the nature of hydrogen traps and correlate with the microstructure of the alloy.

METHODOLOGY

Two techniques were utilized in the investigation of these alloys, slow strain rate testing (SSR) and hydrogen permeation testing. The source of hydrogen for both the SSR tests and the permeation tests were from electrolytic reduction of water. Electrolytic charging was chosen as a hydrogen source as it is safer to use than gaseous hydrogen and under certain thermodynamic conditions it can be as potent as several hundred atmospheres of gaseous hydrogen. The electrolyte for hydrogen charging was 0.1 N H_2SO_4 as it is less likely to promote film formation that inhibits hydrogen adsorption.

SSR testing is a mechanical test that subjects a tensile test specimen to constant extension at a low rate, typically 10^{-5} to 10^{-8} /sec. Test samples were run in both air and hydrogen charged conditions. Hydrogen charged specimens were electrolytically precharged for two weeks prior to testing, charging was continued during the test. The mechanical properties of the charged samples were compared to those of the sample tested in air to determine the extent of degradation. The fracture surfaces of the test specimens were then examined with the aid of a scanning electron microscope to determine if any brittle cracking has occured and to determine the effect of hydrogen on the nucleation of microvoids in ductile regions.

The hydrogen permeation test is a method of determining the diffusivity of hydrogen in an alloy and to determine the nature of the hydrogen trap sites, i.e, saturable or unsaturable. In this test, which is based upon the Devanathan-Stacharsky technique, hydrogen is evolved on one side of a thin foil of the alloy by cathodically polarizing it in H_2SO_4. A portion of this hydrogen adsorbed on the metal diffuses into the alloy foil. The opposite side of the foil is anodically polarized so that any hydrogen that diffuses through will be oxidized. The current from the oxidation reaction is monitored as a function of time. The current is initially zero and stays at this value for a period of time, then begins to rise until it reaches a maximum steady state value. After steady state, charging is stopped and the current drops back to zero. The diffusivity can be calculated from the current vs time plots. If the same specimen is again tested, the two plots can be compared to determine the type of hydrogen traps.

RESULTS

Nickel based alloys such as Hastelloys C-22, C-276, G-30, Inconel 625 and stainless steel 904L were tested for their susceptibility in annealed, cold worked (c.w) and c.w +aged conditions. The highly corrosive external KSC environment necessitates use of Ni based alloys although pure Ni is known to be susceptible to hydrogen damage.

These alloys were ranked based on the % loss in ductility, UTS and SEM observations. The scheme for ranking these alloys is shown in Figure 8.

(1) Hastelloy G-30 annealed
(2) Hastelloy G-30 annealed + aged
(3) 904L annealed
(4) Hastelloy C-22 annealed
(5) Hastelloy C-22 annealed + aged
(6) Hastelloy G-30 cold worked
(7) Hastelloy G-30 cold worked + aged
(8) inconel 625 annealed + aged
(9) Inconel 625 annealed
(10) Hastelloy C-22 cold worked
(11) Hastelloy C-276 cold worked + aged
(12) Hastelloy C-276 cold worked
(13) Hastelloy C-22 cold worked
(14) Hastelloy C-22 c.w. + aged

All alloys were susceptible to hydrogen. the first three were only slightly susceptible. Alloys 4 through 9 are moderately susceptible and alloys 10 through 14 are highly susceptible. C-22 showed absence of saturable irreversible traps which is good for hydrogen applications.

Figure 9 shows the effect H has on the degradation of mechanical properties of Hastelloy C-22. Table III lists Diffusion Coefficients determined for some of the alloys. Each Diffusivity number is an average of three to four independent experiments. The determination of the activation energy indicated in the table makes it possible to find diffusivity of H at any temperature of interest. Table IV summarizes the degradation in vaious mechanical properties of Hastelloy C-22 due to H exposure. Finally Figure 10 shows the fractographic evaluation procedure and results obtained for two alloys. Such evaluation was performed for all alloys.

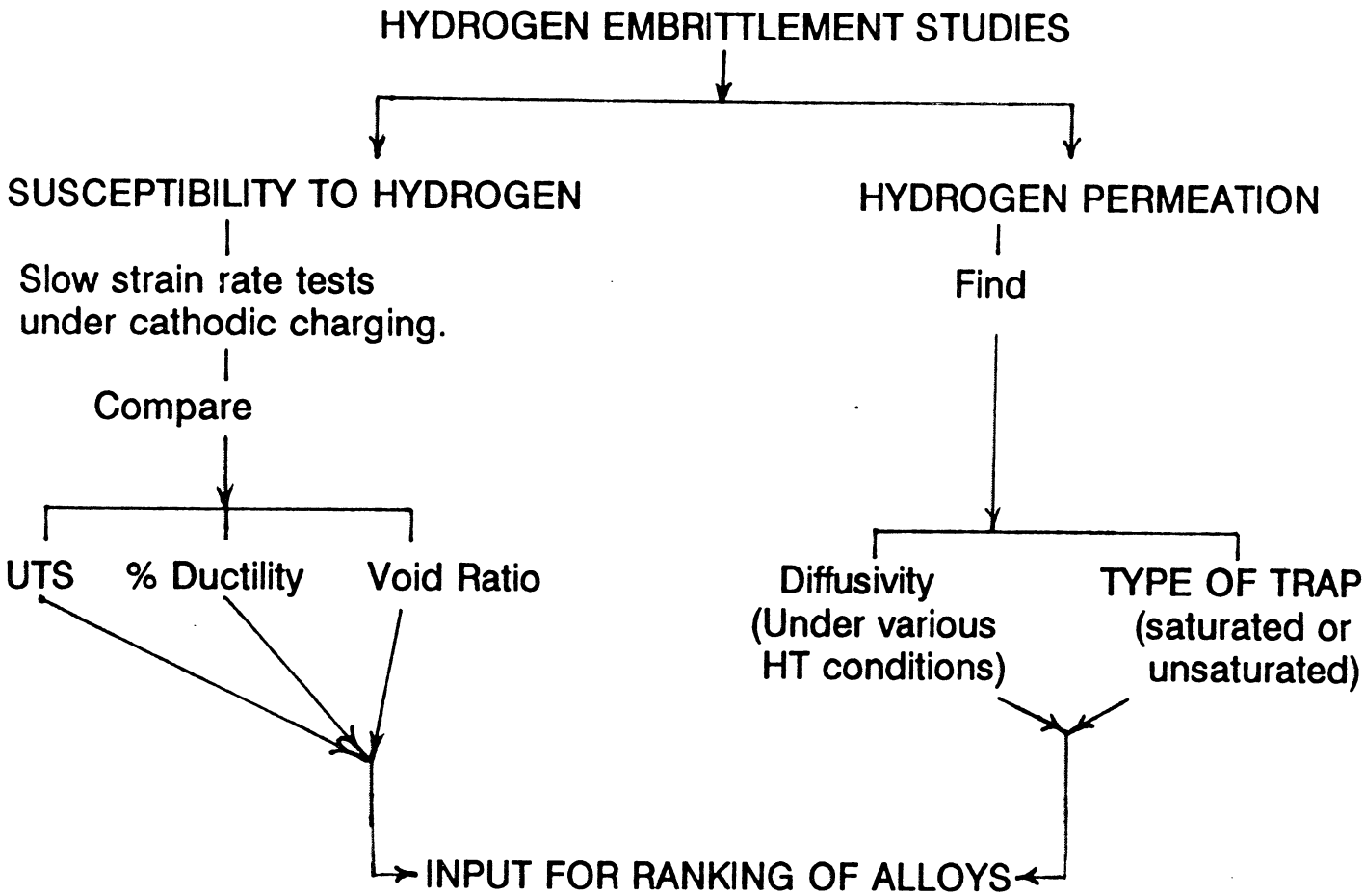

Figure 8 The Scheme For Ranking Of Different Alloys With Respect To Their Hydrogen Embrittlement

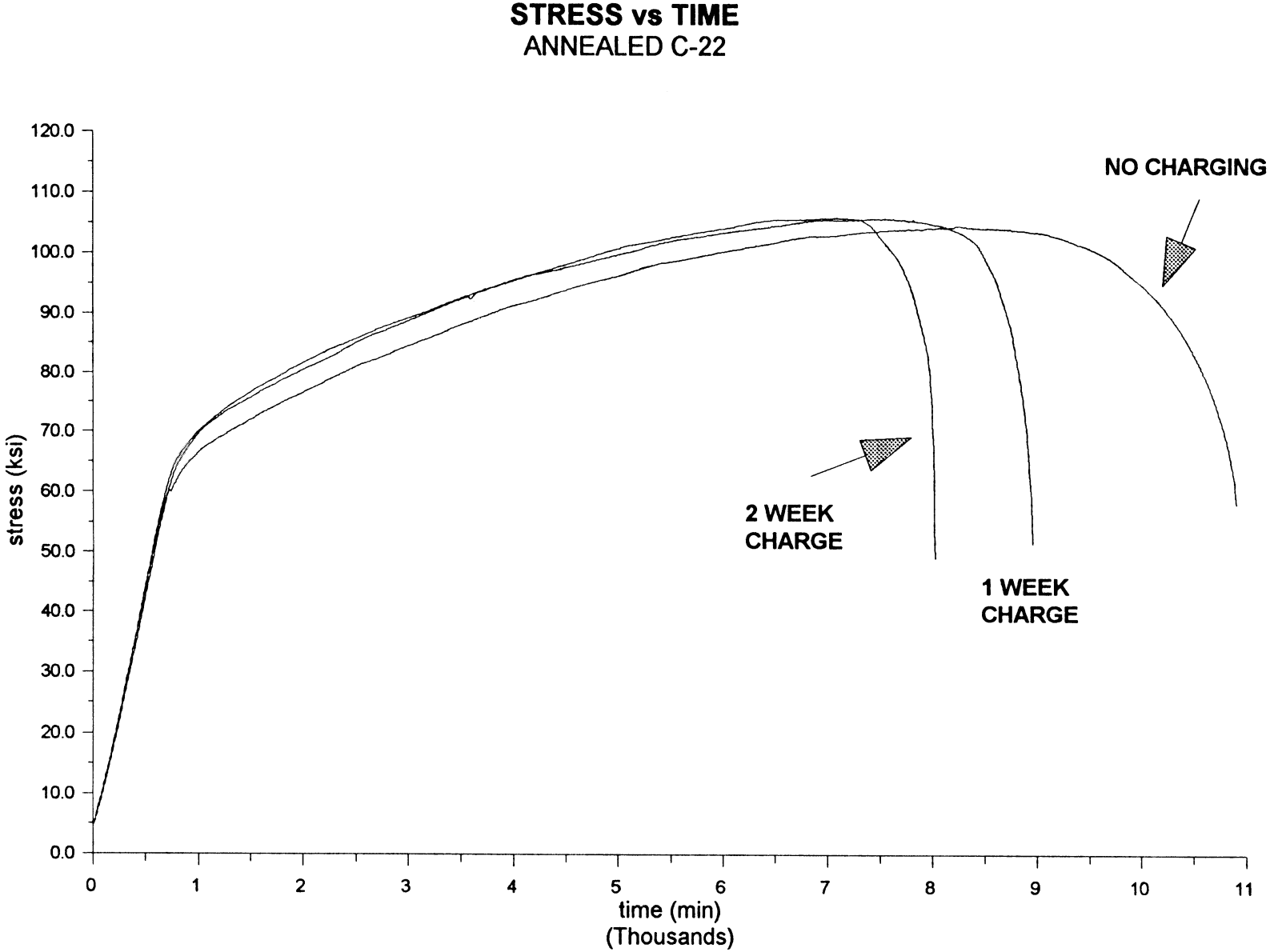

Figure 9 The stress-time behavior comparison for annealed Hastelloy C-22 with and without H charging under slow strain rate pulling.

DIFFUSION COEFFICIENTS

Alloy	Temperature	By lag time method(cm^2/s)
Hastelloy C-22	51°C	7.68×10^{-12}
INCONEL 625	42°C	3.86×10^{-11}

Activation Energy for Hydrogen Diffusion in Hastelloy C -22 is 49 KJ/mole

TABLE III DIFFUSION COEFFICIENTS OF SOME NICKEL BASED ALLOYS

MATERIAL	CHARGING TIME	TTF (min)	UTS (ksi)	STF (%)	RA (%)
C-22 ANNEALED	0.00	1.09E4	104.6	64.2	79.6
C-22 ANNEALED	1 WEEK	8.96E3	105.9	52.8	62.9
C-22 ANNEALED	2WEEK	8.02E3	105.9	46.2	55.3
C-22 A & A	0.00	9.84E3	104.5	57.2	73.8
C-22 A & A	1 WEEK	8.44E3	108.2	49.8	47.7
C-22 A & A	2 WEEK	9.02E3	107.4	51.8	49.5
C-22 CW	0.00	2.59E3	177.1	13.7	71
C-22 CW	2 WEEK	2.23E3	172	10.55	36
C-22 CW & A	0.00	3.30E3	176.6	17.8	45.6
C-22 CW & A	2 WEEK	1.85E3	187	10.1	17.9
904L ANNEALED	0.00	5.28E3	105.7	32.4	68.4
904L ANNEALED	2 WEEK	5.40E3	105.4	29.4	62.5

A & A - ANNEALED & AGED
CW - COLD WORKED
CW & A- COLD WORKED & AGED
TTF - TIME TO FAILURE
UTS - ULTIMATE TENSILE STRENGTH
STF - STRAIN TO FAILURE
RA - REDUCTION IN AREA

Table IV Table of Mechanical Properties Tested Under Slow Strain Rate Condition Under Charged(1 Week and 2 Weeks) and Non-charged Conditions

HYDROGEN EMBRITTLEMENT TESTS (SSR) FRACTOGRAGHIC EVALUATION RESULTS

MATERIAL	CONDITION	DIMPLE SIZE RATIO (R)	
		AT THE CENTER	OUTER SURFACE
INCONEL 625	ANNEALED	0.9	0.45
INCONEL 625	AGED	1.25	0.57
HASTELLOY G30	ANNEALED	1	0.7

$$R = \frac{\text{DIMPLE SIZE WITH HYDROGEN CHARGING}}{\text{DIMPLE SIZE WITHOUT HYDROGEN CHARGING}}$$

$R > 1$: HE DUE TO ENHANCED VOID GROWTH

$R < 1$: HE DUE TO ENHANCED VOID NUCLEATION

Figure 10 The Fractograhic Evaluation involved taking scanning electron micrographs and measuring the void ratio of Dimples as shown above. A ration other than Unity indicates H susceptibility.

TECHNICAL DISCUSSION

Hydrogen has been known to have a deleterious effect upon metals since the late 1950's. Damage due to hydrogen can manifest itself in several different forms, these include blistering, decarburization and embrittlement. Blistering occurs at both low and high temperatures. At low temperatures hydrogen collects at internal microvoids and fissures. The pressure in the microvoid builds as more hydrogen migrates to the site, eventually the pressure exceeds the flow stress of the alloy and plastic deformation occurs. Further increase in hydrogen pressure causes adjacent microvoids to link together and form macroscopic cavities. When these cavities are near the surface they bulge out and appear as blisters. At elevated temperatures two other mechanisms can also lead to blistering, they are decarburization and deoxidation reactions. In decarburization hydrogen reacts with carbon in cementite or carbides to form methane gas. The methane acts in the same manner as hydrogen to produce blistering. Deoxidation produces blistering when hydrogen reacts with oxide inclusions in the metal and form water vapor. The water vapor then acts as the source of pressure responsible for blistering.

Decarburization is an elevated temperature process that is often the precursor to blistering, though it often produces failure without any occurrence of blistering. Hydrogen reacts with carbon in the form of cementite or carbides to form methane gas thereby removing carbon from the metal. The carbon in these alloys is often the principal strengthening mechanism and its removal results in lowered strength and poorer creep resistance.

Hydrogen embrittlement is the deterioration of a material's mechanical properties in the presence of hydrogen. Often a normally ductile material will fail in a brittle manner when exposed to a hydrogen containing environment and tensile stress. The mechanisms of hydrogen embrittlement are not well understood. Hydrogen is believed to reduce the cohesive strength of the metal, particularly at grain boundaries, thereby reducing the amount of energy to produce a fracture. Grain boundary segregation of sulfur, phosphorous and tin are known to increase susceptibility to hydrogen embrittlement. Hydrogen is known to promote the initiation of microvoids in ductile metals such as nickel and some of its alloys, this results in lower ductility and strength.

A critical hydrogen content must be reached before brittle cracking can occur in a particular alloy. Metal under applied stress can have a higher hydrogen concentration than the metal in unstressed condition. Applied stress also increases the apparent diffusivity of hydrogen in the metal, presumably by dislocation transport. There are two general types of hydrogen trap sites in metals, saturable and unsaturable. Saturable traps have high binding energies that permanently bind the hydrogen to the trap, the metal must be melted in order to liberate the hydrogen. Unsaturable traps have much lower binding energies and hydrogen can migrate in and out of these trap sites much more readily. Metals which contain saturable types of traps are more susceptible to embrittlement.

Hydrogen embrittlement can be mitigated by two methods, diffusion barriers and alloy selection. Diffusion barriers are coatings which decrease the rate of absorption of hydrogen into the metal thereby increasing the time needed to reach a critical hydrogen concentration. This technique works best when the hydrogen exposure is intermittent in nature, but at long times it becomes less effective. Alloy selection is a more practical solution for long term applications. Corrosive environment are of particular concern with regards to alloy selection. The importance of this is due to fact that hydrogen is a significant byproduct of corrosion, therefor an alloy that is resistant to both corrosion and hydrogen embrittlement is desirable. It should be pointed out that alloy selection should also consider the microstructure.

Human Factors Analysis of Orbiter Processing Tasks Involving Visual Inspection for Low Probability of Occurrence Events

A Final Report

Presented To
National Aeronautics And Space Administration
John F. Kennedy Space Center
Kennedy Space Center, Florida

Presented By
William W. Swart, Ph.D., P.E.
Yasser A. Hosni, Ph.D., P.E.
Robert R. Safford, Ph.D., P.E.
David F. Kennedy
Bert A. Yadi
Bartricia A. Williams
Department of Industrial Engineering
And Management Systems
University of Central Florida
Orlando, Florida

Human Factors Analysis of Orbiter Processing Tasks
Involving Visual Inspection
for
Low Probability of Occurence Events

INTRODUCTION

The high quality of work performed in most Orbiter processing activities and the relatively low rate of occurrence of quality incidents paradoxically can be expected to lead to a particular type of human factors problem. This occurs in tasks where human operators or inspectors are required to detect the occurrence of "Low Probability of Occurrence" events. It is known that in tasks of this nature, there is a "high probability" of failing to detect these low probability of occurrence "events". This phenomenon occurs in most types of tasks where detection of low probability events is required and occurs despite the degree of training, skill, and alertness of the inspector or the apparent obviousness of the event to a person not involved in the inspection.

This problem has been demonstrated in numerous tasks such as air defense radar monitoring, microscopic inspection of tissue for cancer growth, and a variety of industrial type inspections for defects. This problem is frequently called "the vigilance problem" or "phenomenon" in the literature.

This component of the Cooperative Agreement research activity was designed to demonstrate the potential for "vigilance" problem occurrence in Orbiter processing tasks and to determine factors influencing the vigilance-induced performance errors in Orbiter processing.

Literature Summary

The literature on vigilance and associated problems in industrial inspection is extensive. A summary of literature relevant to the problem addressed in this project component is presented in Table 1. The references presented in the table are separated into categories which help identify the variables that can be expected to influence the vigilance phenomenon and the remedial actions that can be undertaken to alleviate vigilance-induced problems.

Orbiter Processing Tasks

Examples of Orbiter processing tasks which could be expected to experience this problem because of the task structure and the relatively low probability of occurrence of events include:

- STR system post flight inspection
- TPS post flight and roll out inspections

Signal Rate	Desse and Ormand, Fortune, Kappauf and Powe, Jenkins
Signal Magnitude	Adams, Fortune
Human Characteristics:	
Gender Differences	Dember and Hancock
Team Size	Baker and Salas
Visual Acuity	Long and Rourke
General Suggestions for Improvement:	
Environmental Distractions	Galinsky et al.
Rotation of Workers	Loeb et al.
Proper Training	Williams
Secondary Task	Wiener
Time of Day	Craig et al.
Human Interest, Behavior and Clarity	Cole et al.

Table 1:

Summary of Vigilance Literature Relevant To Project Component

- ECL radiator inspection prior to roll out
- STR system aft close-out inspection for removal of access equipment
- INS, COM, EPD electrical systems connection inspection

All of the above tasks involve visual inspection and the need to recognize the presence of a low probability of occurrence condition. Although the condition or event needed to be detected may seem "obvious" (e.g., unconnected electrical connectors, beam in aft, indentation in tile, etc.) research in the problem area suggests that error rates in the neighborhood of a 1 in 10 chance of failure to detect may occur when there is a probability of event occurrence of 1 in 100. Probability of inspection task failures would be expected to increase as the probability of occurrence decreases.

For purposes of this project, two experiments were designed and executed. These tasks involved simulation of two Orbiter processing activities. The Orbiter processing tasks simulated in this study were:

- Post flight inspection of TPS (Thermal Protection System) tile gaps for charred gap filler material.
- Pre OPF (Orbiter Processing Facility) "roll out" inspection of TPS tile gaps for presence of processing shims.

The reasons for selecting these particular tasks included:

- The tasks are easily learned so that any vigilance decrement observed in the performance of the tasks should not be confounded with learning effects.
- The tasks do involve low probability of occurrence events. Given 25,000 or more tiles on the vehicle (depending on the particular vehicle being inspected) there are relatively few gaps in which shims are left after processing or in which burned gap filler is found.
- The tasks are the type of inspection task which the ample literature on vigilance suggests would be candidates for a vigilance effect.

Experiment I

The inspections described above are done by the technicians who work under the vehicle and look directly up at the tile gaps. The viewing distance in these inspection situations varies from about one foot to five feet. To simulate this situation, subjects in the experimental situation were required to look at successive iterations of the pattern shown in Figure 1. This pattern, which is similar to the tile patterns exhibited on the underside of the Orbiters, was projected on a white matte ceiling surface above the subjects and was adjusted to enable the simulated tile size to approximate an actual 6" by 6" "acreage" tile in terms of the visual angle subtended by the image.

Subjects participating in this task were required to view the image patterns and determine whether any gaps contained the presence of a "target" (i.e., whether the gaps were filled with a bright orange color or a dark brown color).

The major effects examined in the study were the color of the target material in the gaps between the tiles and the degree of visual difficulty. Figure 2 presents a schematic of the experimental design for these two effects.

One of the target colors chosen was orange, a relatively high contrast color compared to the back (or gray) of the tiles and the color of one of the widely used processing shims. The other color was a "low contrast" brown, the color of some of the darker plastic shim material and a color similar to that of burned gap filler material.

Low difficulty targets were those that were relatively large (i.e., filled wide gap for the length of a tile) and were located in the central area of the visual field. High difficulty targets were smaller and were located in the peripheral areas of the visual field.

Forty subjects were tested. Each subject viewed 500 presentations of the "tile pattern" image. These images were presented for a viewing time of 5 seconds. Signal rate for both the orange and brown signals were 9%. Four out of each nine of each color signals were classified as high difficulty, while the remaining five were classified as low difficulty signals.

RESULTS OF EXPERIMENT I

The results of the statistical analysis of this experimental study are shown in Figure 3. As can be seen in the figure, both major effects of interest (i.e., color and task difficulty) were significant. In addition, two significant interactions were noted.

The effect of color on target identification, the most significant effect, are shown in Figure 4. As can be seen, subjects correctly identified 93% of the orange targets (Note: that still corresponds to a "miss rate" of 7%, a rate that could be expected to increase if the signal presentation rate of 9 per 100 were lowered). Brown, on the other hand, produced a "miss rate" of 40%. Only 60% of brown targets were correctly identified.

CONCLUSION OF EXPERIMENT I

This study demonstrated that a vigilance effect could be expected in Orbiter processing tasks and delineated, for the selected Orbiter processing activities, factors influencing the performance decrement. Knowledge of these effects can be readily used by process designers or in process improvement activities to help eliminate problems arising from vigilance tasks.

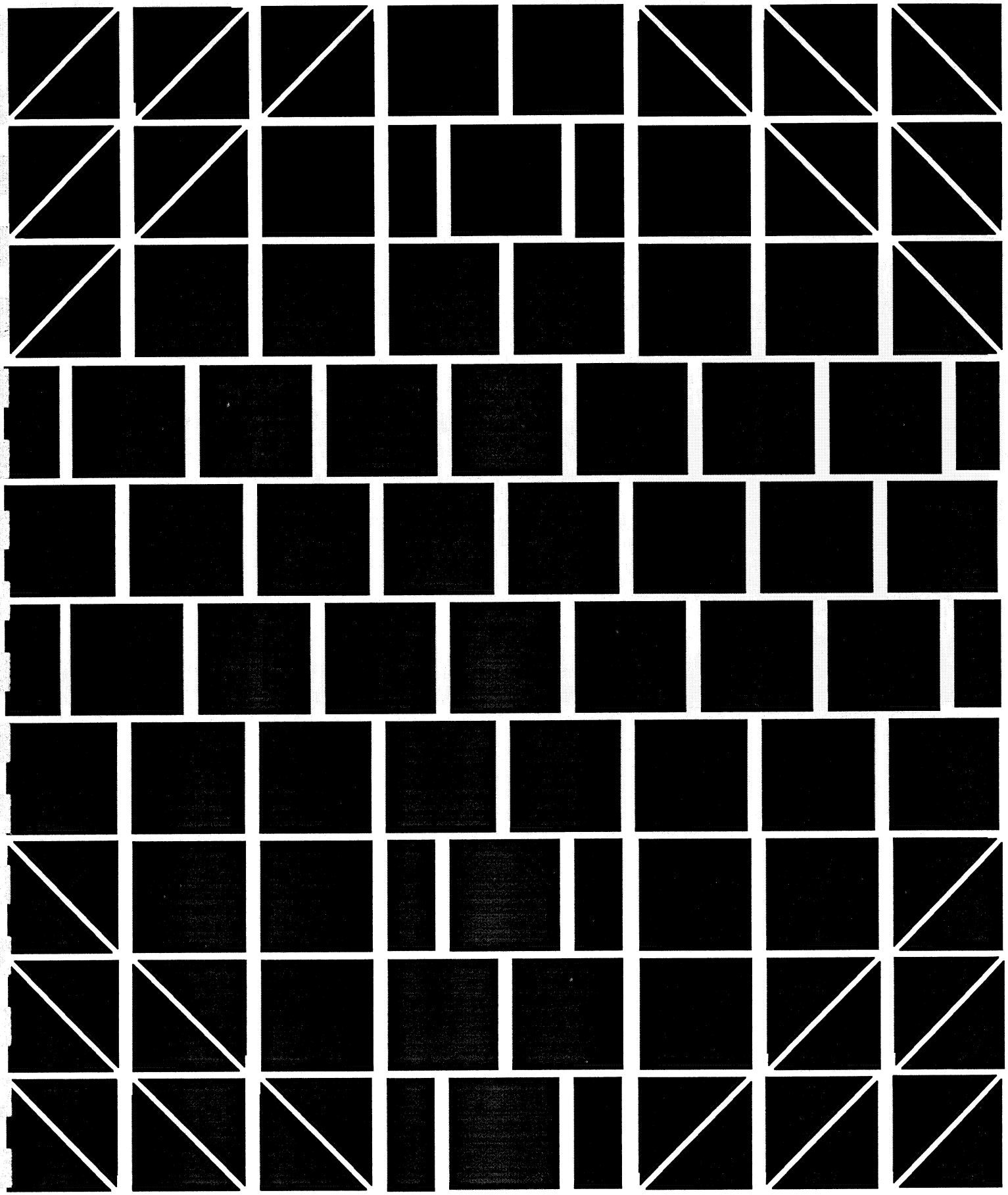

Figure 1:

Simulated Tile Pattern Configuration Used In Experiment 1

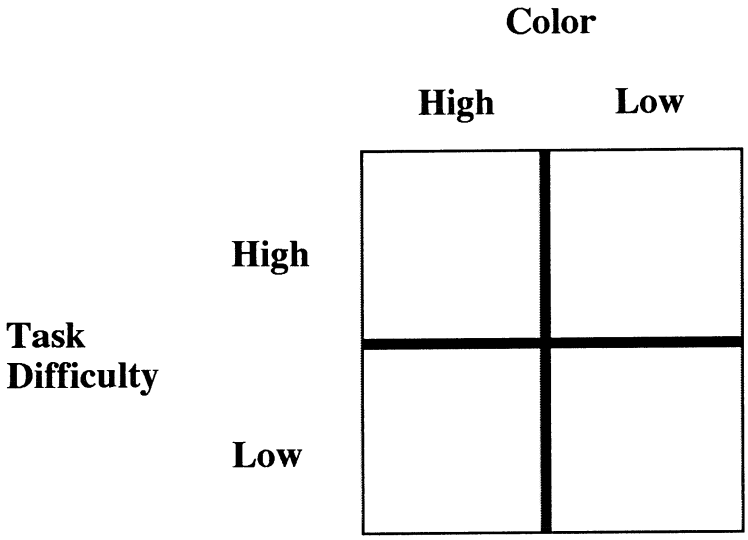

Other Factors Considered:

* **Time in the Task (Phase)**

* **Corrective Refraction (Corrective Lenses Y/N)**

* **Sex (M/F)**

Figure 2:

Experimental Design For Experiment I

Factor	Significance	Results
Main Effect:		
Color	<<.005	Highly Significant
Task Difficulty	.025	Significant
Interactions:		
Refractive Correction X Color	.001	Highly Significant
Task Difficulty X Color	.018	Significant

Figure 3:

Experiment 1 Significant Effects

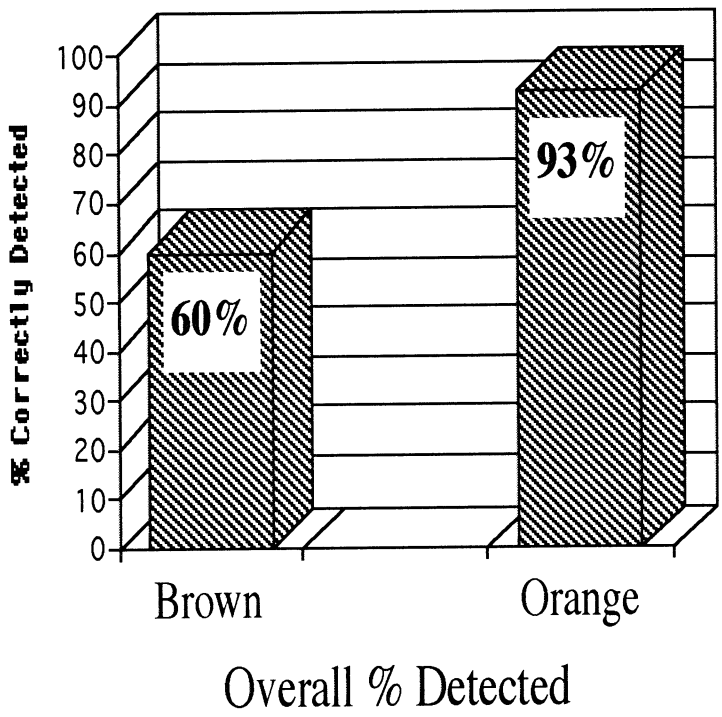

Figure 4:

Color Effect on Signal Detection

Experiment II:

The results of experiment I were deemed significant enough to warrant further experimentation in an environment with higher fidelity to actual Orbiter Processing Access to the actual Orbiter vehicles, for purposes of experimentation of this nature, was not available. Arrangements were made with TW recreational Services and Ringling Enterprises at the Spaceport U.S.A. at the Kennedy Space Center Visitors Center to gain access to the full scale Orbiter Model, Ambassador, for the conduct of a site study. In this site study of experiment II, subjects searched the tile gaps on the underside of the Orbiter model Ambassador seeking to identify the locations where 6" by 1/8" strips of shim stock material had been placed on the model substrate.

EXPERIMENTAL DESIGN FOR EXPERIMENT II

The experimental design for experiment II, the site study at the Kennedy Space Center, is shown in the diagram of Figure 5. As indicated in the figure, three independent variables of interest were investigated. These included:

- target color
- signal rate
- team size

Target color was found in experiment I to be the independent variable with the largest effect on the dependent variable of signal detection. In experiment II, two levels of signal color were employed in experiment I.

Signal rates of 9 per 100 were employed in the first experiment with an inter arrival average time of 55.5 seconds. This signal presentation rate was adopted as the high rate for experiment II. The low signal rate adopted for experiment II was a rate one-fourth that of the higher rate. The lower rate involved presentation of target signals with an inter arrival interval averaging approximately 3 minutes and 45 seconds.

The third independent variable in experiment II was team size. Subject inspectors engaged in the search task of experiment II worked either individually or in pairs.

Experiment II. Experimental Procedure

As mentioned previously in the study of experiment II, subjects searched the tile gaps on the underside of the Orbiter model Ambassador to find and identify the location of 6" by 1/8" strips of shim stock material that had been placed on the model substrate surface. Under the high signal rate conditions, subjects were presented with 24 randomly placed targets along a path covering the underside of the models starboard side. On the low signal rate condition, 6 targets

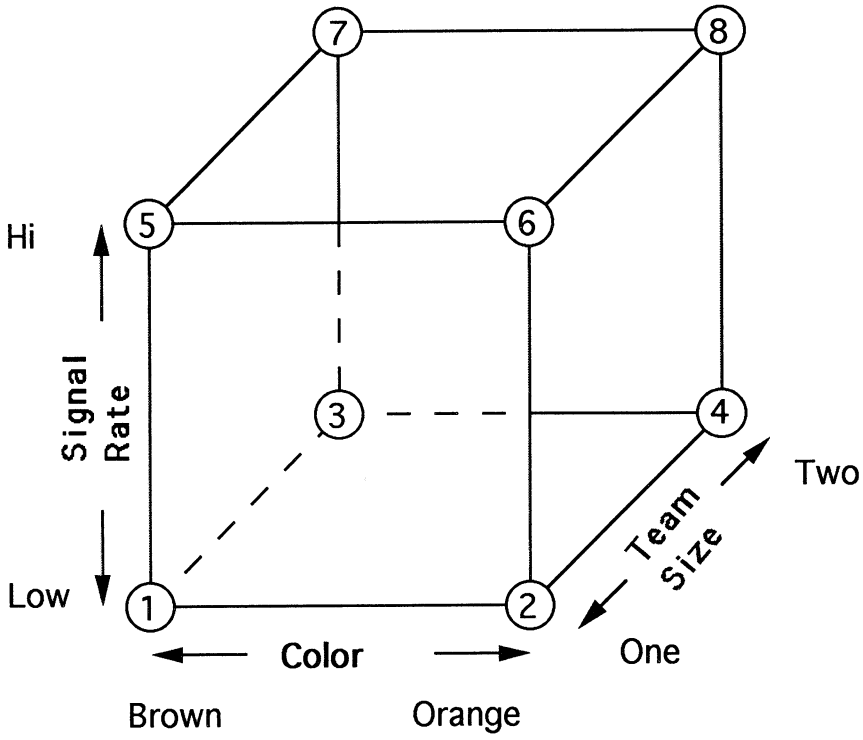

Figure 5:

Experimental Design For Experiment II

were randomly placed in gaps along the path. Figure 6 presents a diagram of the path and shows the locations of the targets under the high signal rate conditions. Subjects searching either as individuals or in pairs followed the prescribed path marked by tape on the ground under the Orbiter model. This tape included location markers at every one foot interval. When a target was located, the location of the target was noted by the subjects on a score sheet which was provided to them. The length of the path followed by the subjects was such that subjects proceeding in a "normal" pace as determined in pilot investigations conducted prior to experiment II would encounter signals at the desired signal presentation rate.

Experiment II Results

The second experiment conducted with 40 subjects and with the use of the Orbiter model Ambassador yielded results which confirmed and enhanced the results of the first experiment. These results are discussed below:

Effect of Target Color

The statistically significant effect of most practical value from the initial experiment was the effect of target color on task performance and the degree to which the vigilance phenomenon errors were present in the results. The same effect in a magnitude close to that observed in the first experiment was present in the second follow on-site study conducted at the Kennedy Space Center.

More specifically, the effect of the independent variable, target color, on the dependent variable present correct detections, is shown in the bar chart of figure 7. As can be seen, when the target color of the shims being searched for was the more visible orange color, 90.5% of the targets were identified, on the average, by the subjects. When the "less visible" brown shims were being sought the average percentage of shims that were detected dropped to 73.1%. The effect of the color change was therefore equivalent to a 17.4% shift in detection percentage across all subjects who participated in the experiment.

The results achieved above are very similar to those achieved in experiment I where the overall percentage of correct detections of orange "shims" was 93% and the overall percent correct detections of the brown shims was 60%.

Other Effects Observed in Experiment II

The cube of figure 8 presents the summary results of the 2^3 experimental design of the second experiment. The number in the "box" is the average value across all subjects of the

Subject Path for Experiment II And Target Location-High Signal Rate Condition

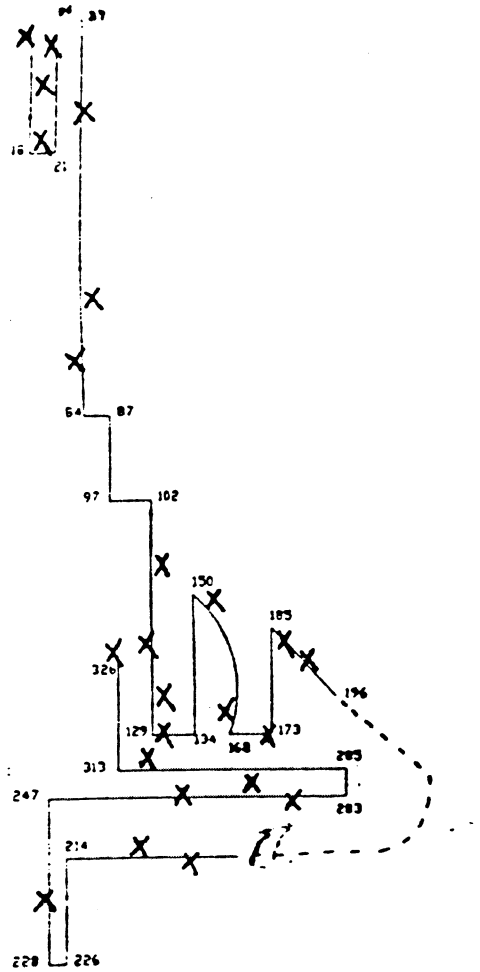

Figure 6

UCF/NASA-KSC "Vigilance Phenomena" Study January 8, 1993

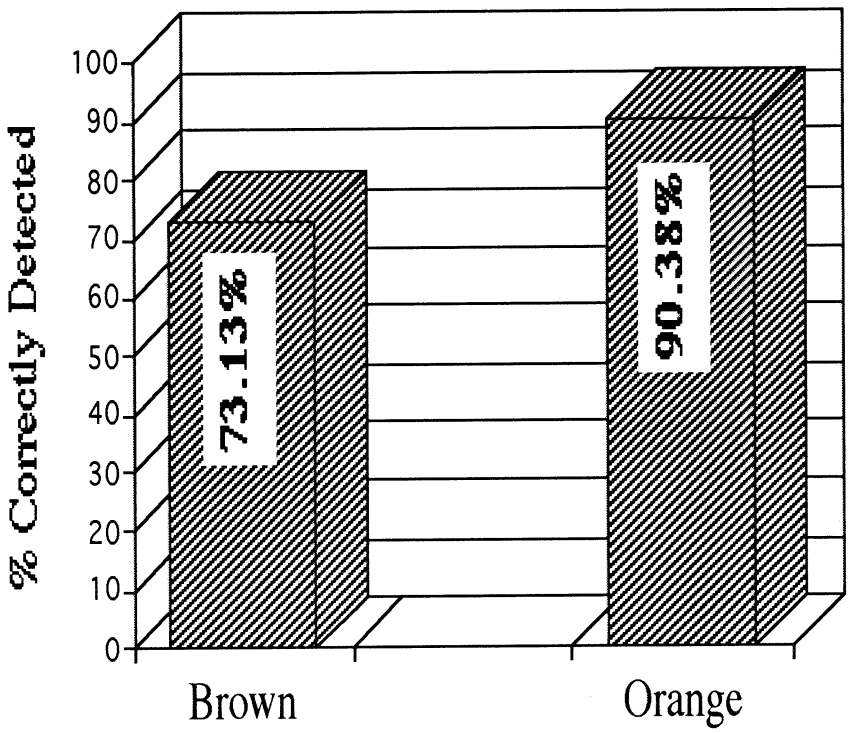

Figure 7:

Experiment II K.S.C. Site Study For All Subjects

"percent correct identification" of targets under the conditions represented by the corner. The figure illustrates, for example, the 95% of the orange targets were identified under the low signal rate condition when individuals searched for targets. Similarly, 77% of the brown targets were detected under high signal rate conditions by teams of inspectors.

The information contained in the overall experimental summary was analyzed using 2^n factorial experimental analysis procedures. The results of that analysis are presented in Table 2. Effects associated with the individual independent variables and the interaction effects for combinations of the independent variables were computed from the analysis and are presented in Table 3 and the "Dot Diagram" of figure 9. As can be seen in the effects summary and the dot diagram, the magnitude of the effect associated with target color is .174. This, the largest of the effects and the most practically significant, indicates that there is, overall, a 17.4% increase in the magnitude of the response measure, percent correctly identified as we move from the "low" level of color (brown) to the "high" level (orange). This 17.4% value is in fact the difference between the 90.5% detection value with orange and the 73.1% value with brown observed and commented on earlier. Team size is the next highest effect. As indicated by the value .084 for that effect, and 8.4% increase in percent correctly identified is observed as inspection team size is increased to two from one. The signal rate effect and the three way color by team size by signal rate interaction are also seen as relatively strong on the "dot diagram" summary of the effects.

Comments on Team Size

As indicated above, increasing team size from one inspector to two inspectors produced an 8.43 increase in the percent of targets that were correctly identified in the experiment. A more complete review of the results for the different team sizes can be seen in Figure 10. As indicated in the figure, an increase in team size resulted in a 2.2% increase in the percentage of brown targets detected of 14.3%. The average of these two values yields the 8.4% difference calculated earlier (the average of 14.3% and 2.2% is 8.25%. Difference from 8.4% calculated previously is due to "rounding" done at different places in different analyses).

These results might at first be interpreted to suggest that two person, simultaneous inspection is preferred to individual inspection (in fact, many inspection procedures in Orbiter processing are done by teams of two or more individuals). Another alternative inspection mode that should be considered is that of independent inspection by two or more inspectors. The set of "bars" at the far right present the hypothetical values that would be realized in the inspection task of experiment II by pairs of inspectors searching independently for targets. The values of 88% correct detection for brown targets and 98.85% correct detection for orange targets are computed by application of "reliability" analysis procedures appropropriate for parallel redundancy systems. For example, if one inspector is expected to correctly identify 66% of the brown targets (i.e., miss 34% of the targets) then the expected "miss" percentage of two independent, assuming random placement of target misses, is .34 x .34 = .1156 or about 12%. The expected overall correct detection of brown targets would be about 88%.

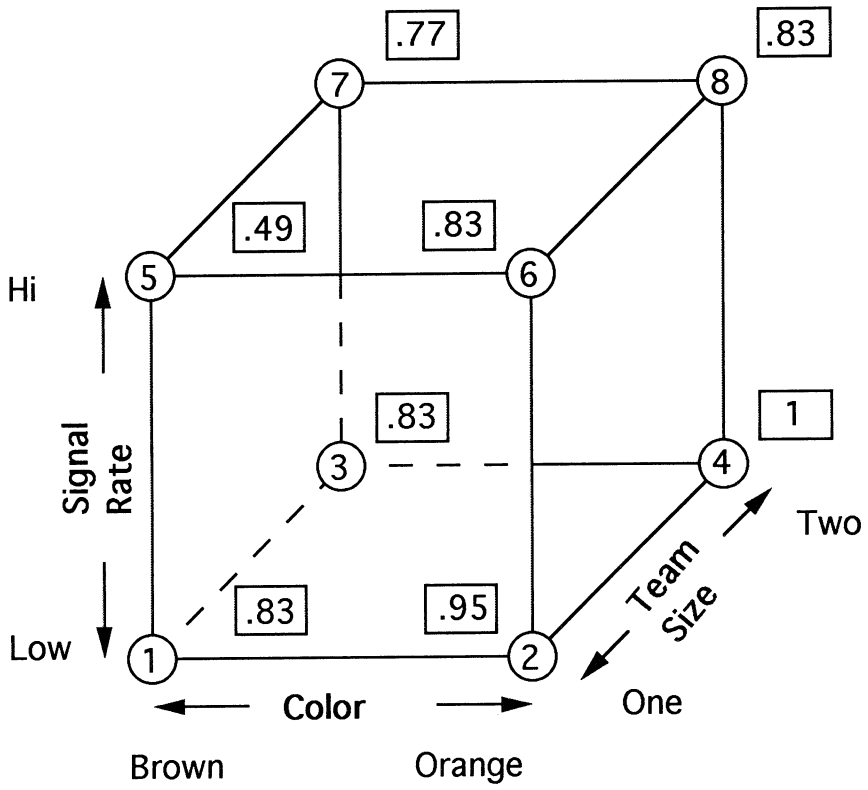

Figure 8:

Experiment II Effect Summary For All Subjects

Corner	Effects							Response
	C	T	S	CT	CS	TS	CTS	
1	-	-	-	+	+	+	-	0.83
2	+	-	-	-	-	+	+	0.95
3	-	+	-	-	+	-	+	0.835
4	+	+	-	+	-	-	-	1.0
5	-	-	+	+	-	-	+	0.489
6	+	-	+	-	+	-	-	0.835
7	-	+	+	-	-	+	-	0.77
8	+	+	+	+	+	+	+	0.835

Table 2:

2^n Analysis Matrix

Effects		Results
c	.696/4	0.174
T	.336/4	0.084
TC	-.236/4	-0.059
S	-.686/4	-0.172
SC	.126/4	0.032
TS	.226/4	0.565
CTS	-.326/4	-0.815

Table 3

Effects Associated With Experiment II

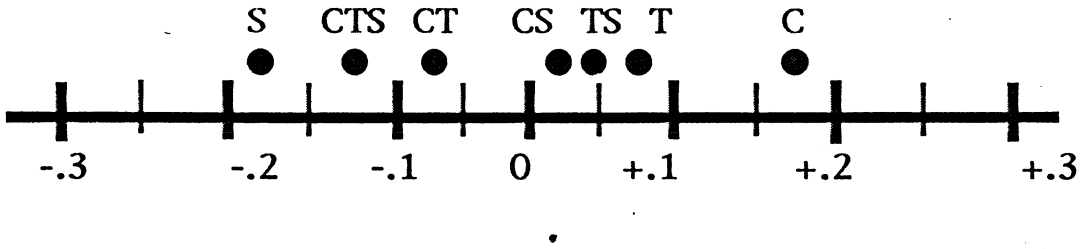

Figure 9

Dot Diagram Presentation Of Experiment II Results

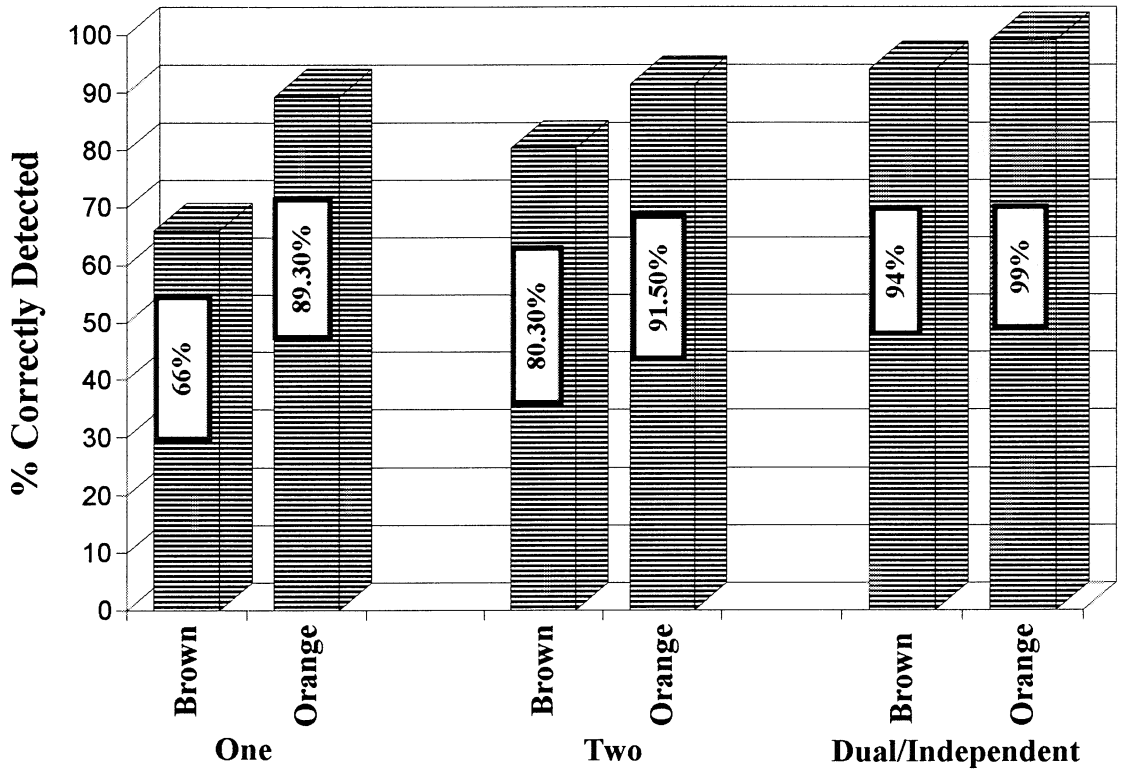

Figure 10:

Experiment II K.S.C. Site Study For Team Size Effect

Recommendations

The human factors experiments summarized in this report and previously summarized in project reviews with PT and TP-OAO representatives suggest a number of specific recommendations for changes in Orbiter processing procedures and for future activity directed toward identification and removal of vigilance phenomena problems. The recommendations are divided into three categories which are described below:

- Category 1: Specific Recommendations Related to Visual Inspection for Processing Shim Removal
- Category 2: Recommendations for Collection of Data Related to Vigilance Incident Occurrence
- Category 3: Recommendations for Comprehensive Process Review to Enable Identification of Processes with High Potential for Vigilance Decrements.

Specific Recommendations Related to Visual Inspection for Processing Shim Removal:

As mentioned, the visual inspection tasks incorporated in experiments I and II approximated the type of inspection that is performed in a "walk down" manner by technicians, engineers, and quality personnel when inspecting tile gaps for unremoved processing shims, burned gap filler or other "target" conditions. The results of those experiments and the results of observations by project personnel of inspection tasks being performed during actual Orbiter processing activities have resulted in a number of specific suggestions for reducing the potential for vigilance errors in the task of inspecting tile gaps for unremoved processing shims.

These suggestions include:

1) Change the color of the five thousandths inch brown shims to another more visible color having greater contrast characteristics with the Orbiter tiles. The results of both experiments I and II indicate the potential for vigilance performance decrement reduction that can be expected from substitution of colors with the visibility of orange shims for colors like the current brown.

2) Adopt the practice of making processing shims sufficiently large to extend beyond the outer mold line surface (OML) of the tile whenever possible. The visual task of searching for an object protruding from a tile gap is a much "easier" visual task than that of looking into a gap, even a large gap, for a target. In addition, the task of searching for a protrusion is less likely to be subject to vigilance-type performance decrement.

The above changes should be capable of relatively easy implementation. The next set of

recommendations would involve a slightly increased level of difficulty to implement.

3) Flag the processing shims: Cutting shims to a size that protrudes beyond the boundary of the gap is itself an example of flagging. Other methods of flagging are possible and have been suggested by technicians and engineers. These alternate methods would involve attaching an object to the shim, a string or a tag, that would protrude and serve as a "flag" to the presence of a shim. A consideration with respect to this suggestion is that the flag would alter the dimension of the shim at a point where the flag is attached. Consequently, shims would most likely have to protrude beyond the gap to begin with in order to provide an acceptable attachment point for the flag. The presence of a flag would increase the visibility of the targets and reduce the vigilance decrement potential.

4) Adopt an "accounting" system for tracking the placement of shims on the Orbiters. Currently. no records are kept of the number of shims that are placed on the vehicles during processing or the location of the shims. A shim that is inadvertently left on the vehicle by a processing technician will likely not be removed unless found in a "walk down" type inspection; the type of inspection that is most subject to vigilance type error. Adoption of an accounting system would provide a method for tracking the placement and removal of processing shims.

5) Task management is needed to minimize the vigilance decrement potential. Managerial approaches, discussed in the vigilance literature, could also be used to reduce the vigilance potential of tasks involving searching tile gaps for targets. Examples of managerial approaches would include control of inspection duration and inspection team size.

Another approach that can be employed to reduce the vigilance problems involves automation of the inspection process. Inasmuch as the vigilance problem is due to a basic human failing in inspection task ability, removing the human inspector from the task can improve performance if an effective automated target detection procedure is available.

Recommendations for Collection of Data Related to Vigilance Incident Occurrence

A second category of recommendations relates to the collection of data to quantify the actual occurrence of events that are likely associated with the vigilance phenomenon in Orbiter processing. In the course of the conduct of the project being reported here, project personnel asked the question of NASA engineers, LSOC engineers and processing technicians, "How often have processing shims been left on the vehicles when they should have been removed?" Anecdotal information suggesting that it was "not frequent but not uncommon" was readily

available. In fact, project personnel in the process of observing a tile bonding process observed a technician leave an orange shim in the gap of a newly bonded tile. The same personnel also later observed an "inspection" of the tile from below by a technician in which the presence of the orange shim went undetected (after the inspection, when technician attention was called to the particular gap by those who had observed the shim, it was immediately detected).

Despite the availability of anecdotal information, data that would enable quantification of this particular type of vigilance phenomenon occurrence is not available. Discussions by project personnel with TPS engineers indicates that when a "vigilance event" is detected (e.g. the presence of a target missed in a previous inspection) there is no mechanism that guarantees that the event will be recorded. With respect to the removal of previously undiscovered tile processing shims, no standard format exists for reporting the event if it is recorded.

It is recommended that for processes which are identified as having a "high" potential for the occurrence of "vigilance" events that mechanisms for the recording of the occurrence of the events be established. These mechanisms which would not have to be elaborate in nature could be developed as part of the Orbiter processing activity review process described in the next set of recommendations.

Recommendations for Comprehensive Process Review:

The research that was conducted on this project component has demonstrated the likelihood of the occurrence of vigilance problems in Orbiter processing tasks. The specific tasks that were addressed in the process simulations embedded in the experiments conducted were:

- post flight inspection of tile gaps for burned gap filler material
- pre-OPF roll out inspection of tile gaps for unremoved processing shims

These tasks were chosen for the simulation because, as indicated earlier, they possessed characteristics that identify them as highly likely to be subject to the vigilance phenomenon.

Other Orbiter and Shuttle processing tasks possess the characteristics that make them likely candidates for inspection errors induced by the vigilance effect. A summary of the characteristics associated with tasks that can be expected to be influenced is shown in Table 4.

In the left column, the table indicates traits or characteristics of a task that increase the task's potential for being influenced by the vigilance phenomenon. For example, where visual inspection tasks that are easily learned, involve a binary decision (e.g. pass/fail, present/not present), have a low probability of occurrence, and require "discrete" viewing of successive "scenes" for the target stimulus.

Characteristics	Reference
Low Probability of Occurrence Events	Desse and Ormond; Fortune; Galinsky et al; Jenkins; Kappauf and Powel
Visual Attributes	Adams; Fortune; Warm, Dember, Parasuraman; Wiener
Discrete Events	Fortune; Desse and Ormond; Jenkins
Easily Learned/Training	Jenkins; Kauppauf and Powel; Williams
Performance	Kauppauf; Jenkins
Binary Categories	Cole et al; Craig; Loeb et al; Galinsky et al; Jenkins; Warm, Dember, Parasuraman; Wiener

Table 4:

Characteristics Of Tasks Identified In Literature As Subject To Vigilance Problems

The third category of recommendations deals with a review of Orbiter and Shuttle processing tasks to determine which of the tasks are candidates for vigilance problems and which of the candidate tasks should be examined in more detail.

More specifically, it is recommended that:

1) Orbiter and Shuttle processing tasks should be reviewed to identify those tasks having the potential for vigilance-induced errors. In the first stage of the review, processing tasks would be classified as either having or not having the potential for vigilance-induced errors. Tasks having those characteristics summarized in Table 4 would be categorized as vigilance problem candidates. Other tasks would be excluded from further consideration in the review process.

2) Assign A Vigilance Problem Potential Index. Tasks identified in the first step of the process review procedure as having the potential for a vigilance problems should be individually reviewed and scored with respect to:

- degree of criticality of errors that would result from the vigilance effect
- strength of the task potential for being influenced by the vigilance effect.

The scores obtained would then be combined in a manner similar to that employed in the development of the Improvement Potential Index described in the section of this report detailing the component of the Cooperative Agreement entitled: "Human Factors Analysis of TPS Tile Processing Methods" in order to develop a Vigilance Problem Potential Index. Processing tasks with the highest Vigilance Problem Potential Index would be the processes that would be selected first for action to reduce vigilance-induced problems.

3) Specific Process Review. Tasks Identified in step 2 above as being the most worthy of more in-depth review should then be reviewed by a person or persons capable of assessing the processing task with respect to:

- the task components associated with potential vigilance problems
- data available to more accurately quantify the vigilance potential and analyze the factors contributing to that potential
- appropriate experimentation required for obtaining additional data for quantification of vigilance potential and factors influencing vigilance
- corrective measures related to reducing or eliminating the vigilance problem

Conclusion

This project component has demonstrated that Orbiter processing tasks involving visual

inspection by humans for low probability of occurrence events can be expected to be subject to problems associated with the "Vigilance Effect" or "phenomenon." That is, there exists a high probability that the inspection process will fail to identify the occurrence of the low probability event.

The consequences of the existence of the Vigilance Effect in processing activity would seem to be two-fold in nature: The first type of consequence is related to mission safety and the acceptability of the output of Orbiter and Shuttle processing activities in preparing the vehicle and the Shuttle for a mission. In general, the type of event that can be expected to occur as a result of the vigilance effect is undesirable. Events that should be detected by inspection processes are missed. The consequences of these missed events will vary and are dependent on the nature of the event. Shims that fly in gaps on the vehicle and survive obviously were not in high heat build-up areas. Their presence does, however, result in a tile gap which is there for a purpose being filled and perhaps introducing undesirable "side" loads on a tile bond. Vigilance events occurring in other systems, STR structural system inspections, for example, could have varying degrees of consequences from minor to severe.

Another category of consequences is one that develops over a long period of time as engineers, supervisors and technicians develop work procedures that compensate for and counteract the effect of vigilance problems. The occurrence of errors in visual inspection due to the vigilance effect on human inspectors results in routine duplication of inspection processes through follow-up inspection, multiple person inspection teams, and also results in rework to correct problems discovered on the follow-up inspections. These added work procedures contribute extra cost to and require extra time in the Shuttle processing flows.

References

Adams, J.A. Vigilance in the Detection of Low-Intensity Visual Stimuli. Journal of Experimental Psychology, 1956

Cole, Barry L. and Hughes, Phillip K. *A Field Trial of Attention and Search Conspicuity.* Human Factors, 1984, 26(3), 299-313

Craig, Angus. *Signal Detection Theory and Probability Matching Apply to Vigilance.* Human Factors, 1987, 29(6), 645-652

Craig, Angus, Davis, D.R., and Matthews, G. Diurnal Variation, Task Characteristics and Vigilance Performance. Human Factors, 1987, 29(6), 675-684

Desse, J. and Ormond, E. *Studies of Detectability During Continuous Visual Search.* U.S.A.F. Wright Development Center Technical Report, 1953

Fortune, Bill. *An Experimental Investigation of the Effects of Selected Vigilance Variables On Inspection Accuracy In A Visually Aided Scanning Task.* The University of Arkansas, 1975

Fisk, Arthur D., Scerbo, Mark W. *Automatic and Control Processing Approach to Interpreting Vigilance Performance: A Review and Reevaluation*, Human Factors, 1987, 29(6), 653-660

Galinsky, Tracy I., Warm, Joel S., Dember, William N. and Weiler, Earnest M. *Sensory Alteration and Vigilance Performance: The Role of Pathway Inhibition.* Human Factors, 1990, 32(6), 717-728

Jenkins, Herbert M. *The Effects of Signal Rate on Performance in Visual Monitoring.* American Journal of Psychology, 1958

Kappauf, W.E. and Powe, W.E. *Performance Decrement on an Audio-Visual Checking Task.* Journal of Experimental Psychology, 1959, 57

Loeb, Michael, Noonan, Thomas K., Ash, Dan W. and Holding, Dennis H. *Limitations of the Cognitive Vigilance Increment.* Human Factors, 1987, 29(6), 661-674

Swets, John A. and Green, David M. *Applications of Signal Detection Theory. Psychology: From Research to Practice*, Edited by H.L. Pick Jr. et al.. (Plenum Publishing Corporation, 1978)

Verbaten, Harry S., Brinkman Jan and Verbaten, Marinus N. *Processing Demands, Effort and Individual Differences in Four Different Vigilance Tasks.* Human Factors, 1989, 31(1) 45-62

Warm, Joel S. *Vigilance and Target Detection.* National Academy Press, 1992

Warm, Joel S., Dember, William N. and Hancock, Peter. *Operator Workload Scheduling and Performance*. University of Cincinnati/Dept. of Psychology, NAG-1-1118

Weiner, Earl L. *Vigilance and Task Load: In Search of the Inverted U.* Human Factors, 1984, 26(2), 215-222

Williams, Peter S. Processing Demands, Training and the Vigilance Decrement. Human Factors, 1986, 28(5), 567-579